Characterization of Battery Anode Materials by X-ray and Electron-Based Imaging Techniques

vorgelegt von
M. Eng.
Kang Dong

von der Fakultät III – Prozesswissenschaften
der Technischen Universität Berlin
zur Erlangung des akademischen Grades

Doktor der Ingenieurwissenschaften
- Dr. -Ing. -

genehmigte Dissertation

Promotionsausschuss:
Vorsitzender: Prof. Dr. Walter Reimers
Gutachter: Prof. Dr. John Banhart
Gutachterin: Prof. Dr. Yan Lu
Gutachterin: Prof. Dr. Julia Kowal

Tag der wissenschaftlichen Aussprache: 28 August 2019

Berlin 2020

Erklärung

Ich erkläre hiermit, dass ich die vorliegende Dissertation selbst verfasst und keine anderen als die angegebenen Quellen und Hilfsmittel verwendet habe.

Berlin, 2020 Kang Dong

Abstract

To tackle the problem of increasing carbon dioxide emissions, Li batteries have been proposed as a promising storage medium of electricity harvested from renewable clean energy sources. In addition, Li batteries are the predominant power sources in cell phones, laptops and electric vehicles. However, state-of-art Li-ion batteries with an energy density below 300 Wh kg^{-1} cannot meet the ever-increasing demands for lighter and safer batteries with longer life time and lower costs. Li batteries based on anode materials with higher specific capacity (*e.g.* silicon and lithium) could potentially boost the energy density of Li batteries. In this dissertation, X-ray and electron-based imaging techniques were used to investigate the currently existing challenges that prevent the massive commercial deployment of silicon and lithium anodes.

Firstly, *in-situ* and *operando* synchrotron X-ray radiography was employed to visualize the internal microstructure change of a silicon electrode during cell operation. The volume expansion and shrinkage of individual Si particles during lithiation and delithiation were dynamically displayed. An expansion prolongation phenomenon was discovered and quantified whereby some particles continue expanding even after the reversal of the external battery current direction when shrinkage would be expected. Secondly, lithium deposition at the Li/separator and at the Li/carbon matrix interregion was discovered by synchrotron X-ray tomography. A higher concentration of widely distributed deposition sites was found under an increased deposition density. The morphology and distribution of Li deposition within the commercial Celgard® 2325 separator are, for the first time, presented in three dimensions. In addition, the spatial distribution of Li deposition inside a carbon deposition host was visualized and quantified. Thirdly, the Li deposition mechanism was further investigated using focused ion beam scanning electron microscopy. Li nucleation was found to preferably stem from surface irregularities (cracks and impurities, *etc.*) of the Li substrate. Surface heterogeneity of the Li substrate is concluded as one critical fundamental cause for the initial inhomogeneous nucleation, rather than the SEI properties and/or an uneven Li-ion flux. Computational modeling of the electrode/electrolyte interface further confirms the favorable nucleation sites and helps to explain the nucleation and growth behavior of dendrites. Lastly, a $Li_{10}SnP_2S_{12}$ (LSPS) solid-state electrolyte was employed in a Li-S cell to mitigate the side reactions of liquid electrolyte and suppress the dendritic growth. *In-situ* and *operando* synchrotron tomography and energy dispersive diffraction were simultaneously conducted to visualize the morphological and compositional evolution. Cavities/voids observed at the InLi/LSPS interface demonstrated the interfacial mechanic degradation during battery operation, which was also reflected by the energy dispersive diffraction results and the electrochemical performance.

Kurzfassung

Um das Problem der zunehmenden Kohlendioxidemissionen anzugehen, wurden Lithium-Ionen-Batterien als vielversprechendes Speichermedium für Strom aus erneuerbaren sauberen Energiequellen vorgeschlagen. Darüber hinaus sind Li-Batterien die vorherrschenden Energiequellen in Mobiltelefonen, Laptops und Elektrofahrzeugen. Selbst hochmoderne Li-Ionen-Batterien mit einer Energiedichte von weniger als 300 Wh kg^{-1} können die ständig steigenden Anforderungen nach leichteren und sichereren Batterien mit längerer Lebensdauer und geringeren Kosten nicht erfüllen. Li-Batterien auf Basis von Anodenmaterialien mit höherer spezifischer Kapazität (mit z. B. Silizium und Lithium) könnten möglicherweise die Energiedichte von Li-Batterien drastisch erhöhen. In dieser Dissertation wurden Röntgen- und elektronenbasierte Bildgebungstechniken verwendet, um die aktuellen Herausforderungen zu untersuchen, die den massiven kommerziellen Einsatz von Silizium- und Lithiumanoden derzeit noch verhindern.

Als Erstes wurde mit In-Situ- und Operando-Synchrotron-Röntgenradiographie die interne Mikrostrukturänderung einer Siliziumelektrode während des Zellbetriebs sichtbar gemacht. Die Volumenexpansion und -schrumpfung einzelner Si-Partikel während der Lithiierung und Delithiierung wurde dynamisch dargestellt. Es wurde eine Expansionsverzögerung entdeckt und quantifiziert, bei dem sich einige Partikel auch nach der Umkehr der externen Batteriestromrichtung weiter ausdehnen, wenn eigentlich schon eine Schrumpfung zu erwarten wäre. Zweitens wurde eine Lithiumabscheidung am Li-Separator- und im Li-Kohlenstoff-Matrix-Zwischenbereich durch Synchrotron-Röntgentomographie entdeckt. Bei einer erhöhten Ablagerungsdichte wurde eine höhere Konzentration weit verteilter Ablagerungsstellen gefunden. Die Morphologie und Verteilung der Li-Abscheidung im kommerziellen Celgard® 2325-Separator wird erstmals dreidimensional dargestellt. Zusätzlich wurde die räumliche Verteilung der Li-Abscheidung im Kohlenstoff sichtbar gemacht und quantifiziert. Drittens wurde der Li-Abscheidungsmechanismus unter Verwendung eines fokussierten Ionenstrahls in Kombination mit einem Rasterelektronenmikroskop weiter untersucht. Es wurde festgestellt, dass die Li-Keimbildung vorzugsweise von Oberflächenunregelmäßigkeiten (Rissen und Verunreinigungen usw.) des Li-Substrats herrührt. Die Oberflächenheterogenität des Li-Substrats wird als eine kritische fundamentale Ursache für die anfängliche inhomogene Keimbildung angesehen und nicht die Elektrode/Elektrolyt Grenzschicht-Eigenschaften und/oder ein ungleichmäßiger Li-Ionen-Fluss. Die rechnergestützte Modellierung der Grenzfläche zwischen Elektrode und Elektrolyt bestätigt die begünstigten Keimbildungsstellen und hilft, das Keimbildungs- und Wachstumsverhalten von Dendriten zu erklären. Schließlich wurde in einer Li-S-Zelle ein $Li_{10}SnP_2S_{12}$-Festkörperelektrolyt (LSPS) eingesetzt, um die Nebenreaktionen des flüssigen Elektrolyten zu umgehen und das dendritische Wachstum zu unterdrücken. In-situ- und Operando-Synchrotron-

Tomographie und energiedispersive Röntgenbeugung wurden gleichzeitig durchgeführt, um die morphologische und kompositorische Entwicklung zu visualisieren. An der InLi/LSPS-Grenzfläche beobachtete Hohlräume zeigten die mechanische Verschlechterung der Grenzfläche während des Batteriebetriebs, was sich auch in den Ergebnissen der energiedispersiven Röntgenbeugung und der elektrochemischen Leistung widerspiegelte.

Contents

1. Introduction

Since the First Industrial Revolution, energy-driven consumption of fossil fuels has led to a dramatic increase in carbon dioxide (CO_2) emission (Figure 1). The production of electricity/heat and transportation, which are two main sectors related to burning fossil fuels (coal, oil and natural gas), accounts for around 50 % and 20 % of all the contributors to the global CO_2 emissions in 2014, respectively. The increasing concentration of CO_2 is able to enhance the greenhouse effect, which would lead to global warming and therefore would endanger the survival of human beings.

Utilizing clean and sustainable energy sources is an essential solution to reduce CO_2 emission. Renewable energy sources, for instance, solar and wind power, are intermittent and thus require powerful energy storage systems. Electrical energy storage systems like batteries can be used not only as an electricity storage medium for household use and smart electric grid during off-peak hours but also as the power sources for transportation like electric vehicles (EV).[1]

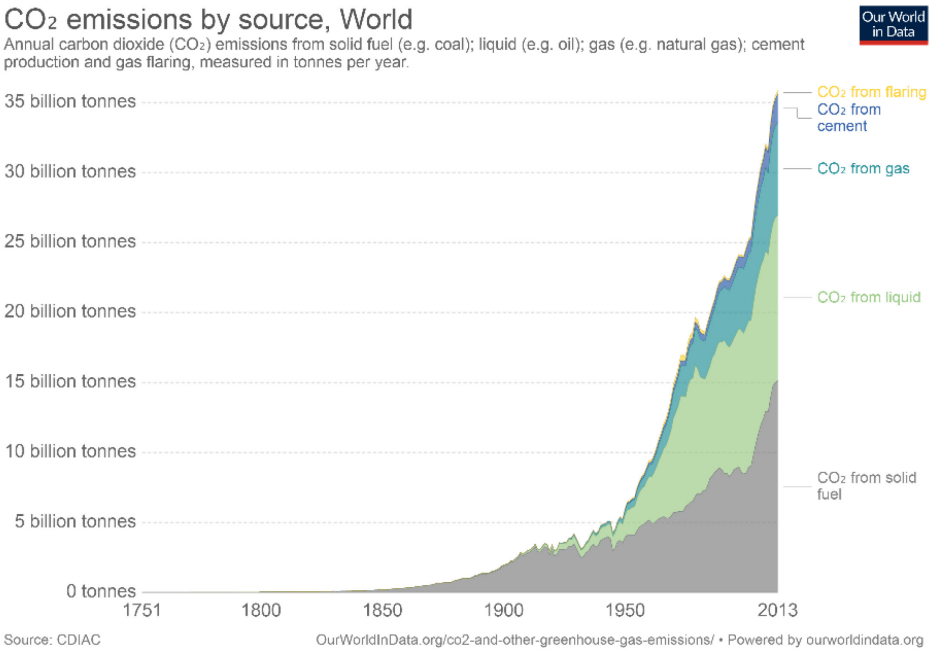

Figure 1. Carbon dioxide emissions from different fuel sources from 1751 to 2013. [2]

However, the state of the art Li-ion batteries have the energy density of around 250 Wh/kg [3, 4] by 2017, which cannot meet the ever-increasing market demand for higher energy density, lighter and safer batteries with longer lifetime and lower costs. For example, to match or even surpass the vehicle range with internal combustion engine as well as address “range anxiety”, advanced lithium batteries with superior performance and lower cost are highly desired to approach the performance needed to power an electric car for over 500 km on a single charge.

1.1 Basic principle

A battery is a device that converts the chemical energy contained in its active materials directly into electric energy by means of an electrochemical redox reaction.[5] It normally consists of one or more basic electrochemical cells connected in series or parallel. A single-cell battery is typically composed of a cathode, an anode, a separator, electrolyte and a container.

Depending on their capability of being electrically recharged, batteries are classified as primary and secondary (rechargeable). Due to good reversibility of the redox reaction between the active materials inside, rechargeable batteries are able to be repeatedly discharged and charged electrically without distinct capacity decay in short term.

Lithium (Li) batteries were first proposed by British chemist M. Stanley Whittingham in the 1970s. He used titanium (IV) sulfide and lithium metal as the electrodes. In this battery, Li ions migrate from the anode to the cathode during discharge and back when charging. The motivation to use Li metal as the anode is largely due to its lightweight (0.534 g cm^{-3}) and the most electronegative potential (-3.04 V *vs.* the standard hydrogen electrode (SHE)). During the following decades, different materials were used to replace the cathode and anode in order to increase the capacity, energy density, cycling life and safety.

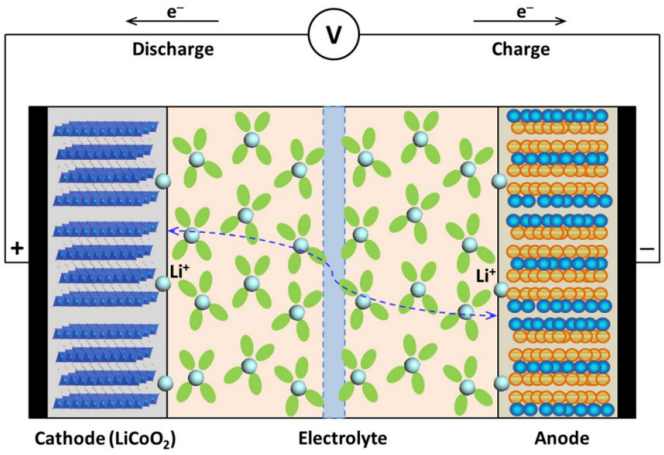

Figure 2. A schematic of the working principle of a typical Li-ion battery.[6]

Based on the type of anode materials, Li batteries can be categorized into Li-ion batteries and Li metal batteries (LMB). Typical Li-ion batteries are rechargeable and consist of a graphite anode and a transition metal oxide cathode, as shown in Figure 2. While available Li metal batteries at present, which use lithium metal as an anode, are basically primary batteries, largely due to the inferior cycling ability and safety concerns related to the lithium anode during battery cycling.

1.2 Lithium battery materials

A road map for the development of anode and cathode materials for Li batteries with the potential *vs.* Li/Li^+ of each material as a function of its theoretical capacity is shown in Figure 3. Theoretically, one can pair one material at the anode region (typical potential *vs.* Li/Li^+ >1.6 V) with one at the cathode region (typical potential *vs.* Li/Li^+ < 1.6 V) to build a battery given a suitable electrolyte is well chosen.

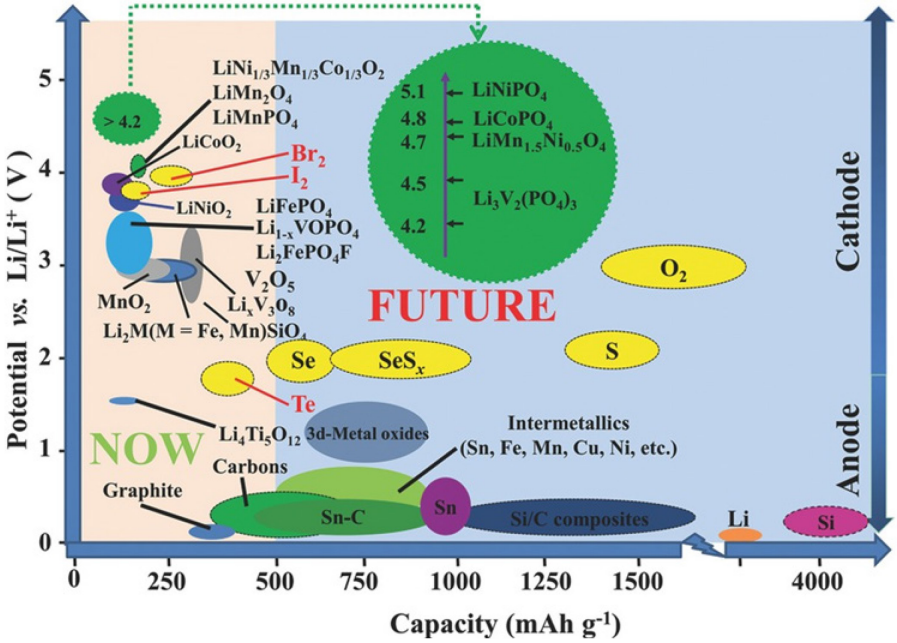

Figure 3. A road map for the development of electrode materials for Li batteries.[7]

An ideal electrode material for Li battery should meet the requirements of 1) high energy density and high reversible capacity; 2) bigger potential difference against the other electrode; 3) high rate or power capability; 4) low cost, environmentally friendly and excellent abuse tolerance; 5) wide working temperature range. [6]

Except for electrode materials, electrolytes and separators also play a virtual role in a working battery, which will be briefly described in this chapter.

In general, the gravimetric capacity of a cell can be expressed as follows [8]:

$$Q\ (mAh\ g^{-1}) = \frac{1}{\frac{1}{Q_a}+\frac{1}{Q_c}+\frac{1}{Q_m}} \qquad (1)$$

where Q_a and Q_c are the theoretical gravimetric capacity of anode and cathode materials, respectively, and Q_m is the gravimetric capacity of other cell components (*e.g.* electrolyte, separator, current collector and cell case). To boost the gravimetric capacity and energy density of a cell, adopting anode and cathode materials with higher theoretical capacity and a bigger potential difference between them would be a promising approach.

1.2.1 Anode material

Based on the electrochemical reaction mechanism, the anode materials in Figure 3 can be basically classified into three main groups: 1) intercalation anodes, *e.g.* carbon-based materials and $Li_4Ti_5O_{12}$; 2) alloy anodes like Si, Ge and Sn; 3) conversion anodes, mainly referring to transition metal oxides but also including metal sulfides, phosphides and nitrides.[6]

Among all the anode materials, graphite is the first commercial one for Li-ion batteries due to its good reversibility and long cycle life. The maximum theoretical capacity of graphite is 372 mAh g^{-1}, which falls far below the specific capacity of silicon and lithium and thereby limits the energy density of Li batteries.

1.2.1.1 Silicon anode

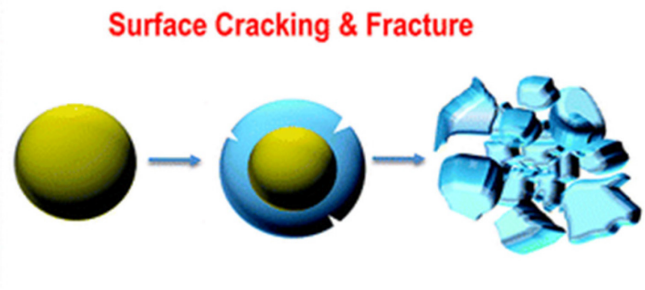

Figure 4. A schematic of the cracking and volume change of silicon particles during lithiation. Reprinted with permission from reference [9]. Copyright (2012) American Chemical Society.

Silicon (Si) could yield the highest specific capacity (4200 $mAhg^{-1}$) upon full lithiation ($Li_{22}Si_5$) among all known anode materials, which is approximately 10 times that of the conventional graphite anode with a fully lithiated phase of LiC_6.[10-12]

However, the large amount of Li ions inserted into Si materials leads to an extreme volume expansion as shown in Figure 4, which is approximately 400% calculated on the basis of the volume change of the crystal structure.[8] Volume expansion during lithiation and the unavoidable shrinkage during delithiation bring about repetitive structural changes accompanied by mechanical deformation. The capacity of the Si electrode decreases irreversibly during the volume change due to the generation of electrical isolation of fractured Si fragments.

During the repetitive volume change, the concomitant generation and fracture of a solid-electrolyte interface (SEI) layer on the Si surface, which is the decomposition product of the organic electrolyte, will consume electrolyte and re-expose fresh Si to the electrolyte. This process will directly lead to a low coulombic efficiency and gas generation. Large volume change is therefore widely regarded as the root cause of the short lifetime of silicon-based anodes.

1.2.1.2 Lithium anode

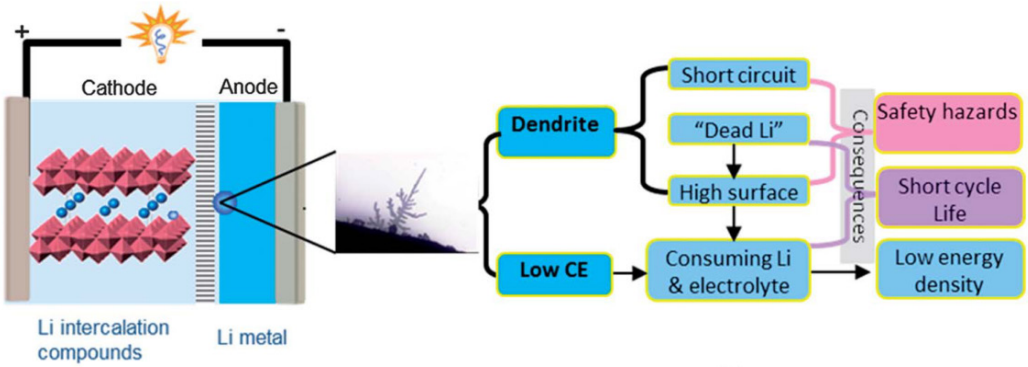

Figure 5. A schematic of Li metal batteries and the primary problems related to the Li metal anode. [13]

The attempt aiming to employ lithium metal as anode material for Li metal batteries (LMBs) could be traced back to 1970s when lithium batteries were firstly proposed. Since then tremendous efforts have been devoted to boosting the practical use of Li anode over the last four decades. [4, 14-16]

Lithium metal batteries (LMSs) typically consist of metallic lithium anodes, sulfur or oxygen or Li intercalation compounds as cathodes, and organic liquid, polymer or hybrid-gel electrolytes. Li metal has several highly appealing advantages as a anode material; 1) Li metal is lightweight with a low density of 0.534 g cm^{-3}; 2) Li metal has the lowest anode potential (-3.04 V *vs.* SHE) of all known electrode material; 3) A high theoretical capacity of 3 860 mAh g^{-1} or 2 061 mAh cm^{-3} versus the storage capability of the carbon anode (340 Ah kg^{-1} or 740 mAh cm^{-3}); 4) Theoretically, no need for copper current collectors (9 g cm^{-3}) that is used in conventional Li-ion batteries, which can increase the energy density of the batteries dramatically. [17]

However, after over 40 years of research and development, the practical applications of LMBs are still hindered by the uncontrollable growth of hazardous Li microstructures (*e.g.* dendrites and fibres) and a low coulombic efficiency derived from unstable solid electrolyte interphase (SEI), [13, 18] as shown in Figure 5. The concomitant problems and challenges are safety issues, short service life and low energy density.

Regarding hazardous Li microstructures, it is commonly regarded that inhomogeneous/dendritic deposition originates from 1) an inhomogeneous SEI which will induce "hot spots" for preferred deposition; 2) weak electrochemical stability and mechanical strength of the SEI layer leading to the exposure of fresh Li that is favorable for Li deposition [19]; 3) inhomogeneity of the Li^+ concentration on the anode surfaces. The operation of a Li-ion or Li metal battery requires the transport of Li ions inside the battery between cathode and anode in a closed electric circuit, corresponding to the charge-transfer reaction $Li^0 \Leftrightarrow Li^+ + e^-$ at Li metal anode. Non-uniform local current densities across the lithium surface during charge or discharge lead to preferred Li ion deposition and dissolution at a relatively small number of sites, creating dendritic and

fibre-like deposition during charging and "dead" lithium during discharging that is nonactive in subsequent cycles.

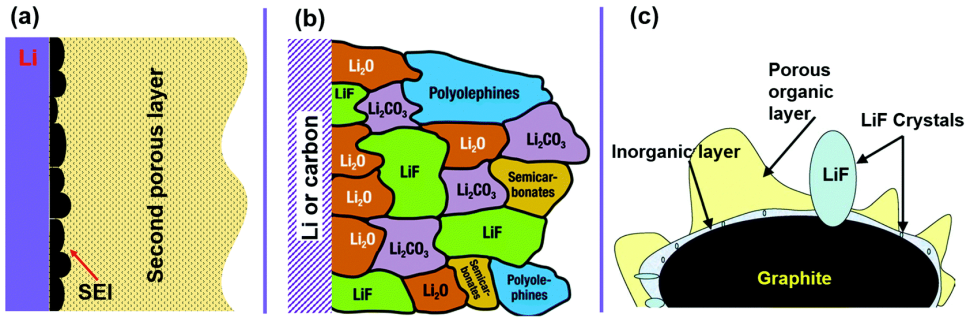

Figure 6. Three structural and/or composition models of the solid electrolyte interfaces (SEI) on lithium or carbon anodes.[20, 21] (a) The double-layer structure model proposed in 1983; (b) A Mosaic model revealing the structure and composition of SEI on Li or carbon proposed in 1997; (c) A Mosaic model on graphite anode proposed in 2006. Reproduced from reference [20].

A low coulombic efficiency is the combined result of parasitic reactions of Li metal with liquid electrolytes and the instability of solid electrolyte interfaces (SEI). Li is thermodynamically unstable in non-aqueous electrolytes [15], and will react with the organic solvents and salts at the Li/electrolyte interface and generate a passivation layer termed solid electrolyte interface (SEI) layer. The SEI was firstly proposed by E. Peled, and exists in all alkali metals and alkaline earth battery systems based on non-aqueous electrolytes.[21, 22] Typically, the SEI layer is composed of mixed Li-based compounds such as Li alkyl carbonates ($ROCO_2Li$, ROLi, *etc.*) and Li salts (*e.g.* LiOH, Li_xPF_y), as shown in Figure 6. This SEI layer covering on the surface of Li anodes is not stable, primarily due to the dramatic volume change at Li surfaces during repetitive Li deposition and dissolution.

1.2.2 Cathode material

1.2.2.1 Transition metal oxide cathodes

Typical cathode materials for Li-ion batteries are transition metal oxide cathodes, like layered $LiMO_2$ (M=Co, Ni, Mn, and their mixture), spinel LiM_2O_4 (M=Mn, and mixture with Co or Ni), and olivine $LiMPO_4$ (M=Fe, Mn, Ni, Co, and their mixture).[23, 24]

Lithium cobalt oxide ($LiCoO_2$) was the first commercial cathode which was developed by John B. Goodenough in 1980 and was later employed in Sony's Li-ion battery in 1991. Afterward, it acted as the dominant cathode materials of Li-ion batteries for portable electronics for years. It can deliver a specific capacity of 140 mAh/g in practical use and has good cyclability and moderately high rate capability. But Li_xCoO_2 is not chemically stable at $x < 0.5$, resulting in oxygen evolution and concomitant safety issues as well as structure degradation.[23] In addition, due to its high cost and toxicity, a number of cathode materials have been investigated, including $LiMn_2O_4$, $LiFePO_4$,

and derivatives of $LiCoO_2$ ($LiNi_{0.8}Mn_{0.15}Al_{0.05}O_2$ and $LiNi_xMn_yCo_{1-x-y}O_2$). These derivatives of $LiCoO_2$ are generated by partially substituting Co cations with more abundant Ni and/or Mn, as the substitution could generally improve the structural stability at the expense of small operating voltage and cycling capacity.[23] Table 1 shows the comparison of these transition metal oxide cathodes.

Table 1. Comparison of various cathode materials used in commercial Li-ion batteries. [25]

Cathode Material	Midpoint voltage vs. Li (C/20)	Specific Capacity (Ah/kg)	Advantages	Disadvantages	Applications
LCO	3.9	155	In common use, good cycle life, good energy	Moderate charged state thermal stability,	Mainly smaller portable electronics (3C)
LMO	4.0	100–120	Very good thermal stability, inexpensive, very good power capability	Moderate cycle life, lower energy	Higher power applications such as power tools and electric motive power
NCA	3.7	180	Very good energy, good power capability, good cycle life	Moderate charged state thermal stability, sensitive to moisture even in discharged state	Excellent for motive power and premium electronic applications
NMC	3.8	160	Very good combination of properties (energy, power, cycle life and thermal stability)	Patent issues	Both portable and high power applications including power tools and electric vehicles
LFP	3.4	160	Very good thermal stability and cycle life, good power capability	Lower energy, special preparation conditions	Mainly used in high power such as power tools and energy storage applications, patent issues

Note: LCO is $LiCoO_2$; LMO is $LiMn_2O_4$; NCA is $LiNi_{0.8}Mn_{0.15}Al_{0.05}O_2$; NMC is $LiNi_xMn_yCo_{1-x-y}O_2$; LFP is $LiFePO_4$.

1.2.2.2 Sulfur cathode

Sulfur (S) has the highest theoretical capacity of 1675 mAh g^{-1} among the solid cathode materials, as shown in Figure 3, which is over 5 folds larger than that of the transition metal oxides cathodes. In addition, sulfur has the advantages of high energy density, low-cost and environmental friendliness.[26-28] When paired with metallic Li, Li-S cells, with a theoretical energy density of 2600 Wh kg^{-1}, could deliver a practical energy density of 400-600 Wh kg^{-1}, which is around two times higher than that of current Li-ion batteries.[29]

The reaction process of sulfur in Li-S batteries with liquid electrolyte undergoes three phase-transition stages[30]:

The first solid-to-liquid stage with a theoretical capacity of 208 mAh g^{-1}:

$$S_8 + 2Li^+ + 2e^- \rightarrow Li_2S_8 \qquad (2)$$

The second liquid-to-liquid stage with a theoretical capacity of 208 mAh g^{-1}:

$$Li_2S_8 + 2Li^+ + 2e^- \rightarrow 2Li_2S_4 \qquad (3)$$

The third liquid-to-solid stage with a theoretical capacity of 1256 mAh g^{-1}:

$$Li_2S_4 + 6Li^+ + 6\,e^- \rightarrow 4Li_2S \qquad (4)$$

Due to the high solubility of the intermediate polysulfides (*i.e.*, Li_2S_x, x = 8, 6, 4, and 3) in organic liquid electrolyte, long-chain polysulfides (PS) which refers the

polysulfides generated during the charging process, can travel to the lithium anode and be reduced to short-chain polysulfides which can then diffuse back and be re-oxidized to long-chain polysulfides. This migration phenomenon is called “shuttle effect” and can result in low coulombic efficiency and rapid capacity fading.

The full discharged product of sulfur namely lithium sulfide (Li_2S) can also be employed as a cathode material and can be regarded as a derivative of the sulfur cathode. In this case, the Li-Li_2S batteries must be firstly charged and then is almost equivalent to the Li-S battery system.

1.2.3 Separator

A separator is a permeable membrane that separates a battery’s anode and cathode from electronic contact while it enables ionic transport between the two electrodes. Therefore it should be a superior electronic insulator and be able to allow rapid ionic migration. Typically, a separator is a solid matrix that possesses a microporous structure and is wetted by liquid electrolyte in practical use.

There are several important factors needed to be considered when choosing a separator, including composition, thickness, porosity, ionic resistivity, (electro-)chemical/thermal/mechanical stability.[31]

1.2.3.1 Composition

Separators used in batteries that work at ambient temperatures are mostly made of nonwoven fabrics (*e.g.* nylon, cotton, polyesters) or polymer films (*e.g.* polyethylene (PE), polypropylene (PP), poly(tetrafluoroethylene) and poly(vinyl chloride)).[31]

In Li-ion batteries sector, polyolefins materials are adopted due to their excellent combination of mechanical properties, chemical stability and acceptable cost. Most of the commercial polyolefin separators compose of one single or multilayer of polyolefins like PE or PP sheet.

Table 2. Typical properties of several commercial separators.[32]

	Entek	Exxon	Degussa	Celgard
Product	Teklon	Tonen	Separion	2325
Thickness (μm)	25	25	25	25
Single/multilayer	Single layer	Single layer	Trilayer	Trilayer
Composition	PE	PE	Ceramic-PET-Ceramic	PP-PE-PP
Process	Wet extruded	Wet extruded	Wet-laid mat	Dry extruded
Porosity (%)	38	36	>40	41
Melt temperature	135	135	220	134/166

*Separator specifications are found on data sheets for each product

1.2.3.1 Pore size

Separators with big pores have lower ionic resistivity but could not effectively prevent the penetration of possible dendritic lithium thus lead to safety issues. The typical porosity is around 40 % with thickness near 25 μm, as Table 2 shows.

1.2.3.1 Thickness

Celgard® 2400 and 2500 are both single PP layer separators while Celgard® 2500 has bigger pore size and therefore enables better high rate performance. Celgard® 2325 is a triple-layer separator (PP/PE/PP) with each layer has nearly the same thickness. For Li batteries used in EV, thicker separators (~40 μm) which have greater mechanical strength are required to increase safety.

1.2.3.3 Stability

The stability of separator includes chemical, electrochemical, thermal and mechanical stability. Firstly, a separator must be chemically stable with electrolyte and electrode materials after soaking liquid electrolyte and cell assembly for a long period. During battery charge and discharge, separators must be inert and not involved in the redox reactions, which means a superior electrochemical stability.

In addition, separators should also be thermal stable during the drying procedure in the Li-ion battery industry which is normally conducted around 80 ºC under vacuum. The most widely used polyolefin PE and PP have the melt temperature of around 135 ºC and 165 ºC, respectively. A shrinkage of less than 5% after 60 min drying at 90 ºC under vacuum is regarded as a reasonable generalization.[33]

An excellent mechanical and dimensional stability are also required during battery practical use. A good mechanical performance of separator will avoid rapid short-circuit of cells and thus enhance the safety. No obvious curl should occur at the edges if they are unrolled. Also, when used in pouch cells winding of separators should not affect the porous structure at the winding part.

1.2.3.3 Ionic resistivity

When using a separator the effective ionic conductivity of electrolyte will be decreased by a factor of 6-7 compared with free electrolyte because of mass transfer resistance inside the pores. Suitable microstructure, which is related to the pore size, porosity and channel structure, could facilitate ionic migration and enhance high rate performance. The ionic resistivity of the separator can be evaluated by the ratio of the resistivity of the separator soaked in the electrolyte and the resistivity of the free electrolyte, which is called MacMullin number.

1.2.4 Electrolyte

Serving as the charge transfer medium within a cell between a pair of electrodes, electrolytes are an indispensable component. The interfaces between electrolyte and the electrodes determine the overall performance of a cell. Therefore, the chemical and electrochemically stability of electrolytes is of high importance in the device. In addition, there are some other requirements that a superior electrolyte should meet, which include 1) good ionic conductivity and electronic insulativity; 2) wide electrochemically stable window; 3) good chemical compatibility with other cell components like separators, electrode substrates and cell packing materials; 4) wide operation temperature range and environmentally friendly.[34]

1.2.4.1 Liquid electrolytes

In general, electrolytes for Li batteries are liquid solutions which are synthesized by dissolving one Li salt into a mixture of two or more non-aqueous solvents.

By mixing solvents with different physical and chemical natures, the obtained solution could achieve a high fluidity and high dielectric constant simultaneously. The solvents that are commonly used in Li batteries are ethylene carbonate (EC), dimethyl carbonate (DMC), diethyl carbonate (DEC), and ethyl methyl carbonate (EMC). Except for viscosity and dielectric constant, the melting and boiling temperature are also important parameters when choosing an electrolyte solvent.

The available Li salts for Li batteries are relatively limited compared to the variety of organic solvents. The salts should have a high solubility and high mobility in solvents. In addition, both the anion and cation are supposed to remain inert to other cell components. Several Li salts that have been investigated for practical use are, for instance, $LiPF_6$, $LiClO_4$, $LiBF_4$, $LiAsF_6$, and lithium bis(trifluoromethanesulfonyl)imide (LiTFSI). Among them, $LiPF_6$ was successfully commercialized due to the combination of a series of well-balanced properties with concomitant compromises and restrictions.[34]

Conceptually, electrolytes should not undergo any chemical and electrochemical reactions with other components during shelf time and battery operation. However, in practical use, the side reactions of electrolyte seem unavoidable. A relatively stable electrode/electrolyte interface is usually achieved by a kinetic (passivation) instead of a thermodynamic manner.[34]

The possible side reactions or decomposition [15, 35] of a commercial Li electrolyte (1 M $LiPF_6$ in EC/EMC (v/v=1:1)) are presented. This electrolyte was also the most used electrolyte in the work of this dissertation.

The dissociation of $LiPF_6$ has two types, as shown by Equation (5) and (6).

$$LiPF_6 \leftrightarrow LiF + PF_5 \quad (5)$$

$$LiPF_6 \leftrightarrow Li^+ + PF_6^- \quad (6)$$

The generated Lewis acid PF_5 can react with trace H_2O and produce HF.

$$PF_5 + H_2O \rightarrow POF_3 + 2HF \quad (7)$$

$$PF_5 + H_2O \rightarrow PF_4OH + HF \quad (8)$$

Reduction of EC is normally preferable compared to other carbonate solvents due to a high polarity and dielectric constant. C_2H_4 gas will be produced during its decomposition.

$$(CH_2O)_2CO + 2e^- + 2Li^+ \rightarrow Li_2CO_3 \downarrow + C_2H_4(g)\uparrow \quad (9)$$

$$(CH_2O)_2CO + 2e^- + 2Li^+ \rightarrow (CH_2OCO_2Li)_2\downarrow + C_2H_4(g)\uparrow \quad (10)$$

The product $(CH_2OCO_2Li)_2$ can further react with trace amount of water in electrolyte.

$$(CH_2OCO_2Li)_2 + H_2O \rightarrow Li_2CO_3 + (CH_2OH)_2 + CO_2\ (g)\uparrow \quad (11)$$

The reduction of EMC follows one-electron reduction process in Equation (12).

$$CH_3CH_2O(C{=}O)OCH_3 + e^- \rightarrow CH_3CH_2O(C\bullet - O^-)OCH_3 \quad (12)$$

The intermediary $CH_3CH_2O(C^\bullet - O^-)OCH_3$ will then react with Li^+ and generate CH_3CH_2OLi.

$$CH_3CH_2O(C^\bullet{-}O^-)OCH_3 + e^- + 2Li^+ \rightarrow LiO(C{=}O)CH_3 + CH_3CH_2OLi \quad (13)$$

1.2.4.2 Solid-state electrolytes

Due to the side reactions, flammability and easy-leak feature of non-aqueous electrolytes, solid-state electrolytes (SSEs) have been recently regarded as a promising candidate to promote cell safety and energy density.[36] Moreover, the remaining issues of dendrite growth and the low coulombic efficiency of Li metal batteries could be potentially solved by replacing liquid electrolytes with SSEs and thus promote the development and commercialization of LMBs.

However, SSEs have suffered from several disadvantages: 1) low ionic conductivity (10^{-8} to 10^{-3} S cm^{-1} *vs.* 10^{-4} to 10^{-2} S cm^{-1} for routine non-aqueous electrolytes); 2) inferior interfacial contact with electrodes; 3) unstable interfaces with electrodes; 4) poor maneuverability due to their fragile nature.[36]

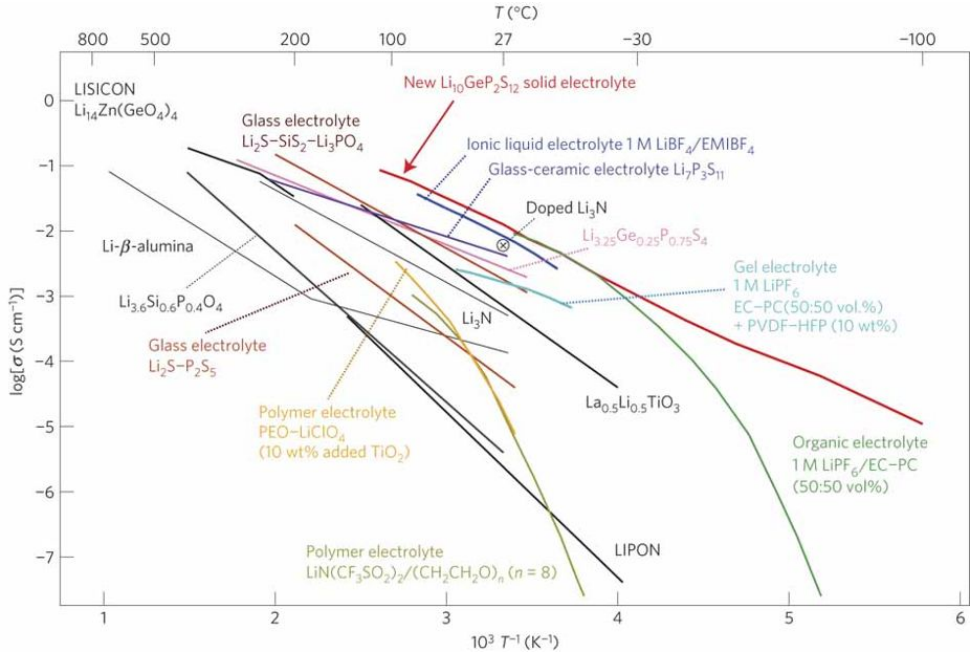

Figure 7. The ionic conductivity of SSEs, organic liquid electrolytes, polymer electrolytes, ionic liquids and gel electrolytes.[37]

The available SSEs can be classified into several groups: 1) the sulfides, or more specifically the thio-LISICON SSEs; 2) the oxides, like $Li_7La_3Zr_2O_{12}$ (LLZO); 3) the polymers, *e.g.* polyethylene oxide (PEO).

The thio-LISICON SSEs are derived from LISICON (Lithium Super Ionic CONductor) compounds by replacing the oxygen with sulfur.[38] The sulfides SSEs [37, 39-42] include $Li_{10}GeP_2S_{12}$ (LGPS), Li_2S-P_2S_5 (LPS) and $Li_{3.25}Ge_{0.25}P_{0.75}S_4$. It can be seen from Figure 7 that the sulfides SSEs generally have a relatively high ionic conductivity, which is even compatible with liquid electrolytes. But they are generally unstable when exposed to air during the manufacturing process and the stability of the electrode/electrolyte interface still needs to be improved.[38, 43]

1.3 Experimental methods

1.3.1 X-ray imaging based on attenuation

Based on the interactions between X-rays and matters, several X-ray imaging techniques have been developed, *e.g.* X-ray fluorescence (XRF), X-ray radiography/tomography and X-ray luminescence tomography. X-ray radiography/tomography is based on the detection of the attenuation or the phase shift of the beam transmitted through a sample. X-ray radiography refers to images recorded without sample rotation while X-ray tomography means images are collected during many different angular positions of a sample that are then reconstructed to a 3D image.

X-rays can be absorbed or scattered by a sample and therefore can be attenuated by intensity. This will induce intensity differences among transmitted X-rays and enable images with contrast generated on a detector. The intensity change of monochromatic X-rays when propagating through a sample obeys the Lambert-Beer law.[44, 45]

$$I = I_0 e^{-\mu d} \tag{14}$$

where I_0 is the flux of incident beam, I is the transmitted photon flux, d is the path distance, and μ is the linear attenuation coefficient of the sample. The coefficient depends on the elemental composition and the density of the composition.[44]

As a non-invasive and non-destructive diagnostic tool, X-ray radiography/tomography has emerged as a unique technique to visualize and quantify the morphological and structural change of materials. With the development of synchrotron radiation sources, X-rays with higher flux become available and thus enable 3D dataset being collected with higher temporal resolution. *In-situ* and/or *operando* measurement can be conducted to track the dynamic change of materials' morphology, chemical composition and crystal structure. For instance, *in situ* synchrotron X-ray tomography was employed to visualize and quantify the electrochemical and mechanical degradation of tin(II) oxide anode material.[46] The evolution of time-resolved, 3D chemical composition and morphology of tin oxide particles during battery operation were presented. Using *in situ* X-ray transmission microscopy (TXM), S. Chao *et al* revealed the interior microstructures of Sn particles during electrochemical lithiation/de-lithiation, from which core-shell reactions of Sn were found to be associated with the formation of cracks.[47] In addition, synchrotron X-ray tomography has also been conducted to uncover the dendritic structure underneath the polymer/electrode interface[48] and the mechanism of internal short circuit induced by Li plating and stripping[49]. All these characteristics have demonstrated that synchrotron X-ray radiography/tomography is highly suitable for battery material studies.[46, 50, 51]

1.3.2 X-ray imaging setups

Two synchrotron X-ray beamlines were employed for the work presented in this dissertation, which are the BAMline and EDDI beamline at the BESSY II electron storage ring of the Helmholtz-Zentrum Berlin. A brief introduction of these two beamlines is presented in this section.

1.3.2.1 BAMline

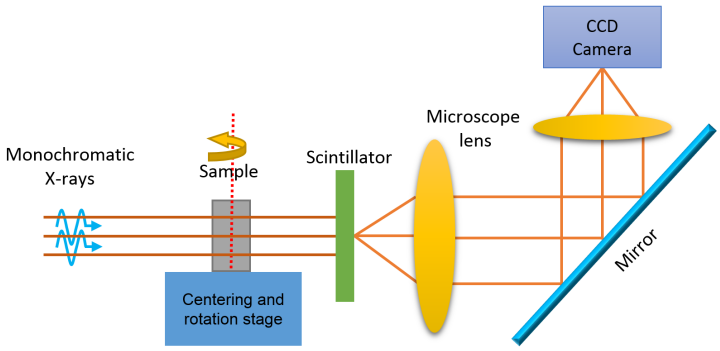

Figure 8. A schematic of the BAMline station at BESSY II.

A schematic of the BAMline station [52] is shown in Figure 8. Generally, the X-rays generated from the electron storage ring are adjusted to a monochromatic beam by the double-multilayer-monochromator (DMM) and/or a double-crystal-monochromator (DCM) with a select energy in the range of 10-35 keV. The aligned incident beam will be attenuated when illuminating the sample, with a portion of the incident beam transmitting through the specimen. The transmitted beam is converted to optical light when passing the scintillator. The optical light will be magnified by a set of traditional optical lens and generate radiography images on the charge-coupled device (CCD) screen. In addition, flat field projections and dark field projections will also be collected for data analysis.

During radiography measurement, 2D projections are recorded by CCD without rotating the cell. An example of this technique is shown Section 2.1 related to lithiation and delithiation of silicon particles.

To get three dimensional (3D) information, normally over a thousand of 2D projections are recorded during a 180° rotation of a specimen. These 2D projections are normalized (using the dark field and flat field projections) and reconstructed by an algorithm written in IDL 8.2 to get a stack of 3D tomographic slices.

1.3.2.2 EDDI beamline

The EDDI beamline at the BESSY II electron storage ring is operated in the **E**nergy **D**ispersive **Di**ffraction (EDDI) mode with a hard synchrotron white beam with an energy range between 8-150 keV. This beamline is suitable for time-resolved *in-situ*

and *operando* imaging (radiography/tomography) and diffraction analysis simultaneously [53, 54] and can therefore be employed for the analysis of structural changes and phase transformations of materials. The doctoral work related to all-solid-state Li-S batteries was conducted at EDDI beamline to visualize the structural change of the solid-state electrolyte as well as reveal the phase transformation of the sulfur electrode.

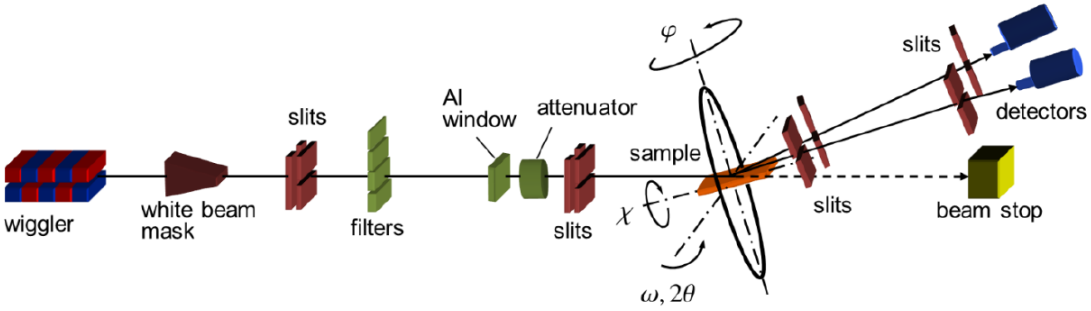

Figure 9. The optical layout of beamline EDDI at BESSY II. Reproduced from reference [53].

Similar to the BAMline, the EDDI beamline is able to implement X-ray imaging based on X-ray attenuation but with a lower spatial resolving power (~ 3 μm). As a white beam is used at EDDI, no monochromator is installed. As shown in Figure 9, it contains a diffractometer system to record the diffracted beam at a fixed angle (2θ) aligned in the vertical plane of the incident beam axis. Detailed beamline information can be found in references [53-55].

1.3.3 Two customized imaging cells

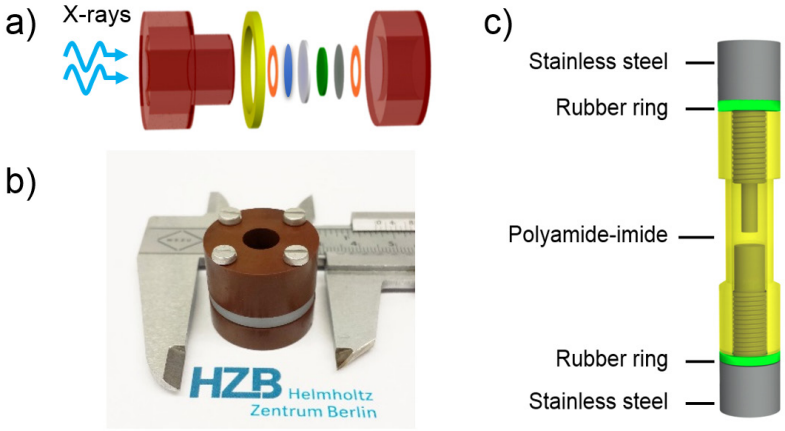

Figure 10. (a) A schematic and (b) a photograph of a cell customized for *operando* synchrotron X-ray radiography; (c) a schematic of the synchrotron X-ray tomography cell. In panel (a) from left to right are housing (claret red), sealing ring (yellow), copper ring (orange), anode (blue), separator (light grey), cathode (green), titanium foil (dark gray, current collector), copper ring (orange), lower housing (claret red). Reproduced from reference [18, 51].

To successfully conduct the experiments at the imaging beamline (BAMline and EDDI), commonly used batteries like coin cells are not suitable as the stainless steel housing

will largely attenuate the X-rays at the photon energy below 35 keV. Therefore two different cells were designed and fabricated (Figure 10) for X-ray radiography and tomography measurements.

The cell housing material (polyamide-imide) is highly transparent to X-rays within the experiment energy range of 10-35 keV, thus enables a high signal-to-noise ratio. In addition, the geometry and dimension should also be considered in order to fit and make full use of the field of view of the cameras.

References

[1] M. M. Thackeray, C. Wolverton, E. D. Isaacs, Electrical energy storage for transportation—approaching the limits of, and going beyond, lithium-ion batteries. *Energy Environ Sci*, **2012**, 5, 7854.
[2] https://ourworldindata.org/co2-and-other-greenhouse-gas-emissions#annual-co2-emissions, accessed July 14, 2019.
[3] R. Van Noorden, The rechargeable revolution: A better battery. *Nature*, **2014**, 507, 26.
[4] D. Lin, Y. Liu, Y. Cui, Reviving the lithium metal anode for high-energy batteries. *Nature Nanotechnology*, **2017**, 12, 194.
[5] D. Linden, T. Reddy, *Handbook of Batteries*. (The McGraw-Hill Companies, Inc., ed. Third Edition, 2001).
[6] J. Lu, Z. Chen, F. Pan, Y. Cui, K. Amine, High-Performance Anode Materials for Rechargeable Lithium-Ion Batteries. *Electrochemical Energy Reviews*, **2018**, 1, 35.
[7] J. Xu, J. Ma, Q. Fan, S. Guo, S. Dou, Recent Progress in the Design of Advanced Cathode Materials and Battery Models for High-Performance Lithium-X (X = O2, S, Se, Te, I2, Br2) Batteries. *Adv Mater*, **2017**, 29, 1606454.
[8] U. Kasavajjula, C. Wang, A. J. Appleby, Nano- and bulk-silicon-based insertion anodes for lithium-ion secondary cells. *J Power Sources*, **2007**, 163, 1003.
[9] X. H. Liu, L. Zhong, S. Huang, S. X. Mao, T. Zhu, J. Y. Huang, Size-dependent fracture of silicon nanoparticles during lithiation. *ACS Nano*, **2012**, 6, 1522.
[10] M. T. McDowell, S. W. Lee, W. D. Nix, Y. Cui, 25th anniversary article: Understanding the lithiation of silicon and other alloying anodes for lithium-ion batteries. *Adv Mater*, **2013**, 25, 4966.
[11] W.-J. Zhang, Lithium insertion/extraction mechanism in alloy anodes for lithium-ion batteries. *J Power Sources*, **2011**, 196, 877.
[12] C. M. Park, J. H. Kim, H. Kim, H. J. Sohn, Li-alloy based anode materials for Li secondary batteries. *Chem Soc Rev*, **2010**, 39, 3115.
[13] W. Xu, J. Wang, F. Ding, X. Chen, E. Nasybulin, Y. Zhang, J.-G. Zhang, Lithium metal anodes for rechargeable batteries. *Energy Environ. Sci.*, **2014**, 7, 513.
[14] D. Aurbach, Review of selected electrode–solution interactions which determine the performance of Li and Li ion batteries. *Journal of Power Sources*, **2000**, 89, 206.
[15] D. Aurbach, E. Zinigrad, Y. Cohen, H. Teller, A short review of failure mechanisms of lithium metal and lithiated graphite anodes in liquid electrolyte solutions. *Solid State Ionics*, **2002**, 148, 405.
[16] R. Marom, S. F. Amalraj, N. Leifer, D. Jacob, D. Aurbach, A review of advanced and practical lithium battery materials. *Journal of Materials Chemistry*, **2011**, 21, 9938.
[17] Z. Liang, D. Lin, J. Zhao, Z. Lu, Y. Liu, C. Liu, Y. Lu, H. Wang, K. Yan, X. Tao *et al.*, Composite lithium metal anode by melt infusion of lithium into a 3D conducting scaffold with lithiophilic coating. *Proc Natl Acad Sci U S A*, **2016**, 113, 2862.
[18] K. Dong, M. Osenberg, F. Sun, H. Markötter, C. J. Jafta, A. Hilger, T. Arlt, J. Banhart, I. Manke, Non-destructive characterization of lithium deposition at the Li/separator and Li/carbon matrix interregion by synchrotron X-ray tomography. *Nano Energy*, **2019**, 62, 11.
[19] X. Guan, A. Wang, S. Liu, G. Li, F. Liang, Y. W. Yang, X. Liu, J. Luo, Controlling Nucleation in Lithium Metal Anodes. *Small*, **2018**, 14, 1801423.
[20] X. Yu, A. Manthiram, Electrode–electrolyte interfaces in lithium-based batteries. *Energy & Environmental Science*, **2018**, 11, 527.
[21] E. Peled, S. Menkin, Review—SEI: Past, Present and Future. *Journal of The Electrochemical Society*, **2017**, 164, A1703.
[22] E. Peled, The Electrochemical Behavior of Alkali and Alkaline Earth Metals in Nonaqueous Battery Systems—The Solid Electrolyte Interphase Model. *Journal of The Electrochemical Society*, **1979**, 126, 2047.
[23] Z. Zhang, S. Zhang, *Rechargeable Batteries*. (Springer, Cham, 2015), https://doi.org/10.1007/978-3-319-15458-9.

[24] M. S. Whittingham, Lithium Batteries and Cathode Materials. *Chem Rev*, **2004**, 104, 4271.
[25] G. E. Blomgren, The development and future of lithium ion batteries. *Journal of The Electrochemical Society*, **2017**, 164, A5019.
[26] A. Manthiram, Y. Fu, Y. S. Su, Challenges and Prospects of Lithium-Sulfur Batteries. *Acc Chem Res*, **2013**, 46, 1125.
[27] P. G. Bruce, S. A. Freunberger, L. J. Hardwick, J. M. Tarascon, Li-O2 and Li-S batteries with high energy storage. *Nat Mater*, **2011**, 11, 19.
[28] M. Hagen, D. Hanselmann, K. Ahlbrecht, R. Maça, D. Gerber, J. Tübke, Lithium-Sulfur Cells: The Gap between the State-of-the-Art and the Requirements for High Energy Battery Cells. *Adv Energy Mater*, **2015**, 5, n/a.
[29] A. Fotouhi, D. Auger, L. O'Neill, T. Cleaver, S. Walus, Lithium-Sulfur Battery Technology Readiness and Applications—A Review. *Energies*, **2017**, 10, 1937.
[30] Z. Yang, S. Wang, K. Dong, Y. Dai, X. Lei, Electrochemical characterization of sulfur with low depth of charge/discharge in lithium sulfur batteries. *Electrochimica Acta*, **2016**, 187, 629.
[31] S. S. Zhang, A review on the separators of liquid electrolyte Li-ion batteries. *Journal of Power Sources*, **2007**, 164, 351.
[32] C. J. Orendorff, The Role of Separators in Lithium-Ion Cell Safety. *The Electrochemical Society Interface*, **2012**, 21, 61.
[33] P. Arora, Z. Zhang, Battery separators. *Chemical Reviews*, **2004**, 104, 4419.
[34] K. Xu, Nonaqueous liquid electrolytes for lithium-based rechargeable batteries. *Chem Rev*, **2004**, 104, 4303.
[35] V. A. Agubra, J. W. Fergus, The formation and stability of the solid electrolyte interface on the graphite anode. *J Power Sources*, **2014**, 268, 153.
[36] X.-B. Cheng, C.-Z. Zhao, Y.-X. Yao, H. Liu, Q. Zhang, Recent Advances in Energy Chemistry between Solid-State Electrolyte and Safe Lithium-Metal Anodes. *Chem*, **2019**, 5, 74.
[37] N. Kamaya, K. Homma, Y. Yamakawa, M. Hirayama, R. Kanno, M. Yonemura, T. Kamiyama, Y. Kato, S. Hama, K. Kawamoto *et al.*, A lithium superionic conductor. *Nat Mater*, **2011**, 10, 682.
[38] A. Ulvestad, A Brief Review of Current Lithium Ion Battery Technology and Potential Solid State Battery Technologies. *arXiv e-prints*. 2018.
[39] F. Sun, K. Dong, M. Osenberg, A. Hilger, S. Risse, Y. Lu, P. H. Kamm, M. Klaus, H. Markötter, F. García-Moreno *et al.*, Visualizing the morphological and compositional evolution of the interface of InLi-anode|thio-LISION electrolyte in an all-solid-state Li–S cell by in operando synchrotron X-ray tomography and energy dispersive diffraction. *Journal of Materials Chemistry A*, **2018**, 6, 22489.
[40] T. Yamada, S. Ito, R. Omoda, T. Watanabe, Y. Aihara, M. Agostini, U. Ulissi, J. Hassoun, B. Scrosati, All Solid-State Lithium-Sulfur Battery Using a Glass-Type P2S5-Li2S Electrolyte: Benefits on Anode Kinetics. *Journal of the Electrochemical Society*, **2015**, 162, A646.
[41] C. Wang, Y. Zhao, Q. Sun, X. Li, Y. Liu, J. Liang, X. Li, X. Lin, R. Li, K. R. Adair *et al.*, Stabilizing interface between Li10SnP2S12 and Li metal by molecular layer deposition. *Nano Energy*, **2018**, 53, 168.
[42] M. R. Busche, D. A. Weber, Y. Schneider, C. Dietrich, S. Wenzel, T. Leichtweiss, D. Schröder, W. Zhang, H. Weigand, D. Walter *et al.*, In SituMonitoring of Fast Li-Ion Conductor Li7P3S11Crystallization Inside a Hot-Press Setup. *Chemistry of Materials*, **2016**, 10.1021/acs.chemmater.6b02163.
[43] Y. Zhu, X. He, Y. Mo, Origin of Outstanding Stability in the Lithium Solid Electrolyte Materials: Insights from Thermodynamic Analyses Based on First-Principles Calculations. *ACS Appl Mater Interfaces*, **2015**, 7, 23685.
[44] H. Chen, M. M. Rogalski, J. N. Anker, Advances in functional X-ray imaging techniques and contrast agents. *Phys Chem Chem Phys*, **2012**, 14, 13469.
[45] J. Banhart, *Advanced tomographic methods in materials research and engineering*. (Oxford University Press, 2008).

[46] M. Ebner, F. Marone, M. Stampanoni, V. Wood, Visualization and quantification of electrochemical and mechanical degradation in Li ion batteries. *Science*, **2013**, 342, 716.
[47] S.-C. Chao, Y.-C. Yen, Y.-F. Song, Y.-M. Chen, H.-C. Wu, N.-L. Wu, A study on the interior microstructures of working Sn particle electrode of Li-ion batteries by in situ X-ray transmission microscopy. *Electrochemistry Communications*, **2010**, 12, 234.
[48] K. J. Harry, D. T. Hallinan, D. Y. Parkinson, A. A. MacDowell, N. P. Balsara, Detection of subsurface structures underneath dendrites formed on cycled lithium metal electrodes. *Nat Mater*, **2014**, 13, 69.
[49] F. Sun, R. Moroni, K. Dong, H. Markötter, D. Zhou, A. Hilger, L. Zielke, R. Zengerle, S. Thiele, J. Banhart *et al.*, Study of the Mechanisms of Internal Short Circuit in a Li/Li Cell by Synchrotron X-ray Phase Contrast Tomography. *ACS Energy Letters*, **2017**, 2, 94.
[50] P. Pietsch, V. Wood, X-Ray Tomography for Lithium Ion Battery Research: A Practical Guide. *Annual Review of Materials Research*, **2017**, 47, 451.
[51] K. Dong, H. Markotter, F. Sun, A. Hilger, N. Kardjilov, J. Banhart, I. Manke, In situ and Operando Tracking of Microstructure and Volume Evolution of Silicon Electrodes by using Synchrotron X-ray Imaging. *ChemSusChem*, **2019**, 12, 261.
[52] W. Gorner, M. P. Hentschel, B. R. Muller, H. Riesemeier, M. Krumrey, G. Ulm, W. Diete, U. Klein, R. Frahm, BAMline: the first hard X-ray beamline at BESSY II. *Nucl Instrum Meth A*, **2001**, 467, 703.
[53] M. Klaus, F. Garcia-Moreno, The 7T-MPW-EDDI beamline at BESSY II. *Journal of large-scale research facilities JLSRF*, **2016**, 2.
[54] F. Garcia-Moreno, C. Jimenez, P. H. Kamm, M. Klaus, G. Wagener, J. Banhart, C. Genzel, White-beam X-ray radioscopy and tomography with simultaneous diffraction at the EDDI beamline. *J Synchrotron Radiat*, **2013**, 20, 809.
[55] C. Genzel, I. A. Denks, J. Gibmeier, M. Klaus, G. Wagener, The materials science synchrotron beamline EDDI for energy-dispersive diffraction analysis. *Nuclear Instruments and Methods in Physics Research Section A: Accelerators, Spectrometers, Detectors and Associated Equipment*, **2007**, 578, 23.

2. Parts of doctoral work

2.1 Microstructural evolution of silicon particles

K. Dong, H. Markötter, F. Sun *et al.*, *In situ* and *Operando* Tracking of Microstructure and Volume Evolution of Silicon Electrodes by using Synchrotron X-ray Imaging. *ChemSusChem*, **2019**, 12, 261-269. (DOI: 10.1002/cssc.201801969) [Accepted Version]

Own contribution: sample preparation and measurement; data analysis and results interpretation; manuscript composition and submission.

2.2 Lithium deposition at the Li/separator and Li/carbon matrix interregion

K. Dong, M. Osenberg, *et al*., Non-destructive Characterization of Lithium Deposition at the Li/Separator and Li/Carbon Matrix Interregion by Synchrotron X-ray Tomography. *Nano Energy,* **2019**, 62, 11-19. (DOI: 10.1016/j.nanoen.2019.05.022) [Accepted Version]

Own contribution: sample preparation and *in-situ* measurement; data analysis and results interpretation; manuscript composition and submission.

2.3 Nucleation and morphological transition of lithium deposition

K. Dong, M. Osenberg, J. Tan, *et al*, Quasi in-situ observation of nucleation and morphological transition of lithium electrodeposition in liquid electrolytes. *To be submitted*.

Own contribution: sample preparation and measurement; SEM data analysis and results interpretation; manuscript composition.

2.4 Morphological evolution at InLi/LISION interface

F. Sun, K. Dong, M. Osenberg *et al*., Visualizing Morphological and Compositional Evolution of Interface of InLi-anode|thio-LISION Electrolyte in All-Solid-State Li-S Cell by in operando Synchrotron X-ray Tomography and Energy Dispersive Diffraction. *J. Mater. Chem. A*, **2018**, 6, 22489-22496. (DOI: 10.1039/C8TA08821G) [F.S and K.D. contributed equally to this work.] [Accepted Version]

Own contribution: sample preparation and *operando* measurement; beamtime application; data analysis and results interpretation.

2.1 Microstructural evolution of silicon particles

K. Dong, H. Markötter, F. Sun *et al.*, In situ and Operando Tracking of Microstructure and Volume Evolution of Silicon Electrodes by using Synchrotron X-ray Imaging. *ChemSusChem*, **2019**, 12, 261-269. (DOI: 10.1002/cssc.201801969)

In situ and *Operando* Tracking of Microstructure and Volume Evolution of Silicon Electrode using Synchrotron X-ray Imaging

Kang Dong,*[a][b] Henning Markötter,[b] Fu Sun,[b] André Hilger,[b] Nikolay Kardjilov,[b] John Banhart,[a][b] Ingo Manke[b]

[a] Institute of Materials Science and Technology, Technical University Berlin, Hardenbergstraße 36, 10623 Berlin, Germany

[b] Helmholtz-Zentrum Berlin für Materialien und Energie, Hahn-Meitner-Platz 1, 14109 Berlin, Germany

*Email: kang.dong@helmholtz-berlin.de

Abstract

The internal microstructure of a silicon electrode in a lithium ion battery was visualized by operando synchrotron X-ray radioscopy during battery cycling. The silicon particles were found to change their sizes upon lithiation/delithiation and the changes could be quantified. It was found that particle volume change is related to its initial size, and is also largely determined by the changing surrounding electron conductive network and internal interface chemical environment (*e.g.* electrolyte migration, SEI propagation) within fractured particles. Moreover, an expansion prolongation phenomenon was discovered involving that some particles continue expanding even after switching the battery current direction and shrinkage would be expected, which is explained by assuming different expansion characteristics of particle cores and outer regions. The study provides new basic insights into processes inside Si particles during lithiation and delithiation and also demonstrates the unique possibilities of *operando* synchrotron X-ray imaging for studying degradation mechanisms in battery materials.

Keywords: Electrochemistry; microstructure evolution; *operando* radiography; silicon; volume change

Introduction

Advanced lithium-ion batteries with high capacity density, high rate capability, and excellent long life are crucial for next-generation energy storage systems, *e.g.* portable electronics, electric vehicles and hybrid electric vehicles.[1] Due to a relatively low specific capacity (372 $mAh \cdot g^{-1}$), traditional graphite-based anode material can hardly meet the future high capacity demand. Given the outstanding theoretical capacity of silicon (4200 $mAh \cdot g^{-1}$, approximately 10 times of the conventional graphite anode) the specific energy of silicon-based batteries could be significantly increased, leading to an improved portability and an extended service time after fully charging.[2] The abundance of silicon in nature and relatively low working potential provide a wide application prospect at an affordable price.

The alloying reaction between Si and Li^+ enables a much higher specific capacity, but is also accompanied by a large volume change. Assuming a silicon eletrode with the maximum possible alloying formula of $Li_{4.4}Si$, the corresponding maximum volume expansion is around 400% as calculated from the volume change of the crystal structure.[3] Both volume expansion and shrinkage during lithium insertion and extraction lead to repetitive strains and structural changes, which finally result in mechanical deformation and irreversible capacity fading of the whole electrode[2b]. Therefore, large volume change is widely regarded as the primary suspect for a short lifetime.

The formation of a solid-electrolyte interface (SEI) layer due to the decomposition of the organic electrolyte[2b, 4] is also widely regarded as another issue that contributes to fast degradation. Being an ionically conducting and electronically insulating layer it protects the electrode and electrolyte from further chemical side reactions and helps to stabilize the electrode/electrolyte interface. Unfortunately, the repetitive volume change or even pulverization of silicon during cycling would break down a previously formed SEI layer and re-expose fresh Si surface area to the electrolyte. As a result, the thickness of the surface interface increases and the irreversible charge “loss” derived from the unceasing development of SEI layer finally brings about gas generation[4c], low cycling efficiency and ongoing capacity decay.[2b] Fundamentally, the continuous development of SEI layer is mainly induced by the repetitive pulverization of silicon.

Based on the above two points, periodic expansion and shrinkage of silicon particles can be plausibly summarized as the main cause for the consecutive capacity fading and low coulombic efficiency throughout the electrode’s lifetime.

Numerous efforts from the perspective of advanced materials have contributed to improve capacity retention and suppress fast capacity fading. One effective approach is to employ nm-scale active materials with various geometries[5], ranging from nanoparticles,[6] nanowires,[7] nanotubes[8], to thin Si films[9]. By utilizing such nanomaterials, volume changes can be effectively accommodated, and de/lithiation significantly promoted due to shortened electron transport and lithium ion diffusion distances. Due to the relatively low electronic conductivity of Si (approx. 0.1 $S \cdot m^{-1}$)[10], varieties of the carbon matrix (*e.g.* porous carbon[11], CNTs,[12] and graphene[13]) are introduced to increase electronic conductivity. Miscellaneous strategies based on Si/carbon architectures, *e.g.* coating[14], encapsulation[15], core/yolk-shell[16] have been designed to enhance the conductivity and structural stability of electrodes. Building such novel material architectures has markedly improved the cycling capacity and stability.

The understanding of de/lithiation and the accompanying volume change has also been promoted by atomic-scale first-principles simulations.[17] In spite of this, in-depth experimental studies related to the internal periodic microstructure evolution have rarely been reported, which is mainly due to the lack of applicable characterization techniques and the rigorous measurement conditions. Using *in situ* transmission electron microscopy (TEM), J. Huang *et al*[18] observed that the fracture of silicon nanoparticles during lithiation is size-dependent, indicating that particles larger than 150 nm undergo cracking while smaller ones do not. Similarly but via in situ X-ray transmission microscopy (TXM), core-shell reactions of Sn, another alloy electrode material from Group IV like silicon, were found to be associated with the formation of cracks.[19] The expansion of Sn particles was also shown to depend strongly on particle size. Recently, synchrotron X-ray imaging has been successfully employed to visualize and quantify the microstructural dynamics of silicon electrode[20] and other alloy-reaction electrode materials[21] to reveal the electrode degradation. However, the periodic microstructure evolution of silicon, which is crucial to comprehend the electrode failure mechanisms, is not yet well understood.[3, 10, 22]

In the present study, *in situ* and *operando* synchrotron X-ray imaging was employed to visualize the internal microstructure evolution and to quantify the volume change during battery operation. Compared to destructive and post-mortem characterization, this unique technique reveals morphological information non-destructively and non-invasively.[21, 23] We present time-lapse X-ray radioscopy (dynamic X-ray radiography) of the microstructure evolution of silicon particles during the first de/lithiation as well as of degradation during subsequent cycling. Contrary to a previous report based on simulation[17c], the expansion and shrinkage of silicon particles are demonstrated to be nonlinear with lithium insertion during battery cycling. In addition, a volume "expansion prolongation" effect of silicon electrode is proposed and quantified, which is further explained based on the hypothesis of different expansion characteristics of particle cores and outer regions.

Results and Discussion

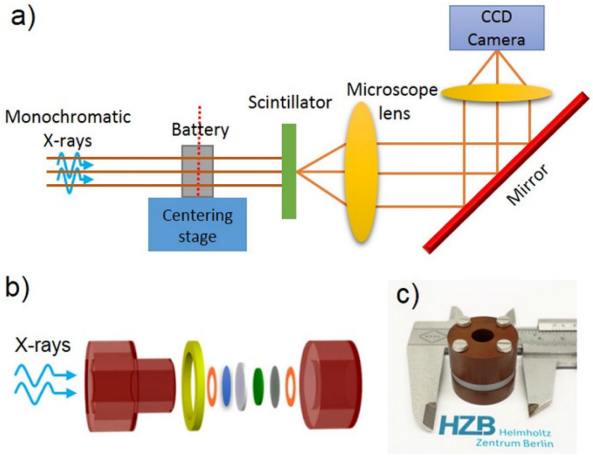

Figure 1. Synchrotron X-ray imaging. (a) Schematic of the synchrotron X-ray imaging setup; (b) sketch and (c) photograph of a cell customized for *operando* synchrotron X-ray imaging. From left to right in b) are, housing (claret-red), sealing ring (yellow), copper ring (orange), lithium plate (blue), separator (light grey), Si/carbon/binder composite (green) titanium foil (dark gray, current collector), copper ring (orange), lower housing (claret-red).

To track changes during battery operation, a custom-built cell (Fig. 1b and 1c) made of a largely X-ray transparent material with good sealing and mechanical stability, was used. Monochromatic synchrotron X-rays passed through the battery perpendicular to the material layers as shown in Fig. 1b. The beam was directed through the hole of the upper housing of the cell, which is designed to avoid undesired X-ray absorption. A projection image of the battery is created on a scintillator, converted to light there and subsequently imaged with a microscope lens system, a mirror and a CCD camera (Fig. 1a). As the attenuation coefficient of silicon (43 cm^{-1}) is far higher than that of the other materials such as carbon/binder composite, separator and lithium (~0.13 cm^{-1}) at an X-ray energy of 12 keV, silicon particles absorb much more X-rays, which enables us to clearly distinguish the silicon particles from the electrode composite and other components within the battery.

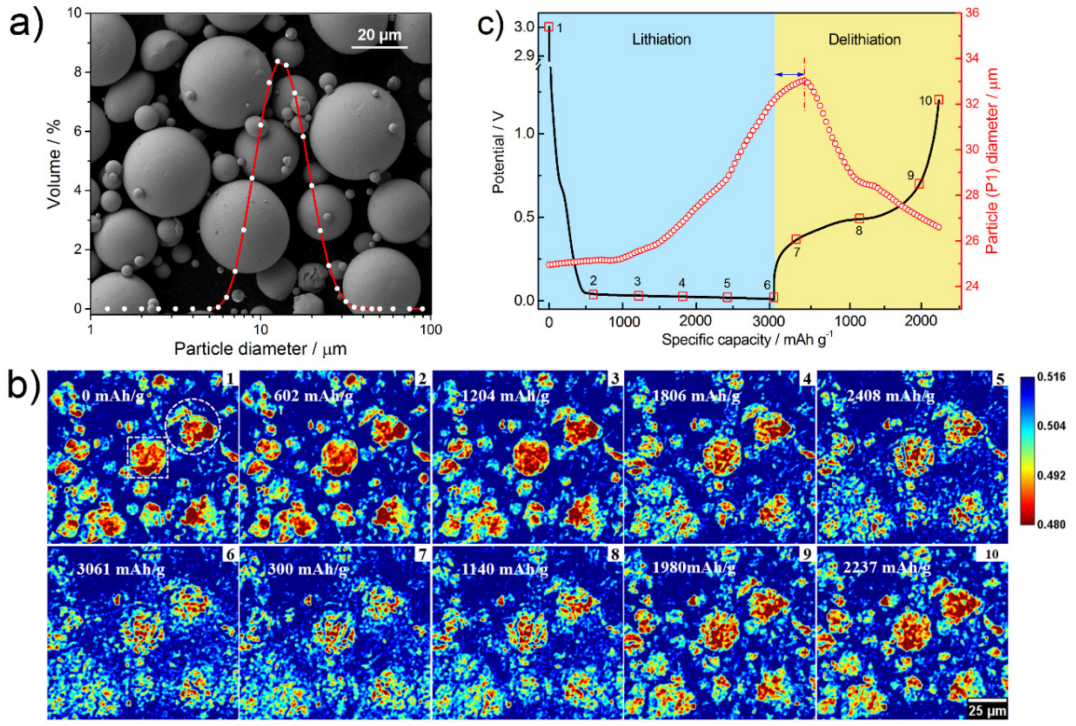

Figure 2. Microstructure evolution. (a) SEM image and particle size distribution of silicon particles; (b) Ten transmission images of the microstructure evolution of silicon particles during the first lithiation (1 to 6) and delithiation (6 to 10), related to the 10 states highlighted by red squares on the potential curve in Fig. 2c. The color scale encodes transmission; (c) First lithiation and delithiation curve (black line) of silicon electrode at a current density of 192.8 mA/g, and the diameter changes (red circle) of the central particle (S1) in Fig. 2b.

Commercial silicon powder with a particle diameter distribution ranging almost from 6 to 30 µm was used for the active anode material. Scanning electron microscopy in Fig. 2a and Fig. S1 gives an impression of the particle morphology. The de/lithiation behavior of silicon particles was compared by selecting silicon particles with various diameters in the images for analysis. Galvanostatic charge-discharge was conducted simultaneously with *operando* synchrotron X-ray imaging to observe the corresponding morphological changes at different de/lithiation states.

In Figure 2b, ten representative states during the first cycle are displayed. They correspond to the states highlighted by red squares on the dis/charge curve in Fig. 2c. A color calibration bar in Fig. 2b represents transmission values, which depend on the mass density and elemental composition of the corresponding investigated region. Particles with a high degree of lithiation will display high transmission and vice versa. In the pristine state, the central particle (denoted as P1), which is marked by a white rectangular in Fig. 2b at 0 $mAh \cdot g^{-1}$, shows inhomogeneous shades pointing at inhomogeneities in the particle density caused by, *e.g.*, the rough surface with slight bulges or overlap with smaller silicon particles. During lithiation from the pristine state to 602 $mAh \cdot g^{-1}$, it seems that the particle remains intact without showing visible cracks. This also applies to the particle marked by a white circle in the first image of Fig. 2b. After that until the end of lithiation to 3061 $mAh \cdot g^{-1}$, the particle (P1) begins to crack

from its surface, and the cracks propagate progressively towards the core. A movie displaying the particle fracture can be found in the supporting information (Movie. S1). As $Li_{4.4}Si$ is the maximum lithiation stage of Si, corresponding to the theoretical capacity of 4200 $mAh \cdot g^{-1}$, we calculate that for each silicon atom, ~3.2 Li ions have been inserted on average by the end of lithiation based on the measured lithiation capacity of 3061 $mAh \cdot g^{-1}$. The average chemical formula therefore is $Li_{3.2}Si$ assuming a homogeneous alloying reaction.

During the first lithiation (Fig. 2b1-2b6), nearly all the visible particles in Fig. 2b with different initial diameters transform to pulverized granules. Small particles are almost completely lithiated while large particles tend to preserve partially unlithiated granules. Incomplete lithiation of larger particles could be the main reason for the difference between the practical lithiation capacity (3061 $mAh \cdot g^{-1}$) and the theoretical capacity (4200 $mAh \cdot g^{-1}$). Disruption of the particles could bring in internal fragments conductively isolated from the electron network and thus deteriorate electron transfer inside the particle. It also inevitably leads to the inward propagation of the SEI layer and low coulombic efficiency. Furthermore, fracture of particles significantly contributes to the volume expansion of the electrode not only laterally within the electrode plane but also in the longitudinal direction (i.e. perpendicular to the plane shown in Fig. 2b). Consecutive accumulation of strain and stress on other battery components is induced, which apparently has a negative impact on maintaining the microstructure integrity of silicon particles as well as the reversibility of the structural changes of the silicon electrode in the long term.[24]

During subsequent delithiation, which is shown in the second row in Fig. 2b, the fragmented granules tend to recover back to the previous particle shape. The cracks between the granules disappear stepwise with lithium being extracted from the Li_xSi accompanied by a decrease in transmission. The recovery/shrinkage of a particle can be attributed to the release of accumulated strain and stress during lithiation caused by particle expansion.[24-25] Eventually the particles transform roughly to their original shape but still exhibit a few visible fractures. After the first delithiation, only ~73% of the pre-lithiated capacity was recovered, as calculated through the ratio of the first delithiation (2237 $mAh \cdot g^{-1}$) and the first lithiation capacity (3061 $mAh \cdot g^{-1}$). According to the delithiation capacity (2237 $mAh \cdot g^{-1}$) and the higher transmission after dealloying we estimate that some lithium remains trapped within the particles without full extraction as well as the lithium involves in the reaction at the SEI layer. This is further demonstrated by the dynamic behavior of the histogram of the transmission through particle P1 in Fig. 3.

The black line in Fig. 2c shows a typical first lithiation and delithiation curve under galvanostatic cycling with a fixed current density of 192.8 mA/g (calculated based on Si weight). The particle diameter of the central particle (P1) is also given as a function of the lithiation and delithiation capacity. Detailed process of particle measurement was

described in experimental section. The particle expands and shrinks during lithiation and delithiation, respectively, in different stages. Contrary to previous report[17c] based on simulation, the expansion and shrinkage of silicon particles are demonstrated herein to be nonlinear with lithium insertion during battery cycling. During the initial stage of lithiation ($0 \leq Q_{lithiation} \leq 800$ mAh·g^{-1}), the particle diameter shows little variation in accordance with Fig. 2b1 to Fig. 2b3 where no apparent particle shape change can be observed. This initial lithiation stage corresponds to an notable voltage drop including a short kink (~ 0.65 V) in Fig. 2c. During the initial voltage drop, an SEI layer forms on the surface of the silicon particles. Note that even at the beginning of the lithiation reaction plateau ($480 \leq Q_{lithiation} \leq 800$ mAh/g) where the particle is supposed to expand, the particle diameter still remains without a notable increase. In later stages ($Q_{lithiation} >$ 800 mAh/g), the particle diameter increases at an increasing rate. The particle diameter does not stop increasing immediately after the current direction has been reversed but keeps climbing for a period after current reversion and maintains that tendency for approximately 400 mAh·g^{-1} (~124 minutes). The time/capacity between the start of delithiation and reaching the maximum particle diameter is thereafter named "expansion prolongation" period and is highlighted by the blue arrow in Fig. 2c. We note that a same extended expansion phenomenon during delithiation was reported before but without detailed explanasion.[26] Further exploration and interpretation of this phenomenon are presented in this paper together with Fig. 4 and Fig. 5.

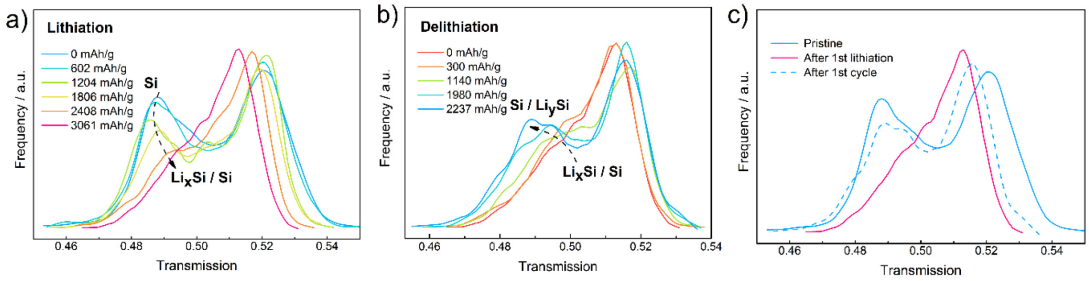

Figure 3. Evolution of chemical components. Histograms of X-ray transmission for all pixels within a white box (highlighted in Fig. S2) around P1 during (a) lithiation, (b) delithiation and (c) comparison of pristine state and states after 1st lithiation and 1st cycle. Smaller transmission values can be attributed to silicon while higher values represent the surrounding electrode material matrix apart from silicon. The arrows indicate peak movements during the electrochemical reaction.

Due to the pronounced differences of attenuation coefficients between silicon and the other battery components it is possible to reveal the evolution of chemical components during cell operation. Figures 3a and 3b show the evolution of chemical components within the region highlighted in Fig. S2 during lithiation and delithiation, respectively. Two peaks with transmissions of about 0.485 and 0.52 are observed both during lithiation and delithiation. The left peak at lower transmission can be ascribed to P1 (low X-ray transmission for Si), whereas the right peak corresponds to more transparent materials such as lithium, carbon and electrolyte, which we denoted as background.

With progressing lithiation the silicon-related peak shifts to higher transmissions while broadening. The background peak (~0.52) first decreases in intensity and later shifts towards lower transmissions, which should be attributed to the expansion of particle P1 and the consumption of lithium electrode during lithiation. At the end of lithiation (3061 $mAh \cdot g^{-1}$, Fig. 3a) the silicon peak has evolved into a shoulder of the background peak. This further demonstrates an incomplete first lithiation and is in good agreement with the analysis of the practical lithiation capacity in Fig. 2c. In addition, the broad left shoulder of the background peak reveals that there might be few Si particles that were not involved in lithiation and co-exist with Li_xSi ($x < 4.4$) after lithiation. Thus the chemical composition of the active materials at the end of lithiation should be denoted as Li_xSi/Si in Fig. 3a. During delithiation in Fig. 3b, the histogram of the lithiated state (0 $mAh \cdot g^{-1}$, red line) develops into two main peaks again (around 0.485 and 0.51). At the end of delithiation (2237 $mAh \cdot g^{-1}$, blue line) a second small shoulder peak appears around 0.485 transmission. The appearance of this shoulder peak reveals that some active material was not fully delithiated as some lithium is trapped in the active material (Li_ySi/Si) during delithiation, which can be derived from a comparison between the pristine state and the state after the 1st cycle shown in Fig. 3c. This leads to a lower delithiation capacity and thus contributes to the decay of the cycling performance in long-term battery operation. It would be highly valuable to quantify x and y in Li_xSi/Si and Si/Li_ySi and thus be possible to compare the de/lithiation depth of single particles with that of the whole electrode. Synchrotron X-ray tomography technique is able to achieve this and is feasible especially for the alloy-based electrode materials (*e.g.* Ge and Sn) with less cracks during de/lithiation, which requires a newly designed battery but can precisely quantify the beam attenuation value of each voxel of the single particles.

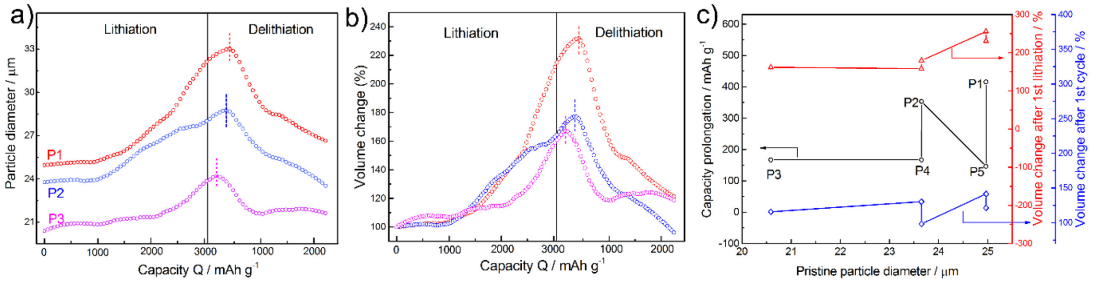

Figure 4. Particle diameter change and volume expansion. (a) Particle diameter change and (b) volume change during the first cycle of three particles including particle P1 (red curve); (c) the capacity of expansion prolongation (black), and the volume change (compared to the pristine volume) of five particles after the first lithiation (red) and after the first cycle (blue) as a function of pristine diameter; scatters connected with lines are used showing the particle sequence with diameter increasing, in order to differentiate particles with similar diameters around 23.7 and 25.0 µm and easily locate each particle's corresponding Y value on other plots in Fig. 4c.

Note that this extended expansion period was previously discovered when monitoring volumetric changes in Si thin-film.[26] A similar phenomenon, but an early termination of particle's volume expansion was presented about $Si_{0.64}Sn_{0.36}$ alloy[27] and Sn electrodes[28]. Despite these previous reports, the asynchronization of particles' volume change with the dis/charging state of electrode is as yet rarely investigated, especially quantitatively. In Fig. 4a and 4b, the diameter development of particle P1 (in Fig. 2c) and diameter/volume variation of another two particles (denoted as P2 and P3, as shown in Fig. 4a and Fig. S3) during lithiation and delithiation are shown for comparison. From the beginning of lithiation until a capacity of 1000 $mAh \cdot g^{-1}$, a period with almost unchanged diameter and less than 10 % expansion is observed in all three particles. After this, the smallest particle (P3) expands slightly up to 2000 $mAh \cdot g^{-1}$, while the diameters of the other two particles increase markedly and do not stop growing even until a delithiation capacity of 400 $mAh \cdot g^{-1}$ after changing the current polarity. The points in time when these three particles reach their maximum sizes (i.e. the expansion prolongation period) differ as indicated by the dashed lines in Fig. 4a. After reaching a maximum size, all three particles undergo a pronounced diameter reduction followed by a stage of decreased shrinkage rate until the end of delithiation.

The volume change of the corresponding three particles is given in Fig. 4b assuming that the particles are spherical. As mentioned previously, the first lithiation capacity of the whole electrode is 3061 $mAh \cdot g^{-1}$, which corresponds to an average of 3.2 Li-ions inserted for each silicon atom. The volume expansion of the pristine particles with diameters of 20.6 and 23.7 µm are roughly around 170%, which is far less than the theoretical volume change of 336% calculated by assuming similar Li-ion (3.25 Li-ions) insertion into Si as into the alloying product ($Li_{3.25}Si$).[3] Even the biggest volume change of the three particles during the first cycle is only around 232%. This plot demonstrates how volume expansion varies with particle diameter.

To further explore potential factors determining expansion prolongation two more particles (denoted as P4 and P5 in Fig. 4c and Fig. S3) were analyzed in addition to the three particles shown in Fig. 4a and 4b. Figure 4c gives the expansion prolongation capacities (black), the volume expansion during lithiation (red), and the volume change after the first cycle (blue) of five different particles. These five particles have initial particle diameters of 20.6, 23.7, 23.7, 25.0, 25.0 µm. Radiographs of initial states of the five particles can be found in Fig. S3. In Fig. 4c, the expansion prolongation effect can be observed on all five particles. The expansion prolongation period varies and does not show a general strict correlation with the pristine particle diameter. This is also the case with the volume change after the first cycle (blue line in Fig. 4c). For particles with similar pristine diameters (~23.7 and 25.0 µm), apparent differences of the expansion prolongation and the volume shrinkage can be observed.

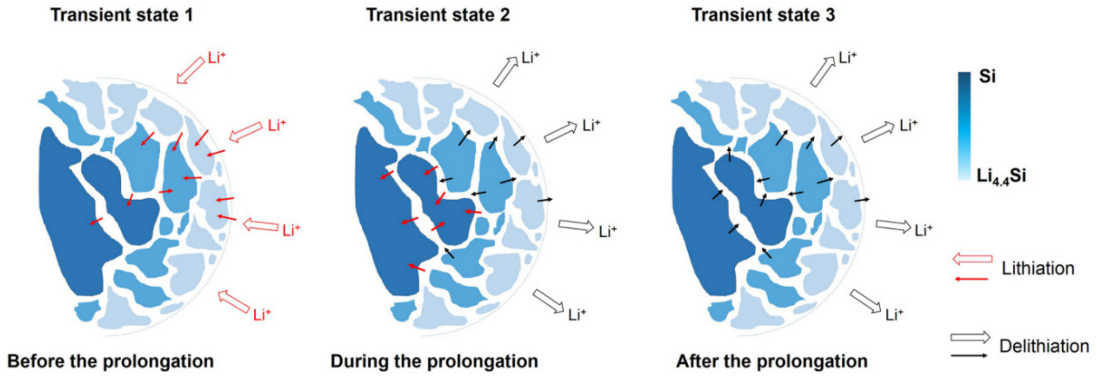

Figure 5. Mechanism of lithiation prolongation. Schematic illustration of three transient states: The lithium migration just before, during and after the expansion prolongation; arrows indicate the Li^+ migration directions.

For every individual Si particle, the maximum expansion and shrinkage should have a positive correlation with the depth of silicon de/lithiation, which will also be affected by the constantly changing environment (*e.g.* electrolyte, conducting network, stress/strain) during de/lithiation. To get the silicon particles de/lithiated deeply for higher capacities, excess conductive carbon (45 wt %) and electrolyte (137 ml/mg $_{Si}$) and a low current density (192.8 mA/g, i.e. 0.046 C) are utilized. Except for the initial particle diameter, all these external factors could largely affect the de/lithiation degree and lead to varying volume change behavior, as shown in Fig. 4. But these factors do not convincingly explain why five randomly picked individual particles all keep expanding for a significant period (i.e. 400 $mAh \cdot g^{-1}$ in Fig. 2c) during delithiation instead of reversing in volume immediately after the current direction has been reversed.

Based on the observations of microstructure evolution in Fig. 2b we assume that the main reason for expansion prolongation is attributed to a prolonged lithiation of the inner core of the particles as the schematic in Fig. 5 shows. During initial lithiation, particles appear intact without observable cracks. However, with progressing lithiation cracks appear and propagate towards the particle core, and connections between the shell and the central core weaken. This means that the shell of a particle can be lithiated easier and a lithium concentration gradient along the radius of the particle may exist even until the end of lithiation as represented by transient state 1 in Fig. 5 just before inverting the current direction. Due to fracture propagation the fresh cracks provide diffusion tunnels for Li^+ ions to migrate through the particles towards their core regions, which allows for faster Li^+ migration paths and relatively easier lithiation. After inversion of the current the whole particle is subjected to delithiation and Li^+ starts to be extracted from the whole particle as the black arrows in Fig. 5 outside the particle indicate. However, due to the inhomogeneous lithium distribution within the cracked particle the less lithiated inner parts could still react with Li^+ ions although the whole particle is being delithiated. This prolonged lithiation progress inside the particle during electrode delithiation is represented by red arrows in transient state 2 in Fig. 5. Hence, the inner parts still continue to expand while the outer fractures are supposed to shrink.

The former process dominates the whole volume change during this period. With the inner core getting more lithiated the expansion of the inner core slows down due to the increasing lithiation depth of the particle and decreasing concentration gradient. This means that lithium within the particle tends to distribute more homogeneously. The particle diameter reaches its maximum value after the core expansion no longer dominates. The whole particle expansion prolongation ends at the same instant followed by a volume shrinkage of the particle as the transient state 3 in Fig. 5 shows. Hence, particle size and tortuosity of the crack structure within the particle largely determine the prolongation time. Compared to the lithiation behavior of silicon, cracks can also be observed in Ge and Sn particles but they tend to preserve the particles' integrity instead of pulverization.[21, 29] Although inhomogeneous lithiation within the particle should be the root cause for the expansion prolongation even if there are no cracks during lithiation, the cracks bring about the migration of Li ions within the particle, thus enable an easier lithiation prolongation even after the inverse of current and lead to an apparent observation of expansion prolongation. Therefore, the volume expansion prolongation of Ge or Sn is supposed to exist but would be harder to be observed than silicon.

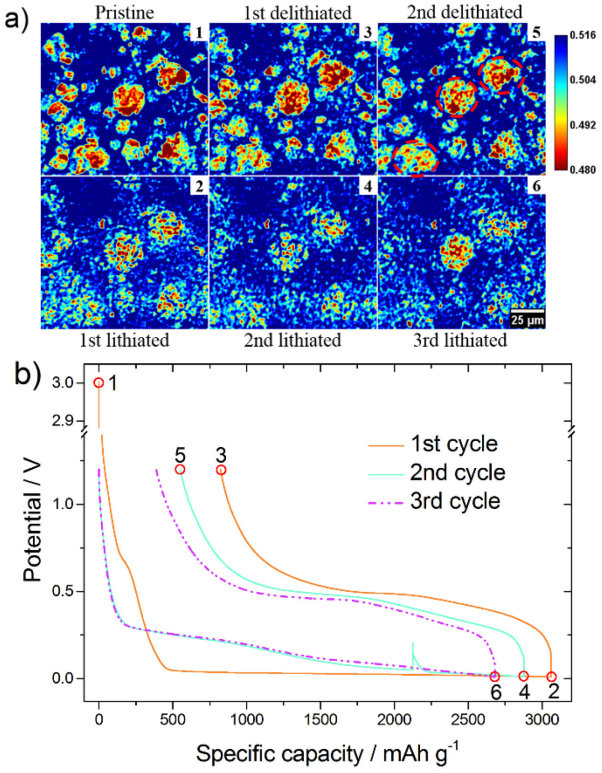

Figure 6. Evolution of particle fracture. (a) The pristine state and the following five de/lithiated states during cycling; (b) potential plots during lithiation and delithiation of first three cycles. The six projections shown in Fig. 6a correspond to the six de/lithiated states marked by small red circles in Fig. 6b. The small voltage peak during the second lithiation is caused by stopping and resuming battery operation after an unscheduled X-ray interruption.

2.1 Microstructural evolution of silicon particles

We now turn our attention to the evolution of silicon particles during consecutive cycling. Projections of the pristine state at the end of each lithiation and the end of each delithiation state during the first three cycles are collected together for comparison in Fig. 6a. These six transient states are highlighted on the discharge and charge diagrams in Fig. 6b by red circles and labeled with the corresponding numbers ranging from 1 to 6. In the top row, when comparing the delithiated silicon with the pristine state, the particles marked by dashed red circles in the 2nd delithiated state all tend to have more cracks and expansion than the corresponding previous delithiated state, indicating progressive irreversible structural deterioration, while allowing for a deeper delithiation. This agrees well with the higher capacity of the 2nd delithiation (2323 mAh·g^{-1}) than the first one (2233 mAh·g^{-1}).

When focusing on the three lithiated states (Fig. 6a2, 6a4 and 6a6), all the smaller particles tend to get deeply lithiated corresponding to severe particle fracture and high X-ray transmission at the end of each lithiation. In contrast, the particle in the center had different lithiation degrees among the three cycles. It was relatively more lithiated during 2nd lithiation and less lithiated during 3rd lithiation. This reveals that the reaction activity of single silicon particles fluctuates during consecutive cycling. The lithiation capacity of the whole electrode kept decreasing constantly with the three lithiation capacities from 3054 mAh·g^{-1}, over 2910 mAh·g^{-1} to 2674 mAh·g^{-1}, respectively.

With repetitive fracture and shrinkage of silicon particles, inner isolated fragments of big particles accumulate during cycling and thus contribute to the continuous loss of lithiation capacity. Meanwhile, repetitive fracture creates fresh silicon surfaces and the electrolyte is continuously consumed to form new SEI layers on the fragments. As a result, a high ionic migration impedance due to electrolyte consumption could easily bring about electrochemical polarization and capacity decay. Besides degeneration of the particle microstructure, the periodic accumulation and release of strain and stress due to the volume change of silicon particles could cause an unstable electron conductive network, which also could contribute to capacity fading in long-term battery operation. Compared to the synergistic effect of several factors that leads to capacity loss, expansion prolongation largely and directly results from the different expansion characteristics of particle cores and outer regions (i.e. lithium concentration gradient along the radius of the particle). In principle, smaller particles could generally result in higher capacity due to a high de/lithiation degree, which is also revealed by Fig. 6. By utilizing nm-sized silicon, severe fracture and pulverization could be potentially avoided but this needs to be further confirmed by *operando* imaging techniques at a higher resolution. Therefore, a flexible and stable carbon/binder matrix with nm-sized homogeneously dispersed silicon and pre-reserved space for silicon expansion is a promising strategy for silicon electrode design.

Conclusions

The interior dynamic microstructure evolution of a silicon electrode during battery cycling was investigated and visually illustrated by means of operando synchrotron X-ray radiography. Dynamic imaging clearly shows microstructure evolution, volume expansion and shrinkage of individual Si particles during lithiation and delithiation. The expansion/shrinkage behavior is found to be related to the initial particle size but does not show a direct relationship with de/lithiation depth. The changing electron conductive network and interface chemical environment (*e.g.* electrolyte migration, SEI propagation) within fractured particle might be a determining factor in the volume change of silicon particles in practical battery operation. An expansion prolongation phenomenon after the end point of lithiation was observed and quantified. This effect should be taken into consideration when optimizing the accommodation space for μm-sized silicon particles to avoid volume changes without sacrificing energy density of the silicon electrode. These results contribute to comprehending the degradation and failure of silicon electrodes and also other alloying anodes and may enable a more targeted design and optimization of alloying anodes with superior performance.

Experimental Section

1. Materials

Silicon particles were obtained from Elkem AS, Norway. Titanium foil was received from ANKURO Int. GmbH, Germany. Carbon black, polyvinylidene difluoride (PVDF), Celgard separator and metallic lithium were purchased from MTI Corp. USA. 1 M $LiPF_6$ with a mixture of ethylene carbonate (EC) and ethyl methyl carbonate (EMC) (1:1, v/v) and N-methyl pyrrolidone solvent (NMP) were purchased from Sigma-Aldrich. The housing for the battery made of polyamide-imide (Torlon) was received from McMaster-Carr Company.

2. Battery assembly

Silicon particles, carbon black and PVDF with a mass ratio of 45:45:10, were mixed together and then dispersed in NMP, followed by stirring to obtain a homogeneous slurry. A titanium foil (ANKURO, Germany) of 5 μm thickness and good electrochemical stability (Fig. S4), was employed as the active material carrier. It has a high X-ray transmission of 85.7% at 12 keV and therefore enables good image contrast. Two copper rings of 6 mm inner diameter were used as the current collectors lying outside the field of view. The detailed structure of the battery is shown in Fig. 1

To build the cathode electrode, the slurry was cast onto the titanium foil (8 mm × 6mm) and subsequently dried in an oven at 60 °C. The battery was constructed by sandwiching Celgard 2325 separator between the cathode electrode (1.625 mg) and a lithium foil (diameter 10 mm) with 100 μl electrolyte employed.

3. Characterization

Synchrotron X-ray imaging was conducted at the BAMline at the BESSY II electron storage ring of the Helmholtz-Zentrum Berlin, Germany.[30] The synchrotron beam was monochromatized to an energy of 12 keV with a double multilayer monochromator that provided an energy resolution of about $\Delta E/E = 1.5\%$. The detector system comprised a 60-µm thick $CdWO_4$ scintillator, a microscopic optic and a PCO4000 camera with a 4008 × 2672 pixel CCD detector. (1.7 × 1.2) mm^2 field of view was captured with a pixel size of 0.438 µm. Each projection was obtained within an exposure time of 120 s with a time interval of around 6.45 min between two projections while the charging/discharging process was continuously running.

The morphology of the silicon and carbon black composite was investigated using a Zeiss LEO Gemini 1530 scanning electron microscope (SEM). The X-ray diffraction measurement was performed on a Bruker D8 Advance. The particle size distribution of silicon was provided and conducted by Elkem AS Company using laser diffraction analysis on a Malvern Mastersizer 2000. Galvanostatic cycling of the cells was conducted using an Ivium CompactStat station, Iviumtechnology. Cyclic voltammetry (CV) tests were performed on a Gamry Interface 1000.

4. Data processing

The obtained raw image data were firstly processed for beam normalization with flatfield and darkfield projections and then for intensity normalization as well as drift/movement correction. Subsequently, a Gaussian blur filter (radius 2) was used followed by given pseudo color (inverted “Jet” Lookup Table in ImageJ) to obtain a deeper visual impression of the detailed microstructure evolution using the software ImageJ.

The dynamic diameter measurement was also conducted using software ImageJ. First, a line was drawn across a particle at the pristine state, as shown in Fig. S2. Specifically, the line was set with a width of 5 pixels rather than 1 pixel to make the line pass through the particle center and thus get an improved precision. While plotting the transmission value aross the particle along the line, the particle border (red dash circle in Fig. S2) was properly identified by setting a threshold (c.a. 0.504) of the transmission value, and thus the line was cut off by the particle’s border, generating a line segment across the particle through particle center. The particle diameter was regarded as the length of line segment, which could be acquired by multiplying one pixel size by the sum of the pixels of the line segment. The particle diameter at transient state was then plotted against time using the ImageJ plugin “dynamic Z-profiler” to obtain the dynamic diameter evolution with battery dis/charging. Due to particle movements during expansion and shrinkage as well as the influence of the movement of surrounding particles, a smooth filter of Savitzky-Golay was applied to the plot with a 50 point window and a polynomial order of 2.

Acknowledgments

This work was sponsored by the Helmholtz Association and the China Scholarship Council (CSC). We would gratefully acknowledge Helmholtz-Zentrum Berlin for the beam time allocation at BAMline and Dr. Heinrich Riesemeier and Ralf Britzke for technical support. The authors would also like to thank Dr. Anna Manzoni and De Ning for SEM and XRD measurements as well as Elkem AS Company for providing samples.

References

[1] a) M. Armand, J.-M. Tarascon, *Nature* **2008**, *451*, 652-657; b) M. S. Whittingham, *Chem Rev* **2004**, *104*, 4271-4302; c) C. M. Park, J. H. Kim, H. Kim, H. J. Sohn, *Chem Soc Rev* **2010**, *39*, 3115-3141; d) M. T. McDowell, S. W. Lee, W. D. Nix, Y. Cui, *Adv Mater* **2013**, *25*, 4966-4985.
[2] a) V. A. Sethuraman, V. Srinivasan, A. F. Bower, P. R. Guduru, *Journal of The Electrochemical Society* **2010**, *157*, A1253; b) A. Casimir, H. Zhang, O. Ogoke, J. C. Amine, J. Lu, G. Wu, *Nano Energy* **2016**, *27*, 359-376.
[3] U. Kasavajjula, C. Wang, A. J. Appleby, *J Power Sources* **2007**, *163*, 1003-1039.
[4] a) D. Aurbach, B. Markovsky, G. Salitra, E. Markevich, Y. Talyossef, M. Koltypin, L. Nazar, B. Ellis, D. Kovacheva, *Journal of Power Sources* **2007**, *165*, 491-499; b) T. Yoon, M. S. Milien, B. S. Parimalam, B. L. Lucht, *Chem Mater* **2017**, *29*, 3237-3245; c) F. Sun, H. Markötter, I. Manke, A. Hilger, N. Kardjilov, J. Banhart, *ACS Appl Mater Interfaces* **2016**, *8*, 7156-7164.
[5] X. Zhang, X. Qiu, D. Kong, L. Zhou, Z. Li, X. Li, L. Zhi, *ACS Nano* **2017**, *11*, 7476-7484.
[6] a) S. W. Lee, M. T. McDowell, L. A. Berla, W. D. Nix, Y. Cui, *Proc Natl Acad Sci U S A* **2012**, *109*, 4080-4085; b) H. Kim, B. Han, J. Choo, J. Cho, *Angew Chem Int Ed Engl* **2008**, *47*, 10151-10154.
[7] a) C. K. Chan, H. Peng, G. Liu, K. McIlwrath, X. F. Zhang, R. A. Huggins, Y. Cui, *Nat Nanotechnol* **2008**, *3*, 31-35; b) H. Wu, G. Chan, J. W. Choi, I. Ryu, Y. Yao, M. T. McDowell, S. W. Lee, A. Jackson, Y. Yang, L. Hu, Y. Cui, *Nat Nanotechnol* **2012**, *7*, 310-315.
[8] a) M. H. Park, M. G. Kim, J. Joo, K. Kim, J. Kim, S. Ahn, Y. Cui, J. Cho, *Nano Lett* **2009**, *9*, 3844-3847; b) Y. Son, S. Sim, H. Ma, M. Choi, Y. Son, N. Park, J. Cho, M. Park, *Adv Mater* **2018**, *30*, 1705430.
[9] a) T. Takamura, S. Ohara, M. Uehara, J. Suzuki, K. Sekine, *J Power Sources* **2004**, *129*, 96-100; b) J. Yin, M. Wada, K. Yamamoto, Y. Kitano, S. Tanase, T. Sakai, *Journal of The Electrochemical Society* **2006**, *153*, A472.
[10] X. Su, Q. Wu, J. Li, X. Xiao, A. Lott, W. Lu, B. W. Sheldon, J. Wu, *Advanced Energy Materials* **2014**, *4*, 1300882.
[11] a) J. Guo, X. Chen, C. Wang, *Journal of Materials Chemistry* **2010**, *20*, 5035; b) A. Esmanski, G. A. Ozin, *Advanced Functional Materials* **2009**, *19*, 1999-2010.
[12] a) W. Wang, P. N. Kumta, *ACS Nano* **2010**, *4*, 2233-2241; b) C. Martin, O. Crosnier, R. Retoux, D. Bélanger, D. M. Schleich, T. Brousse, *Advanced Functional Materials* **2011**, *21*, 3524-3530.
[13] X. Zhou, Y.-X. Yin, L.-J. Wan, Y.-G. Guo, *Advanced Energy Materials* **2012**, *2*, 1086-1090.
[14] J.-K. Yoo, J. Kim, Y. S. Jung, K. Kang, *Advanced Materials* **2012**, *24*, 5452-5456.
[15] a) X. Zhou, Y.-X. Yin, L.-J. Wan, Y.-G. Guo, *Chemical Communications* **2012**, *48*, 2198-2200; b) J. Chang, X. Huang, G. Zhou, S. Cui, P. B. Hallac, J. Jiang, P. T. Hurley, J. Chen, *Adv Mater* **2014**, *26*, 758-764.
[16] a) X. Xia, C. V. Di Leo, X. W. Gu, J. R. Greer, *ACS Energy Letters* **2016**, *1*, 492-499; b) Y. Liu, Z. Tai, T. Zhou, V. Sencadas, J. Zhang, L. Zhang, K. Konstantinov, Z. Guo, H. K. Liu, *Adv Mater* **2017**, *29*.

[17] a) M. K. Chan, C. Wolverton, J. P. Greeley, *J Am Chem Soc* **2012**, *134*, 14362-14374; b) H. Kim, C.-Y. Chou, J. G. Ekerdt, G. S. Hwang, *The Journal of Physical Chemistry C* **2011**, *115*, 2514-2521; c) V. L. Chevrier, J. R. Dahn, *Journal of the Electrochemical Society* **2009**, *156*, A454-A458; d) V. B. Shenoy, P. Johari, Y. Qi, *J Power Sources* **2010**, *195*, 6825-6830; e) K. Zhao, W. L. Wang, J. Gregoire, M. Pharr, Z. Suo, J. J. Vlassak, E. Kaxiras, *Nano Lett* **2011**, *11*, 2962-2967.
[18] X. H. Liu, L. Zhong, S. Huang, S. X. Mao, T. Zhu, J. Y. Huang, *ACS Nano* **2012**, *6*, 1522-1531.
[19] S.-C. Chao, Y.-C. Yen, Y.-F. Song, Y.-M. Chen, H.-C. Wu, N.-L. Wu, *Electrochemistry Communications* **2010**, *12*, 234-237.
[20] a) J. M. Paz-Garcia, O. O. Taiwo, E. Tudisco, D. P. Finegan, P. R. Shearing, D. J. L. Brett, S. A. Hall, *J Power Sources* **2016**, *320*, 196-203; b) J. Gonzalez, K. Sun, M. Huang, J. Lambros, S. Dillon, I. Chasiotis, *J Power Sources* **2014**, *269*, 334-343; c) P. Pietsch, D. Westhoff, J. Feinauer, J. Eller, F. Marone, M. Stampanoni, V. Schmidt, V. Wood, *Nat Commun* **2016**, *7*, 12909; d) S. Muller, P. Pietsch, B. E. Brandt, P. Baade, V. De Andrade, F. De Carlo, V. Wood, *Nat Commun* **2018**, *9*, 2340; e) O. O. Taiwo, J. M. Paz-García, S. A. Hall, T. M. M. Heenan, D. P. Finegan, R. Mokso, P. Villanueva-Pérez, A. Patera, D. J. L. Brett, P. R. Shearing, *J Power Sources* **2017**, *342*, 904-912; f) O. O. Taiwo, M. Loveridge, S. D. Beattie, D. P. Finegan, R. Bhagat, D. J. L. Brett, P. R. Shearing, *Electrochimica Acta* **2017**, *253*, 85-92; g) C. Zhao, T. Wada, V. De Andrade, D. Gürsoy, H. Kato, Y.-c. K. Chen-Wiegart, *Nano Energy* **2018**, *52*, 381-390.
[21] M. Ebner, F. Marone, M. Stampanoni, V. Wood, *Science* **2013**, *342*, 716-720.
[22] F. Sun, H. Markötter, K. Dong, I. Manke, A. Hilger, N. Kardjilov, J. Banhart, *Journal of Power Sources* **2016**, *321*, 174-184.
[23] a) D. S. Eastwood, P. M. Bayley, H. J. Chang, O. O. Taiwo, J. Vila-Comamala, D. J. Brett, C. Rau, P. J. Withers, P. R. Shearing, C. P. Grey, P. D. Lee, *Chem Commun (Camb)* **2015**, *51*, 266-268; b) J. Wang, Y. C. Chen-Wiegart, J. Wang, *Nat Commun* **2014**, *5*, 4570; c) F. Sun, R. Moroni, K. Dong, H. Markötter, D. Zhou, A. Hilger, L. Zielke, R. Zengerle, S. Thiele, J. Banhart, I. Manke, *ACS Energy Letters* **2017**, *2*, 94-104.
[24] H. Tavassol, E. M. Jones, N. R. Sottos, A. A. Gewirth, *Nat Mater* **2016**.
[25] M. J. Chon, V. A. Sethuraman, A. McCormick, V. Srinivasan, P. R. Guduru, *Phys Rev Lett* **2011**, *107*, 045503.
[26] J. Duay, K. W. Schroder, S. Murugesan, K. J. Stevenson, *ACS Appl Mater Interfaces* **2016**, *8*, 17642-17650.
[27] L. Y. Beaulieu, S. D. Beattie, T. D. Hatchard, J. R. Dahn, *Journal of The Electrochemical Society* **2003**, *150*, A419.
[28] F. Sun, H. Markotter, D. Zhou, S. S. Alrwashdeh, A. Hilger, N. Kardjilov, I. Manke, J. Banhart, *ChemSusChem* **2016**, *9*, 946-950.
[29] J. N. Weker, N. Liu, S. Misra, J. C. Andrews, Y. Cui, M. F. Toney, *Energy & Environmental Science* **2014**, *7*, 2771.
[30] W. Gorner, M. P. Hentschel, B. R. Muller, H. Riesemeier, M. Krumrey, G. Ulm, W. Diete, U. Klein, R. Frahm, *Nucl Instrum Meth A* **2001**, *467*, 703-706.

Supporting information

In situ and _Operando_ Tracking of Microstructure and Volume Evolution of Silicon Electrode using Synchrotron X-ray Imaging

Kang Dong,*[a][b] Henning Markötter,[b] Fu Sun,[b] André Hilger,[b] Nikolay Kardjilov,[b] John Banhart,[a][b] Ingo Manke[b]

[a] Institute of Materials Science and Technology, Technical University Berlin, Hardenbergstraße 36, 10623 Berlin, Germany

[b] Helmholtz-Zentrum Berlin für Materialien und Energie, Hahn-Meitner-Platz 1, 14109 Berlin, Germany

*Email: kang.dong@helmholtz-berlin.de

Movie S1. Dynamic microstructure evolution of silicon particles during the first lithiation (from 0 to 15.8 hours) and delithiation (from 15.8 to 27.4 hours).

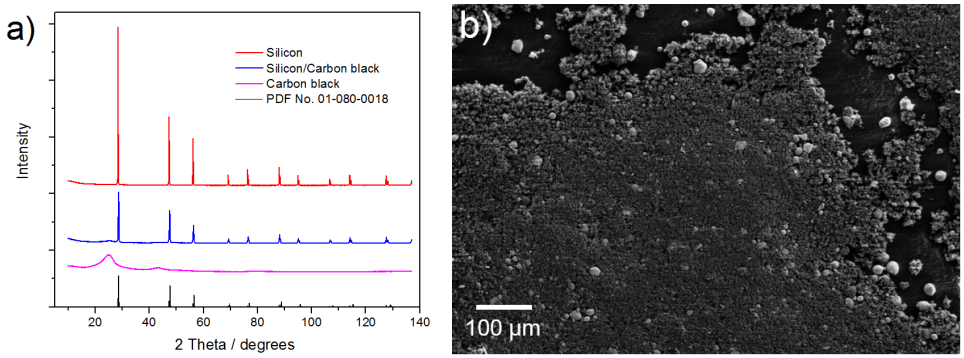

Figure S1. (a) XRD patterns of silicon, carbon black and Si/C composite. (b) SEM morphology of silicon and carbon black composite with a mass ratio of 1:1.

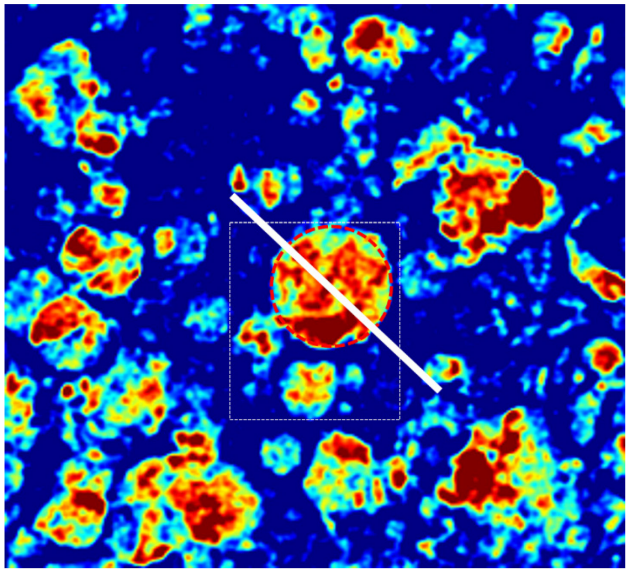

Figure S2. The rectangular region highlighted by a dashed white dash box is used for histograms of X-ray transmission during lithiation and delithiation in Figure 3; A red circle dash and a white dash across the particle schematically show the measurement process of particle diameter, which is regarded as the length of the white line segment cut off by red circle dash.

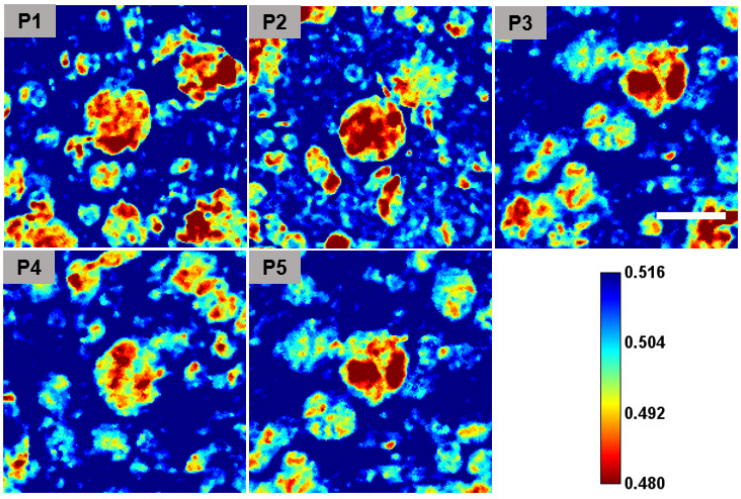

Figure S3. The pristine states of the five target particles that are used for comparison in Fig. 4. All the target particles are positioned at the center of each projection cutout. The length scale bar located in the image of P3 is 25 μm. Detailed description of particle diameter measurement can be found in experiment section.

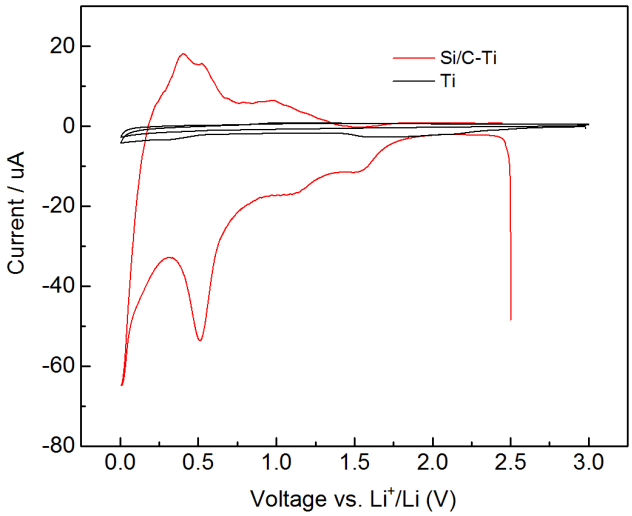

Figure S4. CV plots of Si/C-Ti and pure Ti (8 mm × 6 mm) electrode employing lithium as a counter electrode and 100 µl electrolyte at a scan rate of 0.1 mV/s. The negligible low current and unobservable redox peek between 0.005 and 3.0 V indicate a good electrochemical stability of Ti at this voltage window.

References

1. Gorner, W.; Hentschel, M. P.; Muller, B. R.; Riesemeier, H.; Krumrey, M.; Ulm, G.; Diete, W.; Klein, U.; Frahm, R., BAMline: the first hard X-ray beamline at BESSY II. *Nucl Instrum Meth A* **2001,** *467*, 703-706.

2.2 Lithium deposition at the Li/separator and Li/carbon matrix interregion

K. Dong, M. Osenberg, *et al*., Non-destructive Characterization of Lithium Deposition at the Li/Separator and Li/Carbon Matrix Interregion by Synchrotron X-ray Tomography. *Nano Energy,* **2019**, 62, 11-19. (DOI: 10.1016/j.nanoen.2019.05.022)

Non-destructive Characterization of Lithium Deposition at the Li/Separator and Li/Carbon Matrix Interregion by Synchrotron X-ray Tomography

Kang Dong [a, b,*,✉], Markus Osenberg [a,*], Fu Sun [c], Henning Markötter [a], Charl J. Jafta[d], André Hilger [b], Tobias Arlt [a], John Banhart [a, b], Ingo Manke [b]

[a] Institute of Materials Science and Technology, Technische Universität Berlin, Straße des 17. Juni, 10623 Berlin, Germany

[b] Institute of Applied Materials, Helmholtz-Zentrum Berlin für Materialien und Energie, Hahn-Meitner-Platz 1, 14109 Berlin, Germany

[c] Qingdao Institute of BioEnergy and Bioprocess Technology, Chinese Academy of Sciences, 189 Songling Road 266101 Qingdao, PR China

[d] Institute of Soft Matter and Functional Materials, Helmholtz-Zentrum Berlin für Materialien und Energie, Hahn-Meitner-Platz 1, 14109 Berlin, Germany

✉ Corresponding author

Email: kang.dong@helmholtz-berlin.de

Abstract

Inherently uncontrollable Li electrodeposition has significantly hindered the practical application of Li metal batteries largely due to a dendritic deposition which can initiate an internal short circuit and gives rise to severe safety issues. The understanding of the fundamental electrodeposition mechanism is, however, elusive and limited due to a lack of feasible in situ characterization techniques. Here synchrotron X-ray tomography was employed to noninvasively visualize Li deposition at the lithium/separator and lithium/carbon matrix interregion. A higher concentration of widely distributed deposition sites was observed under an increased current density. The 3D morphology and distribution of deposited Li within the widely used Celgard® 2325 polyolefin separator are, for the first time, visualized in situ, thus promoting the understanding of the short-circuiting process of Li metal batteries. In addition, we also visualized and quantified the spatial distribution of Li depositions inside a porous carbon host to unravel the deposition behavior that can hardly be probed by surface imaging

techniques. The Li electrodeposition behavior found here could help to promote the understanding and development of surface modifications related to Li anodes, separators as well as novel 3D geometry electrode designs for accommodation of Li depositions and alleviation of volumetric changes.

Keywords: Lithium deposition; dendrites; lithium metal batteries; energy storage; in situ X-ray tomography

1. Introduction

After almost three decades of commercialization and development, Li-ion batteries are the dominant power source of portable electronic devices and electric vehicles. However, their practical energy density is limited by the graphite anode and therefore available systems do not meet the ever-increasing market demand for lighter and safer batteries with longer lifetime and lower costs.[1, 2] Metallic lithium (Li) as an anode material for rechargeable lithium batteries (*e.g.* Li-S and Li-air systems) is gaining increasing attention nowadays as it has the highest theoretical capacity (3860 $mAh \cdot g^{-1}$), lowest anode potential (-3.04 V vs. the standard hydrogen electrode) and lowest mass density (0.534 $g \cdot cm^{-3}$) of all known candidates.[3, 4] With ten times higher theoretical capacity than commercial graphite anodes (372 $mAh \cdot g^{-1}$), batteries based on lithium anodes and transition metal oxide cathodes could markedly boost the available energy density roughly from 250 $Wh \cdot kg^{-1}$ to 440 $Wh \cdot kg^{-1}$.[3] Unfortunately, lithium anode is still plagued by the uncontrollable growth of hazardous Li microstructures (e.g. dendrites and fibres) and a low coulombic efficiency derived from unstable solid electrolyte interphase (SEI) after its early studies in the 1970s.[5] These two issues together lead to large volumetric changes and a short lifespan. Furthermore, the dendritic and fibre-like deposition of lithium can penetrate the separator and induce an internal short circuit with a risk of an outbreak of fire or even an explosion.

In order to address these problems, numerous advanced materials and novel architectural designs have been proposed including 3D host media for Li deposition[6-12], polymer or solid electrolytes[13] and additives[14-17], as well as surface modifications of the Li anode[18-21] or the separator[22, 23]. Much progress has been made through these approaches in suppressing Li dendrite formation, improving coulombic efficiency (CE) and stabilizing the SEI. Meanwhile, with the development of advanced probe techniques, the understanding of the lithium deposition mechanism has been significantly promoted in the last decade. For instance, optical microscopy [24-27], electron microscopy [28-30] (*e.g.* SEM and TEM) or nuclear magnetic resonance imaging [31, 32] (NMR or MRI) have recently been employed more frequently for the characterization of the electrode's morphological, structural, or volumetric change and

the lithium plating and stripping process. Nevertheless, these techniques provide insufficient resolution or are limited to a harsh sample environment such as high vacuum and in situ characterization lacks feasibility and operability to some extent. Therefore, techniques that are able to probe battery systems without the need to disassemble a battery and exposing components to environments that could alter their chemical characteristics or appearance are highly useful for the battery community. By using such in situ or in operando techniques it is possible to probe the electrode interface and study the underlying mechanisms of lithium deposition and stripping without disturbing the system.

Recently, operando Neutron Depth Profiling (NDP) was employed to study the distribution of the Li-ions as a function of depth perpendicular to the lithium anode and revealed that the lithium stripping process was more homogenous than the plating process.[33] Synchrotron or lab-based X-ray tomography has also been demonstrated a promising technique to observe the morphological and structural evolution of battery materials under in situ/operando conditions.[34-39] For instance, Harry *et al.* [40] detected the morphology of Li dendrites of cycled lithium polymer batteries and emphasized the important role of subsurface structures in the formation of dendrites. With the same approach, the morphological evolution of a lithium anode was visualized in three dimensions[41] and the mechanism of internal short circuit induced by Li plating and stripping was also investigated.[42, 43]

Herein, in situ synchrotron X-ray tomography was employed to visualize Li deposition at the Li/separator interregion, including the deposition along the Li/separator interface, inside the triple-layered separator and within the porous carbon matrix host. The deposition distributed within the widely used Celgard® separator, to our knowledge, has been characterized and analysed for the first time in 3D. It has been also found that with increasing current density, Li deposition varies in morphologies and distributions at the Li/separator interface as well as within the separator. In addition, a porous carbon fiber matrix was selected for analysing and quantifying Li deposition within this matrix in 3D and unravelling the deposition behavior, which can hardly be probed by surface imaging techniques alone.

2. Experiment

2.1 Materials

Metallic lithium and Celgard® 2325 separator were purchased from MTI Corp. USA. The electrolyte of 1 M $LiPF_6$ with a mixture of ethylene carbonate (EC) and ethyl methyl carbonate (EMC) (1:1, v/v) was received from Sigma-Aldrich. Carbon paper was purchased from Kynol Europa GmbH. The housing for the battery made of polyamide-imide (Torlon) was received from Drake Plastics Europe.

2.2 Battery assembly and characterization

To build the tailor-made cell for X-ray tomography measurements, Celgard® 2325 separator (diameter 3 mm) was sandwiched by two discs of pre-cut metallic lithium (diameter 2.5 mm). Carbon fiber paper in diameter of 2 mm was employed for the symmetric Li-Carbon/Separator/Carbon-Li cell. The amount of electrolyte used for Li/Li conventional cells and cells with carbon deposition host was 20 µl and 70 µl, respectively.

Galvanostatic cycling or charging of the Li/Separator/Li cells and Li-Carbon/Separator/Carbon-Li cell was carried out using Bio-logic MPG2 battery tester and Neware BTS4000 battery cycler, respectively. Before continuous charging, all the cells were subjected to cell activation by 4 cycles of charge and discharge at a low current density. Applied current was calculated based on the area of Li disks (2 mm in diameter). Except the Li-Carbon/Separator/Carbon-Li cell which did not short-circuit after 21 hours of continuous charging, all the Li/Separator/Li cells subjected to constant current cycling short-circuited (defined as a dramatic voltage drop to below 20 mV) during the continuous charging.

Synchrotron X-ray imaging was conducted at the BAMline at the BESSY II electron storage ring of the Helmholtz-Zentrum Berlin, Germany.[44] The synchrotron beam was monochromatized using a double multilayer monochromator that provided an energy resolution of about $\Delta E/E = 1.5\%$ at an energy of 17 keV and 20 keV for Li/Li cells and cells with a carbon deposition host, respectively. These monochromatic synchrotron X-rays were directed onto the sample during a 180° sample rotation. The detector system behind the sample detecting the transmitted and refracted X-rays consisted of a 60-µm thick $CdWO_4$ scintillator, a set of microscope optics and a PCO4000 camera with a 4008 × 2672 pixel CCD sensor. A (1.7 × 1.2) mm^2 field of view was captured with a pixel size of 0.438 µm. All tomography datasets contain 2200 projections and 230 flatfields with an exposure time of 2 s for each projection/flatfield.

The morphology of the carbon paper matrix was investigated using a Zeiss LEO Gemini 1530 scanning electron microscope (SEM). Nitrogen sorption isotherms were obtained from a Quantachrome Autosorb-1MP at liquid nitrogen temperature after the sample was outgassed at 150 °C for 24 h. The data analysis was performed by the Quantachrome software where the specific surface area was calculated by means of the Brunauer–Emmett–Teller (BET) equation and the pore size distribution by a Density Functional Theory (DFT) method. Galvanostatic cycling of the cells was conducted using Bio-logic MPG2 or Neware BTS4000 battery cycler.

2.3 Data processing

The obtained raw image datasets were normalized using darkfields and the best fitting flatfields. These flatfields where found for each projection individually via a correlation based algorithm (written in IDL 8.2). After normalization, drifts and movements

corrections, the datasets were then reconstructed via filtered back projection two times. First reconstruction used a Paganin based filter[45] for pseudo phase retrieval and second with a Hanning filter, both using IDL 8.2 in combination with the "gridrec"[46] library. For segmentation machine learning was applied using ImageJ/Weka[47] utilizing the signals of both reconstructions. The separator phase was segmentated manually using ImageJ. The segmentations were then used as masks on the Hanning filtered reconstructions. Each masked phase was then visualized using VGSTUDIO MAX 3.1. For the 2D overview of the deposition within the separator in Fig. 2 and Fig. 3 the reconstructed volume was flattened along the axis perpendicular to the separator. To flatten the volume in the separator layers the data sets were morphed perpendicular to the separator using the "non-planar view" functionality of VGSTUDIO MAX 3.1. This was done for visualization only (as shown in Fig. 2 and Fig. 3), while the volume calculations were performed without volume morphing.

3. Results and discussion

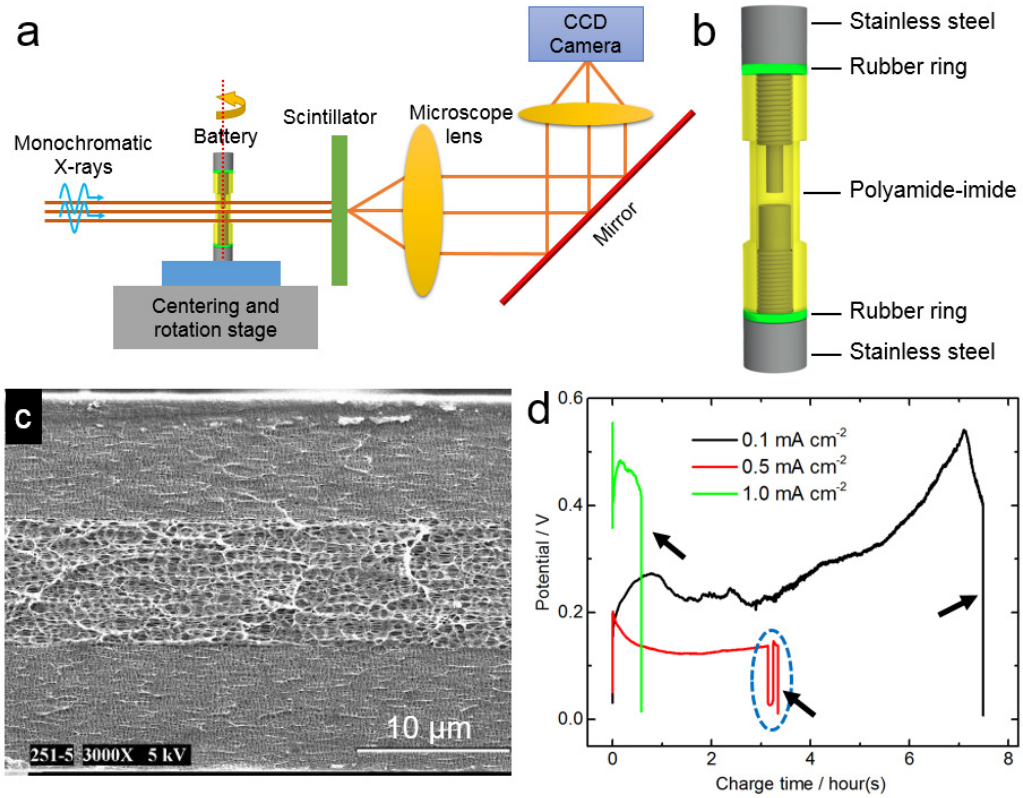

Figure 1. Schematic illustrations of a) the synchrotron X-ray imaging setup and b) the custom-built cell for tomography measurements. c) SEM cross-section view of the Celgard® 2325 separator. d) The voltage profiles of three symmetric Li/Li cells charging at three different current densities until short circuit when the voltage dropped to below 20 mV. Panel c) has been adapted with permission from reference 49 with permission by the American Chemical Society.

Li deposition in a conventional Li|Separator|Li cell

A Swagelok-type cell was custom-built for in situ X-ray tomography (Fig. 1a and 1b). This design has already demonstrated excellent compatibility with synchrotron X-ray tomography setups and can provide good sealing, stable electrochemistry and mechanical stability for image data acquisition.[42, 48] We opted to study symmetric Li/Li cells to illustrate the lithium deposition behavior at the Li/separator interregion and to unravel the mechanisms of battery failure induced by non-uniform lithium deposition. A 25-µm thick commercial Celgard® 2325 separator comprising a PP/PE/PP trilayer as depicted in Fig. 1c was employed in the cells investigated in this work. This trilayer separator offers the advantage of a shut-down feature, where the middle layer has a lower phase transition temperature (160/135/160 ºC) which will fill the pores and stop ion transport when the temperature increases.[49] Three pristine cells were first subjected to a cell activation process (Fig. S1) consisting of 4 cycles running at a low current density (0.1 $mA \cdot cm^{-2}$) to get closer to a practical scenario. Subsequently, these cells were charged at three different current densities (0.1, 0.5, 1.0 mA cm^{-2}, respectively, hereafter named cell No. 1, No. 2 and No. 3) until an internal short circuit occurred (defined here as a sudden sharp voltage drop to below 20 mV, as indicated by black arrows in Fig. 1d). As shown in Fig. 1d, the voltage response of the cell differs for different current densities from the initial voltage increase to cell failure. After cycling, the cells were respectively mounted on the imaging setup and measured by synchrotron X-ray tomography without cell disassembly. Due to the high transmission (> 85.2 %) of the cell active components which contain low atomic elements (Li, C, H, O, P, F) at the applied X-ray energies (17 and 20 keV), interactions between X-rays and active cell components will be largely decreased. Therefore potential beam damage can be effectively suppressed.

Two representative cross-sectional slices from cell No. 1 after cell failure are presented in Fig. 2a and 2b. Firstly, a hill-like protrusion can be observed in Fig. 2a (between yellow dashed lines) and is shown in 3D in Fig. 2c. This protrusion could be attribute to the accumulation of deposition at the electrochemically hot spots, where the relative high local current density area and preferred deposition sites locate. A similar protrusion has been observed in our previous work and it has been analysed that the protrusion consists mainly of electrochemically generated lithium micro-structures[42]. Here, we focus on the comparison of the different deposition behaviors and distributions at the Li/separator interregion under different current densities. Secondly, apart from the protrusion at the interface between Li and separator, Li deposition was also observed within the trilayer separator between two PP (polypropylene) layers, which is evident in Fig.2b and is further visualized in Fig. 2c and 2d using red and blue color representing two different deposition morphologies. From its corresponding distribution map as shown in Fig. 2d, two types of deposited Li morphologies within the separator are visible, namely flake- and island-like depositions (shown in red and blue, respectively). The deposited lithium within the separator accounts for 20.8% of

the whole probe area. In addition, the location of the protrusion displayed in Fig. 2a and 2c is also shown in Fig. 2d and highlighted by the green dashed line.

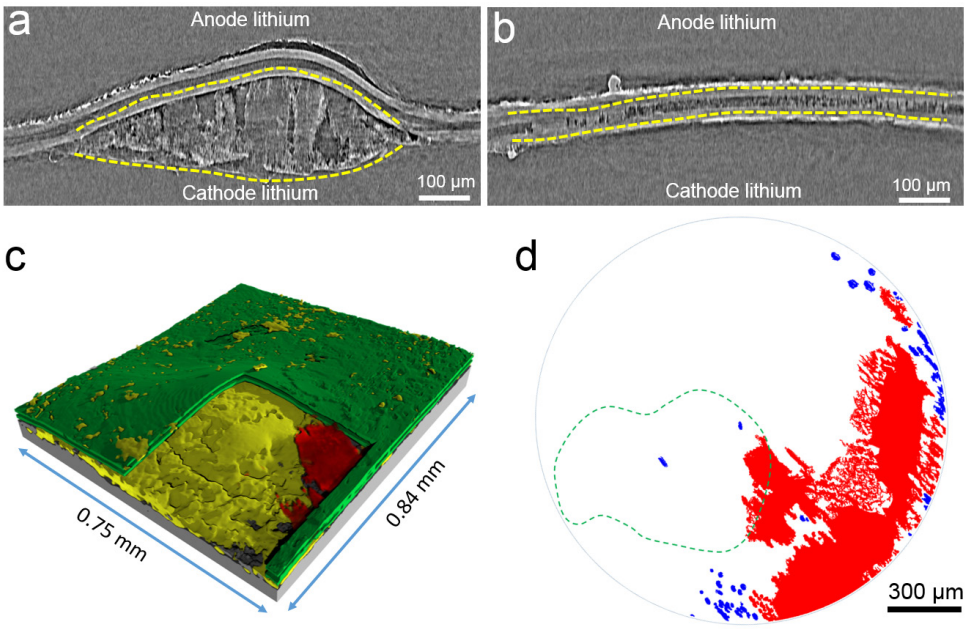

Figure 2. **Internal morphological changes of cell No. 1 deposited at 0.1 mA cm^{-2}**. a)-b) Cross-sectional view of two different lithium deposition morphologies in short-circuited Li/Li cell No. 1 after continuous charging at 0.1 mA cm^{-2} as obtained by X-ray tomography. c) 3D visualization of the two different morphological deposition, namely hill-like deposition (yellow), flake-like deposition (red), that is shown in a) and b) as well as the separator (green) and cathode Li (dark grey). d) Morphology and distribution of deposited Li within the trilayer separator labeled in red (flake-like) and blue (island-like). The broken green line indicates the location of the hilly deposition beneath the separator shown in a) and c).

When 0.5 mA·cm^{-2} was used during continuous charging, Li deposition at the Li/separator interregion differed in morphology and distribution. Firstly, the deposition at the Li bulk interface was found to exhibit a clastic morphology and to be distributed more widely compared to the protrusion-like structure observed at 0.1 mA·cm^{-2}, as indicated by the blue dashed line in Fig. 3a and the distribution map in Fig. 3c. This indicates that the active sites for deposition tended to be more at 0.5 mA·cm^{-2}, which agrees well with previous reports[28]. Comparison of the cross-sectional views of cells between the pristine state and after deposition at three different current densities also demonstrates the increasing of active sites, as shown in Fig. S2. Secondly, within the separator, branch-like deposition mainly formed along the PE (polyethylene) layer as indicated by the red dashed line in Fig. 3a and is shown in Fig. 3d. These depositions are electrochemically generated during Li plating and could penetrate the separator more easily than the Li microstructure obtained at 0.1 mA·cm^{-2}, posing greater threat to battery safety. Moreover, it can clearly be observed that at the surface of the stripping side (i.e. anode lithium), Li-based compounds also exist as the lowest yellow layer at anode side shown in Fig. 3a. This layer of Li compounds at anode side was also found

for the cell that was charged at 1.0 mA·cm^{-2}. This may be caused by side reactions between the electrolyte and the continuously exposed fresh Li during the ongoing stripping process as well as the remaining Li deposition from the pre-cycling process. These Li-based compounds that evolved from side reactions will be explained in more detail in Fig. 4.

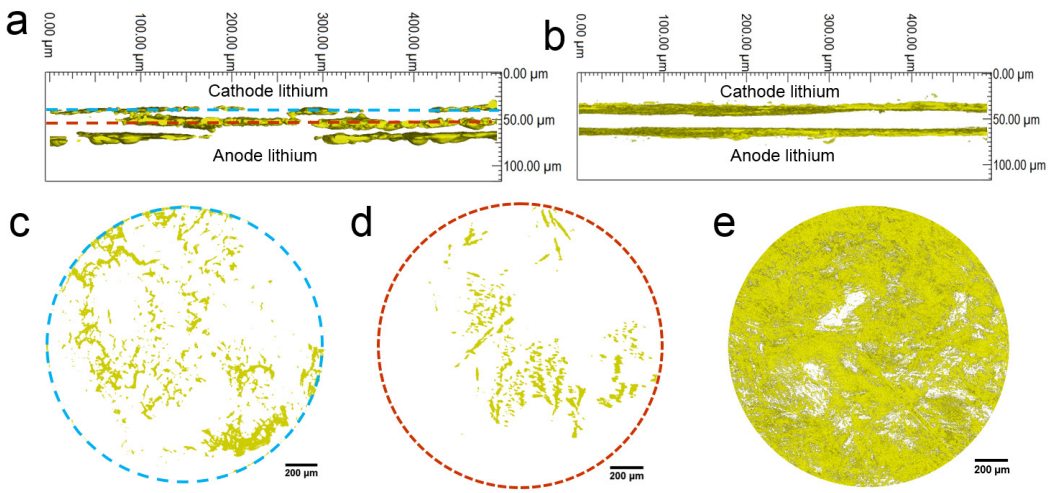

Figure 3. Internal morphological changes of cell No. 2 and No. 3 charged at 0.5 mA·cm^{-2} and 1.0 mA·cm^{-2}, respectively. Cross-sectional view of the short-circuited cell a) No. 2 and b) No. 3. In fig. 3a, the upper and lower yellow layers are Li composites at the Li interface while the middle one shows depositions within the separator. Through-plane slice of Li deposition c) at cathode Li/separator interface and d) within the separator, locations of which are highlighted with a dashed blue and red line in a). e) Top view of the data set illustrating the morphology and distribution of depositions at the cathode Li/separator interface within cell No. 3 in fig. 2b.

With progressing Li deposition at the cathode Li/separator (PP/PE/PP) interface, the outer PP layer might be penetrated at the cathode lithium by the electrochemically generated Li dendrite. Subsequently, the penetration arrives at the middle PE layer which has a higher porosity than PP layer. This PE layer could be a preferential deposition area instead of the cathode interface due to short Li-ion migration paths and easier access to the electrolyte in the porous PE layer. The higher porosity of the PE layer leads to low mechanical strength which enables the deposition within the PE layer. Additionally, a relatively lower tensile strength of Celgard® 2325 in the lateral direction deriving from the method of manufacture (stretching)[49], promotes the lateral spread within the separator rather than a vertical spread. This currently observed Li deposition confined between two PP layers share similarities to the recently observed findings that Li plating proceeds preferentially along 2D Lipon-Lipon interface.[50] These results collectively demonstrate the unique Li deposition behavior that has been never revealed before. On the other hand, it seems that the build-in shutdown function of the PP/PE/PP trilayer separator was activated during Li deposition as the two voltage-drops indicates (highlighted by the blue dash ellipse in Fig. 1d). With a lower

phase transition temperature of 135 ºC, the PE layer melts first and fills the pores to prevent ion transport at the short-circuit area[49, 51], which leads to a voltage increase. After self-repair of the separator, the cell was still kept charging until the second voltage drop occurred around 12 minutes later as the first pronounced voltage drop did not trigger the preset cutoff voltage (20 mV).

Table 1. Comparison of morphology and distribution of Li deposition at Li/separator interregion.

Current density	**at Li/separator interface**		**within separator**	
	Morphology	Distribution	Morphology	Distribution
Low current	hilly	few	flake/island-like	agminated
Medium current	clastic	widespread	branch-like	scattered
High current	lamellar	tiled	not observed [a)]	rare

a) Lithium deposition was not observed in the selected region, which could be largely due to the needle-like deposition that is below the spatial resolution.

Compared to the hilly and clastic Li deposition at 0.1 and 0.5 mA·cm^{-2} a high current density of 1.0 mA·cm^{-2} led to a tiled deposition at the Li/separator interface, as shown in Fig. 3b and Fig. S2. This widely distributed deposition indicates the increase of active deposition sites at the Li interface when a higher current was utilized. However, deposition within the trilayer separator was not observed at the high current density (1.0 mA·cm^{-2}). A relative high current density is likely to induce more detrimental deposition types such as needle-like dendrite, which has a diameter that is typically around or less than 500 nm.[24, 52] Based on the morphology and the distribution of the deposition when increasing the current from 0.1 to 0.5 mA·cm^{-2}, we assume that this missing deposition within the separator at 1.0 mA·cm^{-2} could be largely due to a deposition morphology type (*e.g.* needle-like) that can be hardly observed with a detector resolution of 0.438 μm.

The morphology and distribution of Li deposition at the Li/separator interregion are summarized in Table 1. With increasing current the active deposition sites at the Li surface tend to be more frequent and widely distributed. This leads to a decreasing tension imposed on the separator at the electrode level. While within the separator, the morphology of the Li deposition evolved from flake/island-like to branch-like until possible needle- or filament-like deposition. This indicates an increased risk of separator penetration and thus short-circuiting, as can be clearly observed in Fig. 1d that a higher current density leads to a faster short-circuit event. In addition, it can be calculated based on Fig. 1d that when cell No. 1, 2 and 3 got short-circuit they did not have the same cell failure charging capacity which are 0.75, 1.70, 0.58 mAh·cm^{-2}, respectively.

Based on the in situ measurements of Li depositions along the Li surface and within the separator, the knowledge of cell short-circuit can be extended from understanding a transient incident to understanding a propagation process. Furthermore, as this

commercial trilayer separator can be regarded as a single PE layer artificially modified by being sandwiched between two PP layers, the Li deposition observed between two PP layers could also possibly be found in a bilayer or surface-modified multilayer polymer separator that has anisotropic mechanical properties. The same applies to ceramic[53] and glass fiber[54] separators that feature high porosities, where depositions preferentially occur. This is the first time that the 3D morphology and distribution of Li deposition within a commercial Celgard® polyolefin separator are visualized. The valuable insights presented here could guide the design and development of surface modification on either the separator or metallic anode in order to suppress rapid short-circuit induced by detrimental Li or Na deposition.

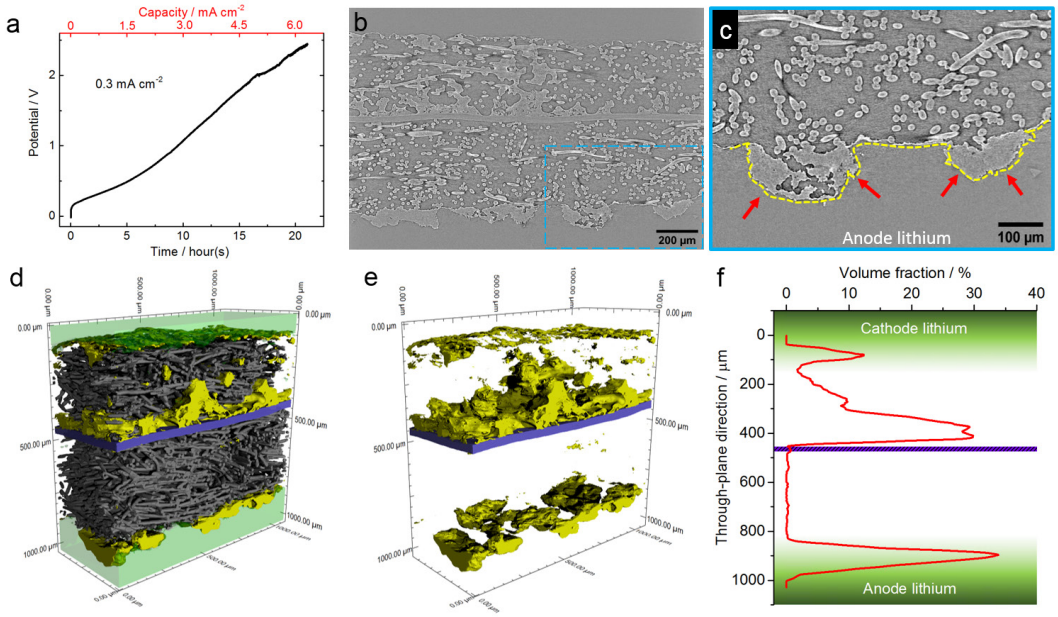

Figure 4. Porous carbon fiber matrix as deposition host. a) The voltage profile of a symmetric Li-Carbon/Carbon-Li cell during high capacity Li deposition at 0.3 mA·cm^{-2}. b) Cross-sectional view of reconstructed raw data after 21 h charging, illustrating two carbon fiber matrices sandwiched between a Li cathode (top) and a Li anode (bottom) with Li depositions at the Li surface and within the carbon matrix. c) Enlarged figure of the region highlighted by blue rectangle in b). d) 3D visualization of a classified subvolume after the high capacity deposition of 6.3 mAh·cm^{-2}. e) As in d) but without showing the Li bulks and the carbon fibers. f) Volume fraction of Li deposition in e) along through-plane direction from cathode Li to anode Li.

Li deposition when utilizing porous carbon host

According to Chazalviel's model, the onset time of uneven deposition is inversely proportional to the applied current density (i.e., $\tau \propto J^{-2}$).[55] On the basis of this theory, various high-surface-area 3D porous media such as an artificial protection layer[10], a conductive[11] or non-conductive porous matrix[7-9] or a 3D substrate[6] have been adopted to lower J and at the same time to accommodate the deposition of Li. Although significant improvement has been shown via using these 3D Li hosts, the underlying Li

deposition mechanism such as the deposition behavior and 3D distribution remain untackled due to the technical challenges of developing non-destructive characterization tools. However, future design of more effective and stable 3D Li host to further redistribute lithium-ion flux, accommodate tremendous volume change and regulate uncontrollable Li deposition asks for fundamental understanding of Li deposition mechanism within 3D hosts. Herein, a porous carbon fiber matrix with a specific surface area of 1265 $m^2 g^{-1}$ (Fig. S3-S4) was employed to investigate the underlying Li deposition mechanism.

A Li-Carbon/Separator/Carbon-Li symmetrical cell was assembled and its pristine state is shown in Fig. S5. After 21 h of on-going charging at 0.3 $mA \cdot cm^{-2}$, corresponding to a deposition capacity of 6.3 $mAh \cdot cm^{-2}$ as shown in Fig. 4a, no internal short circuit occurred. The cell was then characterized by non-destructive X-ray tomography without cell disassembly. Fig. 4b shows a cross-sectional view of the cell and Fig. 4c displays the enlargement of the selected region. Compared to the pristine state (Fig. S5) of the cell, several evident features can be observed after Li deposition. Firstly, the anode Li shows clearly non-uniform dissolved Li pits, as pointed by red arrows in Fig. 4c. It has been generally acknowledged that Li will dissolve during Li stripping process but little is known towards whether the Li dissolve uniformly or non-uniformly. The findings observed in Fig. 4c provides unambiguous evidence that Li dissolve non-uniformly during stripping process. Actually, the current findings agree well with a recent study by Li and co-workers[56], who have predicted by density functional theory (DFT) and tight-binding (DFTB) calculations that Li would be stripped non-uniformly and large voids would form on the Li-metal surface. Secondly, a pronounced passivation layer can be found on anode Li surface as shown in Fig. 4c along the yellow dashed line. Compared to the pristine state (Fig. S5) with hardly visible surface films, a passivation thin layer that covers anode Li can clearly be observed after cycling. Its thickness is non-uniform and the layer is inferred to be the solid electrolyte interface (SEI) layer. The thickness increase of this layer was largely due to repetitive layer breakage and repair during cycling. In addition, as the layer covering on the Li bulk surface was relatively stable, the Li in the pits or along the yellow dashed line beneath the pits would be the preferred further stripping area as the covering passivation SEI layer on these areas were newly generated and could be mechanically unstable. Thirdly, significant electrolyte consumption after electrochemical deposition can be noticed after compared with the pristine state, as shown Fig. S5. The electrolyte, as the Li-ion carrier for Li stripping/plating, is generally supposed to be uniformly distributed within the matrix even with the impact of an external electric field. However, compared with the highly electrolyte-wetted carbon in the pristine state (Fig. S5), the electrolyte can hardly be seen within the carbon anode matrix after electrochemical deposition. Therefore, we speculate that a large amount of the electrolyte has been consumed. This can also explain the ever increasing voltage (Fig. 4a) that could largely derive from a concentration polarization due to severe electrolyte consumption.

Further data segmentation and analysis clearly reveals an inhomogeneous distribution of Li microstructure deposition within the Li-Carbon/Separator/Carbon-Li cell, as shown in Fig. 4d-4f. On the one hand, massive Li microstructures can be observed in the carbon network at the cathode side (yellow deposits above the purple separator shown in Fig. 4d and 4e). These Li microstructures mainly consist of the electrochemically generated Li together with the Li-based by-products formed between the freshly deposited Li and the electrolyte. The majority of this composite is located adjacent or at least close to the separator where Li-ions tend to get electrons directly through the carbon matrix once they have migrated up through the separator. The reason is that deposition of Li-ions near the separator requires less energy without their migration through the whole carbon matrix for the electrochemical reduction at the lithium bulk. In addition, the Li bulk is usually protected by an electronic insulating SEI layer. Therefore, active deposition sites are more likely to exist on carbon fibers or previously deposited lithium within the matrix as electrons can be easily accessed there. On the other hand, another comparable large portion of Li-based deposition exists adhering to the anode Li (Fig. 4c and 4d, yellow deposits below the purple separator). The Li stripping process during the 21 h period (Fig. 4a) continuously exposed fresh Li to the electrolyte, leading to ongoing complex side reactions[57] between the electrolyte and fresh Li, thus generating scattered pits which were simultaneously filled with Li-based side-products. The yielded side-products, such as Li alkyl carbonates ($ROCO_2Li$, ROLi, *etc.*) and Li salts (*e.g.* LiOH, Li_xPF_y), tended to deposit at the stripping sites as the yellow dashed line shown in Fig. 4c. They progressively propagated in depth as well as in width. This process has been previously proposed by Aurbach[58] *et al.* deduced from an in situ atomic force microscopy study, but here, it is further demonstrated and directly visualized.

In contrast to the pronounced Li deposition within the aforementioned separators, Li deposition can hardly be observed in the separator sandwiched by the carbon fiber matrix. In addition, the symmetrical cell based on the carbon matrix did not end with a short circuit even after a high deposition capacity of 6.3 $mAh \cdot cm^{-2}$. This enhanced durability compared with the cells without a deposition host indicates that the porous conductive matrix can effectively act as a superior host for lithium deposition, suppressing a tremendous volume expansion and leading to a prolonged battery lifespan.

Nevertheless, several questions remain to be answered regarding to Li deposition when employing deposition hosts. Firstly, the preferential Li deposition location within 3D host materials has to be further revealed. By employing electron conductive 3D host materials, such as copper[6] and the currently employed carbon matrix, it has been shown that the Li deposition is likely to occur preferentially near the separator and propageate towards the Li bulk/current collector. For electron insulator hosts, such as α-Si_3N_4[8] or polymer[9], preferential deposition sites appear to be near the Li bulk/current collector (i.e. electron donator) and then grow towards the separator. However, a uniform Li deposition within the vapor-grown carbon nanofiber without

any preferential deposition location has been recently reported by Jo and co-workers[59]. These findings suggest that fundamental deposition mechanisms within 3D host materials still demand more elaborate characterizations and insightful understandings. Secondly, the effect of a 3D host on the Li deposition behavior has to be further studied. The current research clearly exemplifies a different Li deposition behavior when using 3D Li host[60]. Previous report has also demonstrated that different Li deposition behavior can be observed when tuning the pore spacing and pillar diameter of the 3D Cu current collector. It is thus concluded that the effect of the pore sizes, tortuosity, conductivity and thickness of the 3D host matrix has to be further resolved. Thirdly, novel electrolytes of higher chemical/electrochemical stability have to be developed and their interaction with Li has to be investigated. Although hazardous lithium depositions and detrimental volume change could be well addressed by utilizing deposition hosts, the non-negligible Li-based composites generated from side reactions accompanied with remarkable electrolyte depletion emphasize the significance and necessity of exploring novel liquid electrolytes, polymer or solid electrolytes. Although recently batteries using novel solid electrolytes have displayed enhanced electrochemical performance,[61, 62] fundamental knowledge towards the electrode/electrolyte interface and/or interregion remains to be promoted for further performance improvement. Given the non-destructive and non-invasive characteristics and the 3D visualization ability, synchrotron X-ray tomography especially conducted in situ or in operando is capable to play a valuable role in these electrode/electrolyte interface and/or interregion investigations.

4. Conclusion

In summary, by using in situ synchrotron X-ray tomography we present and elucidate different Li deposition characteristics along the Li/separator interface, inside a trilayer separator and a porous carbon matrix. With increased current densities the active deposition sites at the Li surface were found to be quantitatively more and widely distributed. With this non-destructive and non-invasive imaging technique, the 3D morphology and distribution of Li deposition within a polyolefin separator are visualized in situ. Moreover, the visualization and quantification of the spatial Li distribution within carbon deposition host are presented. A different deposition behavior in the presence of a deposition host is found and suspected to depend on the conductivity of the host. The deposition behavior found in the Li/separator interregion could help to promote the understanding and development of surface modifications related to Li anodes, separators as well as novel 3D geometry electrode designs for the accommodation of Li depositions and alleviation of volumetric changes.

Acknowledgments

This work was sponsored by the Helmholtz Association, the China Scholarship Council (CSC) and was partially funded by the German Research Foundation, DFG (Project No. MA 5039/4-1). We would gratefully acknowledge Helmholtz-Zentrum Berlin for the beam time allocation at BAMline and Dr. Heinrich Riesemeier and Ralf Britzke for technical support. The authors would also like to thank Dr. Anna Manzoni for SEM measurement and John Schneider for tomography cell fabrication.

Author Contributions

* K. Dong and M. Osenberg contributed equally to this work.

Present Address

C. J. Jafta: Oak Ridge National Laboratory, Oak Ridge, TN, United States.

Notes

The authors declare no conflicts.

References

[1] M. Armand, J.-M. Tarascon, Building better batteries. *Nature*, **2008**, 451, 652.
[2] R. Van Noorden, The rechargeable revolution: A better battery. *Nature*, **2014**, 507, 26.
[3] D. Lin, Y. Liu, Y. Cui, Reviving the lithium metal anode for high-energy batteries. *Nature Nanotechnology*, **2017**, 12, 194.
[4] X. B. Cheng, R. Zhang, C. Z. Zhao, Q. Zhang, Toward Safe Lithium Metal Anode in Rechargeable Batteries: A Review. *Chem Rev*, **2017**, 117, 10403.
[5] W. Xu, J. Wang, F. Ding, X. Chen, E. Nasybulin, Y. Zhang, J.-G. Zhang, Lithium metal anodes for rechargeable batteries. *Energy Environ. Sci.*, **2014**, 7, 513.
[6] S. H. Wang, Y. X. Yin, T. T. Zuo, W. Dong, J. Y. Li, J. L. Shi, C. H. Zhang, N. W. Li, C. J. Li, Y. G. Guo, Stable Li Metal Anodes via Regulating Lithium Plating/Stripping in Vertically Aligned Microchannels. *Adv Mater*, **2017**, 29.
[7] Y. Liu, D. Lin, Z. Liang, J. Zhao, K. Yan, Y. Cui, Lithium-coated polymeric matrix as a minimum volume-change and dendrite-free lithium metal anode. *Nat Commun*, **2016**, 7, 10992.
[8] N. Li, W. Wei, K. Xie, J. Tan, L. Zhang, X. Luo, K. Yuan, Q. Song, H. Li, C. Shen *et al.*, Suppressing Dendritic Lithium Formation Using Porous Media in Lithium Metal-Based Batteries. *Nano Lett*, **2018**, 18, 2067.
[9] G. X. Li, Z. Liu, Q. Q. Huang, Y. Gao, M. Regula, D. W. Wang, L. Q. Chen, D. H. Wang, Stable metal battery anodes enabled by polyethylenimine sponge hosts by way of electrokinetic effects. *Nature Energy*, **2018**, 3, 1076.
[10] G. Zheng, S. W. Lee, Z. Liang, H. W. Lee, K. Yan, H. Yao, H. Wang, W. Li, S. Chu, Y. Cui, Interconnected hollow carbon nanospheres for stable lithium metal anodes. *Nat Nanotechnol*, **2014**, 9, 618.
[11] Z. Liang, D. Lin, J. Zhao, Z. Lu, Y. Liu, C. Liu, Y. Lu, H. Wang, K. Yan, X. Tao *et al.*, Composite lithium metal anode by melt infusion of lithium into a 3D conducting scaffold with lithiophilic coating. *Proc Natl Acad Sci U S A*, **2016**, 113, 2862.
[12] Y. Zhang, W. Luo, C. Wang, Y. Li, C. Chen, J. Song, J. Dai, E. M. Hitz, S. Xu, C. Yang *et al.*, High-capacity, low-tortuosity, and channel-guided lithium metal anode. *Proceedings of the National Academy of Sciences*, **2017**, 114, 3584.

[13] C. Z. Zhao, X. Q. Zhang, X. B. Cheng, R. Zhang, R. Xu, P. Y. Chen, H. J. Peng, J. Q. Huang, Q. Zhang, An anion-immobilized composite electrolyte for dendrite-free lithium metal anodes. *Proc Natl Acad Sci U S A*, **2017**, 114, 11069.
[14] F. Ding, W. Xu, G. L. Graff, J. Zhang, M. L. Sushko, X. Chen, Y. Shao, M. H. Engelhard, Z. Nie, J. Xiao *et al.*, Dendrite-free lithium deposition via self-healing electrostatic shield mechanism. *J Am Chem Soc*, **2013**, 135, 4450.
[15] X.-Q. Zhang, X.-B. Cheng, X. Chen, C. Yan, Q. Zhang, Fluoroethylene Carbonate Additives to Render Uniform Li Deposits in Lithium Metal Batteries. *Advanced Functional Materials*, **2017**, 27, 1605989.
[16] Y. Liu, D. Lin, Y. Li, G. Chen, A. Pei, O. Nix, Y. Li, Y. Cui, Solubility-mediated sustained release enabling nitrate additive in carbonate electrolytes for stable lithium metal anode. *Nat Commun*, **2018**, 9, 3656.
[17] X. B. Cheng, M. Q. Zhao, C. Chen, A. Pentecost, K. Maleski, T. Mathis, X. Q. Zhang, Q. Zhang, J. Jiang, Y. Gogotsi, Nanodiamonds suppress the growth of lithium dendrites. *Nat Commun*, **2017**, 8, 336.
[18] J. Becking, A. Grobmeyer, M. Kolek, U. Rodehorst, S. Schulze, M. Winter, P. Bieker, M. C. Stan, Lithium-Metal Foil Surface Modification: An Effective Method to Improve the Cycling Performance of Lithium-Metal Batteries. *Advanced Materials Interfaces*, **2017**, 4, 1700166.
[19] L. Ma, M. S. Kim, L. A. Archer, Stable Artificial Solid Electrolyte Interphases for Lithium Batteries. *Chemistry of Materials*, **2017**, 29, 4181.
[20] J. Zhao, Z. Lu, H. Wang, W. Liu, H. W. Lee, K. Yan, D. Zhuo, D. Lin, N. Liu, Y. Cui, Artificial Solid Electrolyte Interphase-Protected LixSi Nanoparticles: An Efficient and Stable Prelithiation Reagent for Lithium-Ion Batteries. *J Am Chem Soc*, **2015**, 137, 8372.
[21] J. W. Xiang, Y. Zhao, L. X. Yuan, C. J. Chen, Y. Shen, F. Hu, Z. X. Hao, J. Liu, B. X. Xu, Y. H. Huang, A strategy of selective and dendrite-free lithium deposition for lithium batteries. *Nano Energy*, **2017**, 42, 262.
[22] J. Dai, C. Shi, C. Li, X. Shen, L. Peng, D. Wu, D. Sun, P. Zhang, J. Zhao, A rational design of separator with substantially enhanced thermal features for lithium-ion batteries by the polydopamine–ceramic composite modification of polyolefin membranes. *Energy Environ. Sci.*, **2016**, 9, 3252.
[23] K. Liu, D. Zhuo, H. W. Lee, W. Liu, D. Lin, Y. Lu, Y. Cui, Extending the Life of Lithium-Based Rechargeable Batteries by Reaction of Lithium Dendrites with a Novel Silica Nanoparticle Sandwiched Separator. *Adv Mater*, **2017**, 29.
[24] J. Steiger, D. Kramer, R. Mönig, Microscopic observations of the formation, growth and shrinkage of lithium moss during electrodeposition and dissolution. *Electrochimica Acta*, **2014**, 136, 529.
[25] T. Nishida, K. Nishikawa, M. Rosso, Y. Fukunaka, Optical observation of Li dendrite growth in ionic liquid. *Electrochimica Acta*, **2013**, 100, 333.
[26] K. N. Wood, E. Kazyak, A. F. Chadwick, K. H. Chen, J. G. Zhang, K. Thornton, N. P. Dasgupta, Dendrites and Pits: Untangling the Complex Behavior of Lithium Metal Anodes through Operando Video Microscopy. *ACS Cent Sci*, **2016**, 2, 790.
[27] P. Bai, J. Li, F. R. Brushett, M. Z. Bazant, Transition of lithium growth mechanisms in liquid electrolytes. *Energy & Environmental Science*, **2016**, 9, 3221.
[28] A. Pei, G. Zheng, F. Shi, Y. Li, Y. Cui, Nanoscale Nucleation and Growth of Electrodeposited Lithium Metal. *Nano Lett*, **2017**, 17, 1132.
[29] L. Gireaud, S. Grugeon, S. Laruelle, B. Yrieix, J. M. Tarascon, Lithium metal stripping/plating mechanisms studies: A metallurgical approach. *Electrochemistry Communications*, **2006**, 8, 1639.
[30] R. Baddour-Hadjean, J. P. Pereira-Ramos, Raman microspectrometry applied to the study of electrode materials for lithium batteries. *Chem Rev*, **2010**, 110, 1278.
[31] A. J. Ilott, M. Mohammadi, C. M. Schauerman, M. J. Ganter, A. Jerschow, Rechargeable lithium-ion cell state of charge and defect detection by in-situ inside-out magnetic resonance imaging. *Nat Commun*, **2018**, 9, 1776.

[32] A. J. Ilott, M. Mohammadi, H. J. Chang, C. P. Grey, A. Jerschow, Real-time 3D imaging of microstructure growth in battery cells using indirect MRI. *Proc Natl Acad Sci U S A*, **2016**, 113, 10779.
[33] S. Lv, T. Verhallen, A. Vasileiadis, F. Ooms, Y. Xu, Z. Li, Z. Li, M. Wagemaker, Operando monitoring the lithium spatial distribution of lithium metal anodes. *Nat Commun*, **2018**, 9, 2152.
[34] M. Ebner, F. Marone, M. Stampanoni, V. Wood, Visualization and quantification of electrochemical and mechanical degradation in Li ion batteries. *Science*, **2013**, 342, 716.
[35] S. Muller, P. Pietsch, B. E. Brandt, P. Baade, V. De Andrade, F. De Carlo, V. Wood, Quantification and modeling of mechanical degradation in lithium-ion batteries based on nanoscale imaging. *Nat Commun*, **2018**, 9, 2340.
[36] T. M. M. Heenan, D. P. Finegan, B. Tjaden, X. Lu, F. Iacoviello, J. Millichamp, D. J. L. Brett, P. R. Shearing, 4D nano-tomography of electrochemical energy devices using lab-based X-ray imaging. *Nano Energy*, **2018**, 47, 556.
[37] K. Dong, H. Markotter, F. Sun, A. Hilger, N. Kardjilov, J. Banhart, I. Manke, In situ and Operando Tracking of Microstructure and Volume Evolution of Silicon Electrodes by using Synchrotron X-ray Imaging. *ChemSusChem*, **2019**, 12, 261.
[38] J. Wang, Y. C. Chen-Wiegart, J. Wang, In situ three-dimensional synchrotron X-Ray nanotomography of the (de)lithiation processes in tin anodes. *Angew Chem Int Ed Engl*, **2014**, 53, 4460.
[39] J. Wang, Y. C. Chen-Wiegart, J. Wang, In operando tracking phase transformation evolution of lithium iron phosphate with hard X-ray microscopy. *Nat Commun*, **2014**, 5, 4570.
[40] K. J. Harry, D. T. Hallinan, D. Y. Parkinson, A. A. MacDowell, N. P. Balsara, Detection of subsurface structures underneath dendrites formed on cycled lithium metal electrodes. *Nat Mater*, **2014**, 13, 69.
[41] D. S. Eastwood, P. M. Bayley, H. J. Chang, O. O. Taiwo, J. Vila-Comamala, D. J. Brett, C. Rau, P. J. Withers, P. R. Shearing, C. P. Grey *et al.*, Three-dimensional characterization of electrodeposited lithium microstructures using synchrotron X-ray phase contrast imaging. *Chem Commun (Camb)*, **2015**, 51, 266.
[42] F. Sun, R. Moroni, K. Dong, H. Markötter, D. Zhou, A. Hilger, L. Zielke, R. Zengerle, S. Thiele, J. Banhart *et al.*, Study of the Mechanisms of Internal Short Circuit in a Li/Li Cell by Synchrotron X-ray Phase Contrast Tomography. *ACS Energy Letters*, **2017**, 2, 94.
[43] F. Sun, L. Zielke, H. Markotter, A. Hilger, D. Zhou, R. Moroni, R. Zengerle, S. Thiele, J. Banhart, I. Manke, Morphological Evolution of Electrochemically Plated/Stripped Lithium Microstructures Investigated by Synchrotron X-ray Phase Contrast Tomography. *ACS Nano*, **2016**, 10, 7990.
[44] W. Gorner, M. P. Hentschel, B. R. Muller, H. Riesemeier, M. Krumrey, G. Ulm, W. Diete, U. Klein, R. Frahm, BAMline: the first hard X-ray beamline at BESSY II. *Nucl Instrum Meth A*, **2001**, 467, 703.
[45] D. Paganin, S. C. Mayo, T. E. Gureyev, P. R. Miller, S. W. Wilkins, Simultaneous phase and amplitude extraction from a single defocused image of a homogeneous object. *Journal of Microscopy*, **2002**, 206, 33.
[46] B. A. Dowd, G. H. Campbell, R. B. Marr, V. V. Nagarkar, S. V. Tipnis, L. Axe, D. P. Siddons, Developments in synchrotron x-ray computed microtomography at the National Synchrotron Light Source. *SPIE's International Symposium on Optical Science, Engineering, and Instrumentation*, **1999**, 3772, 224.
[47] C. T. Rueden, J. Schindelin, M. C. Hiner, B. E. DeZonia, A. E. Walter, E. T. Arena, K. W. Eliceiri, ImageJ2: ImageJ for the next generation of scientific image data. *BMC Bioinformatics*, **2017**, 18, 529.
[48] F. Sun, H. Markötter, I. Manke, A. Hilger, N. Kardjilov, J. Banhart, Three-Dimensional Visualization of Gas Evolution and Channel Formation inside a Lithium-Ion Battery. *ACS Appl Mater Interfaces*, **2016**, 8, 7156.
[49] P. Arora, Z. Zhang, Battery separators. *Chemical Reviews*, **2004**, 104, 4419.
[50] A. S. Westover, N. J. Dudney, R. L. Sacci, S. Kalnaus, Deposition and Confinement of Li Metal along an Artificial Lipon–Lipon Interface. *ACS Energy Letters*, **2019**, 4, 651.

[51] C. J. Orendorff, The Role of Separators in Lithium-Ion Cell Safety. *The Electrochemical Society Interface*, **2012**, 21, 61.
[52] Y. Li, Y. Li, A. Pei, K. Yan, Y. Sun, C. L. Wu, L. M. Joubert, R. Chin, A. L. Koh, Y. Yu *et al.*, Atomic structure of sensitive battery materials and interfaces revealed by cryo-electron microscopy. *Science*, **2017**, 358, 506.
[53] P. Bai, J. Guo, M. Wang, A. Kushima, L. Su, J. Li, F. R. Brushett, M. Z. Bazant, Interactions between Lithium Growths and Nanoporous Ceramic Separators. *Joule*, **2018**, 2, 2434.
[54] A. Niemoller, P. Jakes, R. A. Eichel, J. Granwehr, EPR Imaging of Metallic Lithium and its Application to Dendrite Localisation in Battery Separators. *Sci Rep*, **2018**, 8, 14331.
[55] L. Fan, S. Y. Li, L. Liu, W. D. Zhang, L. N. Gao, Y. Fu, F. Chen, J. Li, H. L. L. Zhuang, Y. Y. Lu, Enabling Stable Lithium Metal Anode via 3D Inorganic Skeleton with Superlithiophilic Interphase. *Advanced Energy Materials*, **2018**, 8, 1802350.
[56] Y. Li, Y. Qi, Energy landscape of the charge transfer reaction at the complex Li/SEI/electrolyte interface. *Energy & Environmental Science*, **2019**, 10.1039/c8ee03586e.
[57] R. Marom, S. F. Amalraj, N. Leifer, D. Jacob, D. Aurbach, A review of advanced and practical lithium battery materials. *Journal of Materials Chemistry*, **2011**, 21, 9938.
[58] Y. S. Cohen, Y. Cohen, D. Aurbach, Micromorphological studies of lithium electrodes in alkyl carbonate solutions using in situ atomic force microscopy. *J Phys Chem B*, **2000**, 104, 12282.
[59] H. Jo, D. Song, Y.-C. Jeong, Y. M. Lee, M.-H. Ryou, Study on dead-Li suppression mechanism of Li-hosting vapor-grown-carbon-nanofiber-based protective layer for Li metal anodes. *Journal of Power Sources*, **2019**, 409, 132.
[60] K. H. Chen, A. J. Sanchez, E. Kazyak, A. L. Davis, N. P. Dasgupta, Synergistic Effect of 3D Current Collectors and ALD Surface Modification for High Coulombic Efficiency Lithium Metal Anodes. *Advanced Energy Materials*, **2019**, 9, 1802534.
[61] C. Wang, Y. Zhao, Q. Sun, X. Li, Y. Liu, J. Liang, X. Li, X. Lin, R. Li, K. R. Adair *et al.*, Stabilizing interface between Li10SnP2S12 and Li metal by molecular layer deposition. *Nano Energy*, **2018**, 53, 168.
[62] X. Chen, W. He, L.-X. Ding, S. Wang, H. Wang, Enhancing interfacial contact in all solid state batteries with a cathode-supported solid electrolyte membrane framework. *Energy & Environmental Science*, **2019**, 12, 938.

Supporting information

Non-destructive Characterization of Lithium Deposition at the Li/Separator and Li/Carbon Matrix Interregion by Synchrotron X-ray Tomography

Kang Dong [a, b,*,✉], Markus Osenberg [a,*], Fu Sun [c], Henning Markötter [a], Charl J. Jafta[d], André Hilger [b], Tobias Arlt [a], John Banhart [a, b], Ingo Manke [b]

[a] Institute of Materials Science and Technology, Technische Universität Berlin, Straße des 17. Juni, 10623 Berlin, Germany

[b] Institute of Applied Materials, Helmholtz-Zentrum Berlin für Materialien und Energie, Hahn-Meitner-Platz 1, 14109 Berlin, Germany

[c] Qingdao Institute of BioEnergy and Bioprocess Technology, Chinese Academy of Sciences, 189 Songling Road 266101 Qingdao, PR China

[d] Institute of Soft Matter and Functional Materials, Helmholtz-Zentrum Berlin für Materialien und Energie, Hahn-Meitner-Platz 1, 14109 Berlin, Germany

✉ Corresponding author

Email: kang.dong@helmholtz-berlin.de

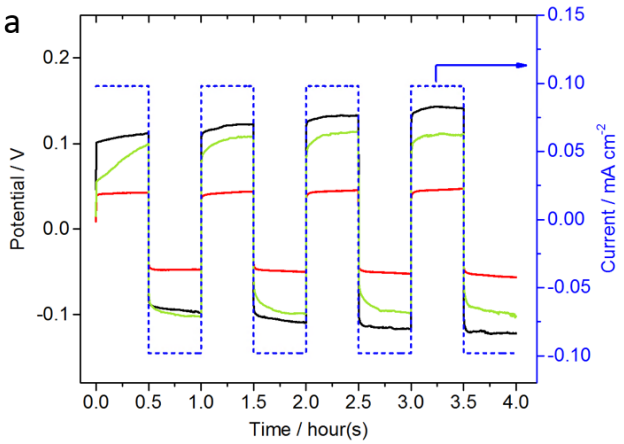

Figure S1. The voltage profiles of pre-cycling for cell activation of three Li/Li symmetric cells cycling at a low current density (0.1 mA·cm^{-2}). The black, green and red curve respectively corresponds to the cell charged at 0.1, 0.5, 1.0 mA·cm^{-2} during the following continuous charge in Fig. 1d.

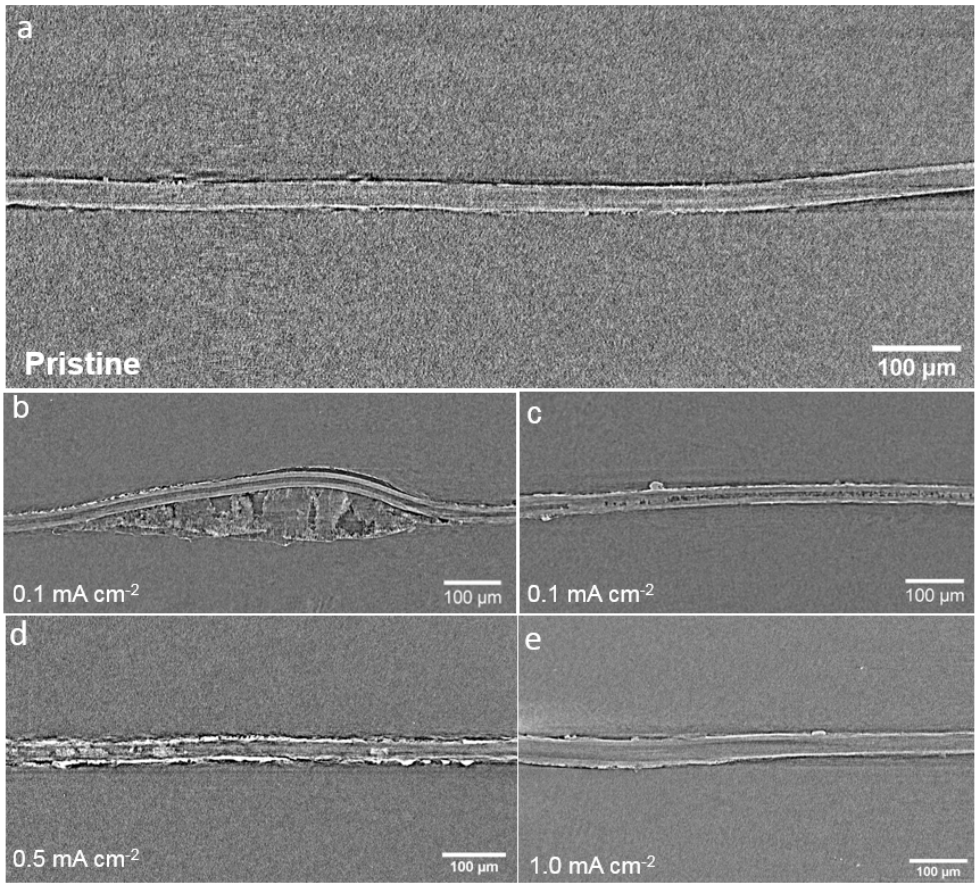

Figure. S2. Cross-sectional view of cells a) in the pristine state and after electrochemical deposition until short-circuit b-c) at 0.1 $mA \cdot cm^{-2}$, d) at 0.5 $mA \cdot cm^{-2}$ and e) at 1.0 $mA \cdot cm^{-2}$.

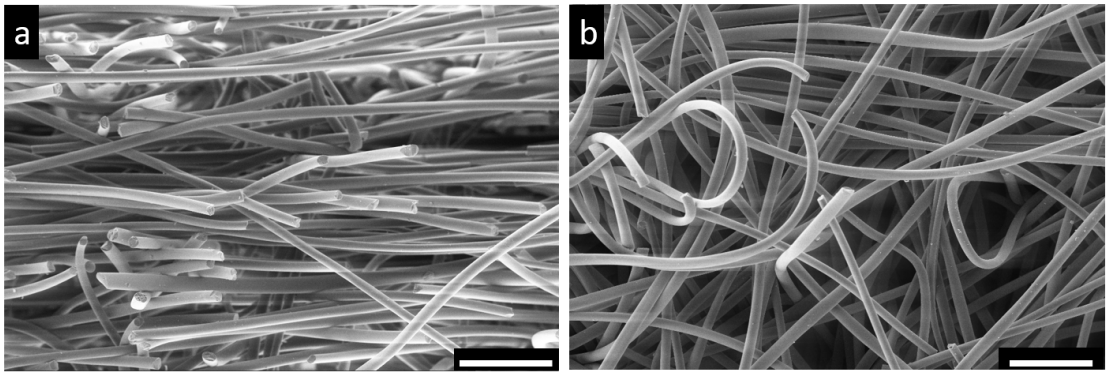

Figure S3. a) Cross-sectional view and b) in-plane view of the carbon fiber matrix used as a Li deposition host. The diameter of the fibers ranges from 8 to 15 µm. All scale bars represent 100 µm.

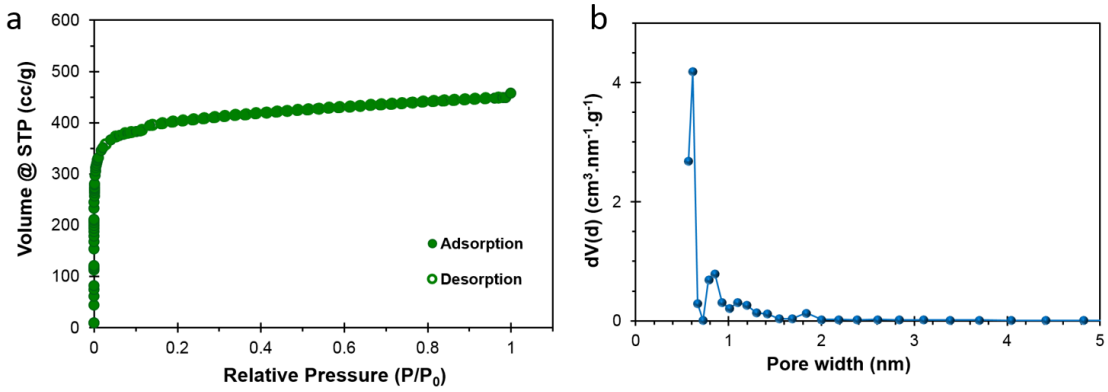

Figure S4. a) Adsorption and desorption behavior of the carbon fiber matrix measured by N_2 physisorption isotherm, which has a specific surface area of 1265 m^2/g determined by using the Brunauer-Emmett-Teller (BET) model. b) Pore size distribution of carbon fiber matrix derived from the physisorption isotherm by DFT calculations.

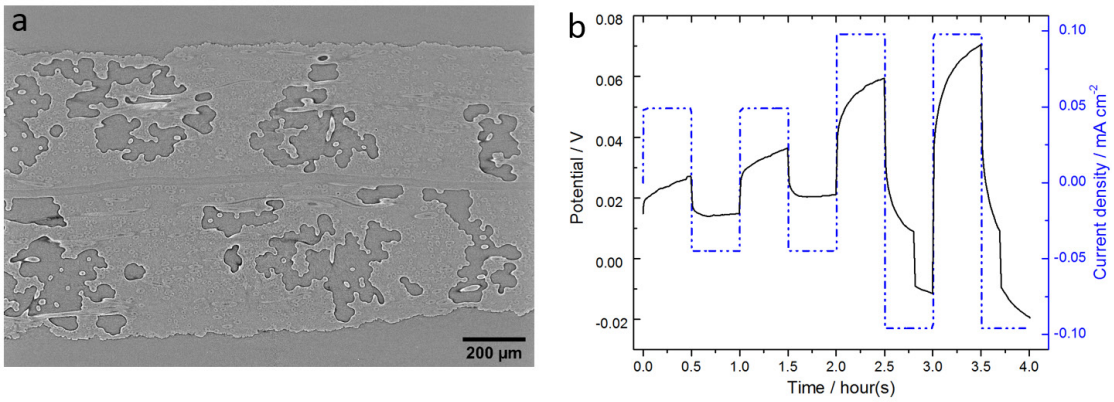

Figure S5. a) Cross-sectional view of reconstructed raw data of a Li-Carbon/Carbon-Li symmetric cell in the pristine state; b) voltage profile of the cell during pre-cycling for cell activation.

2.3 Nucleation and morphological transition of lithium deposition

K. Dong, M. Osenberg, J. Tan, *et al*, Quasi *in-situ* observation of nucleation and morphological transition of lithium electrodeposition in liquid electrolytes. *To be submitted*.

Quasi *in-situ* observation of nucleation and morphological transition of lithium electrodeposition in liquid electrolytes

Kang Dong [a, b], Markus Osenberg [a], Jinwang Tan [c], Fu Sun [d], Emily Ryan [e], John Banhart [a, b], Ingo Manke [b]

[a] Institute of Materials Science and Technology, Technische Universität Berlin, Straße des 17. Juni, 10623 Berlin, Germany

[b] Institute of Applied Materials, Helmholtz-Zentrum Berlin für Materialien und Energie, Hahn-Meitner-Platz 1, 14109 Berlin, Germany

[c] College of Mechatronics and Control Engineering, Shenzhen University, Shenzhen 518060, PR China

[d] Qingdao Institute of BioEnergy and Bioprocess Technology, Chinese Academy of Sciences, 189 Songling Road 266101 Qingdao, PR China

[e] Department of Mechanical Engineering, Boston University, 110 Cummington Mall, Boston, Massachusetts 02215, United States

Abstract

Li metal batteries have suffered from uneven Li electrodeposition (*e.g.* Li dendrites and fibres) and the concomitant potential short-circuits for nearly four decades. However, the nucleation and growth mechanism of the hazardous deposition which leads to safety concerns still remains elusive and inconclusive. In this study, focus ion beam scanning electron microscopy (FIB/SEM) was employed to unravel the nucleation and growth mechanism of Li electrodeposition in a liquid electrolyte. Li nucleation was found to preferably germinate from the surface irregularities (*i.e.* cracks and impurities) of the Li substrate. A transition of the lithium deposition was observed evolving from balls to bush-like deposits when increasing the deposition current density. Cross-sectional views obtained by focused ion beam reveal the inner structures of the Li deposition which provide new insights into the evolution process of Li deposition. In addition, computational modeling was used to further confirm the favorable nucleation sites and explain the nucleation and growth mechanism of Li deposition.

Keywords: Lithium deposition; Lithium dendrites; Lithium metal batteries; Focused ion beam

Introduction

Commercialized Li-ion batteries (LIB) using graphite anodes that are nearly approaching their theoretical capacity cannot meet the ever-increasing demands on batteries of high energy density for cutting-edge electronic devices and electric vehicles.[1, 2] With an ultrahigh theoretical capacity (3,860 mAh/g, 10 times larger than graphite anode (370 mAh g^{-1})) and the lowest redox potential (-3.04 V vs. standard hydrogen electrode), lithium (Li) metal anodes are regarded as a "holy grail" for next-generation batteries, *e.g.* Li-O_2 and Li-S batteries.[3, 4] Successful implementation of Li metal anodes has been widely regarded as the prerequisite for the practical commercialization of these batteries. However, this ultimate aim has been severely hindered by low Coulombic efficiency (CE) derived from side reactions and safety issues due to Li dendrite growth.

Due to the very high chemical reactivity of Li, side reactions between Li and the electrolyte occur from the onset of contact, accompanying the formation of the solid electrolyte interface (SEI) layer, thus leading to a low CE and continuous consumption of electrolyte.[5] Compared with the low CE, which could be partially resolved by using excess amounts of Li and electrolyte, Li dendrites (fibre-, whisker- or needle-like) that form during Li electrochemical plating are considered as the most critical obstacle to the practical application of Li metal batteries. Dendrites could penetrate the separator, induce an internal short circuit, or even cause a fire or explosion.[3, 6]

Over the last four decades, tremendous efforts have been devoted to mitigating Li dendrite formation, including Li deposition hosts[7-9], surface modifications of Li and/or the separator, novel electrolytes[10-12] and additives[13, 14]. Moreover, various imaging characterization techniques have also been employed to understand the Li plating process.[15, 16] For instance, *in situ* optical microscopy[17-20] and magnetic resonance imaging (MRI)[21-23] are able to provide real-time information of the Li structural growth non-destructively; however, the initial nucleation and subtle microstructure of Li dendrites remain uncovered due to limited resolution (c.a. sub-µm). Transmission electron microscopy (TEM)[24] and transmission X-ray microscopy (TXM)[25] enable high spatial resolution investigations, but electrodes are downsized to a small dimension that could not provide a whole macroscopic picture at the real battery scale. In addition, as Li deposits are susceptible to electron beam radiation during standard TEM studies, cryo-electron microscopy[24] was recently applied to resolve the nanostructure of Li dendrites while avoiding beam damage. In spite of significant progress being achieved to suppress dendrite growth, the mechanism of Li nucleation and growth still remains inconclusive.

A comprehensive understanding is crucial for developing strategies that can effectively control the Li deposition process during long term battery cycling. Herein, a custom-built cell close to the size of a practical cell was developed containing no separator but with approximately 1.3 mm height pre-reserved between two Li electrode disks. To

disclose the nucleation and growth mechanisms, which span several length scales, surface and cross-sectional analysis were combined using focus ion beam scanning electron microscopy (FIB/SEM) at multiple length scales. The cross-sectional view of Li deposits discloses the interior structure especially the backbone of the Li dendrite, which has been rarely presented. Since the electrodeposition occurred without external mechanical pressure, the crucial nucleation as well as the evolution of Li deposits can thus be preserved which would otherwise appear to be a flattened and compact deposition layer. In addition, to complete this comprehensive understanding computational modeling is used to study the electrode-electrolyte interface and understand how ion transport near the interface affects the growth and structure of Li dendrites under different charging conditions. This modeling complements and helps to explain the experimental characterization of the interface.

Results and discussion

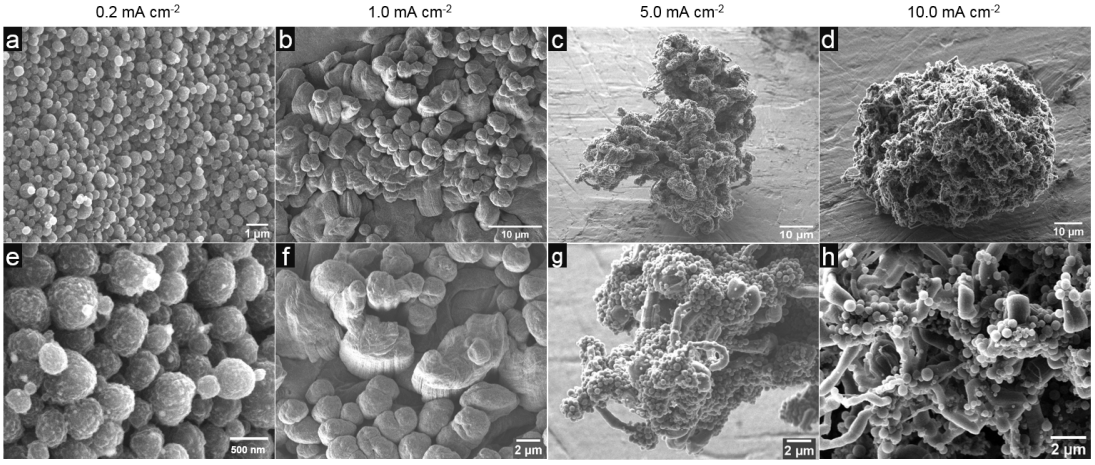

Figure 1. Lithium morphology transformation with increasing deposition current. (a-d) SEM images showing morphological features of Li deposition on Li substrate at current densities of 0.2, 1.0, 5.0, 10.0 mA cm^{-2}. (e-h) The corresponding magnified images of the SEM images (a-d) in the first row.

To explore the morphologies of Li deposition and optimize the cell operating conditions, Li/Li symmetric cells with the customized configuration were subjected to polarization at different current densities. Figure 1 shows the different appearances of deposits at varying current densities ranging from 0.2 mA cm^{-2} to 10 mA cm^{-2} after a fixed deposition capacity of 1.0 mAh cm^{-2}. At a deposition rate of 0.2 mA cm^{-2}, ball-like Li deposits with sub-µm sizes (c.a. 500 nm), as shown in Fig. 1a and 1e, spread and compactly stack up on the Li substrate. Except for the particles with an average size around 500 nm, smaller particles (< 300 nm) adhered to the bigger ones can also be observed. They are speculated to be the newly generated deposits and are expected to continue to grow if electrodeposition proceeds. The even deposition of particles and their similar particle morphologies indicate the uniformity of the local current density at the Li/electrolyte interface during electrochemical deposition. As the current density is increased to 1.0 mA cm^{-2}, the deposition in Fig. 1b and 1f become less uniform with

the co-existence of two different morphologies, namely granular and columnar. Compared to the ball-like particles generated at 0.2 mA cm^{-2} in Fig. 1e, the granular deposits are less spherical and bigger in size, indicating the decreasing nucleation sites. In addition, the columnar deposit which has also been observed in carbonate-based electrolytes[26], can be regarded as the precursor of dendritic deposition generated under a mixed control of charge transfer and ion diffusion.

With the increase of the current density to 5.0 mA cm^{-2}, bush-like Li deposits consisting of ball-like and dendrite depositions arise and grow on the Li substrate. Ball-like particles also appear under this elevated deposition rate. Instead of spreading on the surface of the substrate, these balls tend to deposit on the surface of the bush where new Li deposition exists with a thinner SEI layer thus lower electrochemical reduction resistance for Li^+. As shown in Fig. 1d and 1h, a similar morphological deposition could also be found at 10.0 mA cm^{-2} but with less granular balls and more randomly oriented whisker/dendrite structure when compared to the deposition in Fig. 1c and 1g.

As there is no separator induced reduction of the ionic conductivity in this separator-free cell and assuming that there is no convection in the cell, the diffusion-limiting current can be expressed by,

$$J_{lim} = 2z_c c_0 F D_{app} (t_a L)^{-1} \qquad (1)$$

where the charge number is $z_c = 1$, the bulk salt concentration is $c_0 = 1$ M, F is Faraday's constant, the anion transference number is $t_a = 1 - t_{Li}$ ($t_{Li} = 0.38$) in a diluted electrolyte, and the apparent diffusion coefficient is $D_{app} = 1.0 \times 10^{-6}$ cm^2 s^{-1}.[20, 27] Given the electrode spacing $L \approx 1.3$ mm, J_{lim} of this cell system can be readily calculated as $J_{lim} \approx 3.8$ mA cm^{-2}.

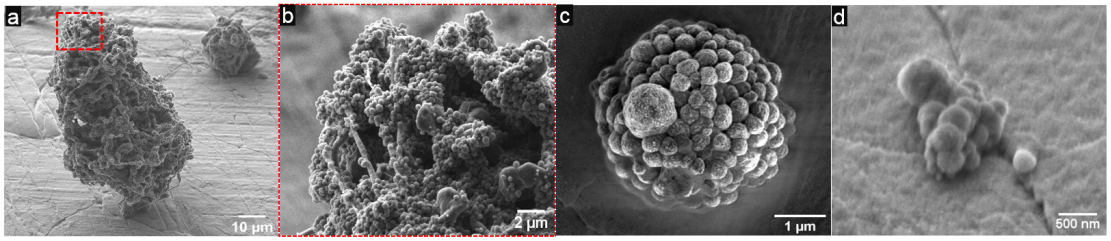

Figure 2. SEM images of Li deposits generated at 5.0 mA cm^{-2} at different length-scales. (a) SEM image of a bush-like dendritic deposit; (b) A magnified view of the top part of the dendrite in panel (a); (c) and (d) Li deposits at initial and nucleating stages.

Based on the diffusion limiting current (3.8 mA cm^{-2}) and our initial observations, 5.0 mA cm^{-2} was the optimal deposition rate for our experiments, as the non-dendritic deposits spread over and stack up on the substrate at lower current density (Fig. 1a and 1b). This enables us to explore the initial Li nucleation and dendrite evolution on the substrate. Figure 2 shows Li deposits at multiple length-scales ranging from a mature bush-like dendrite to the deposits at initial deposition stages with only one single or a cluster of nuclei. Similar to the deposits in Fig. 1a, this bush-like dendrite grew on the

Li substrate covered with Li fibres and balls; while the Li deposits at the initial deposition stage are composed of only ball-like nucleuses with analogous diameter sizes. The phenomenon that most ball-like deposits have similar diameter can be explained based on classic nucleation theory. The Gibbs energy ($\Delta G_{nucleation}$) as a function of the size (r) of a spherical nucleus, is the sum of bulk free energy (ΔG_{bulk}) and surface free energy ($\Delta G_{surface}$),

$$\Delta G_{nucleation} = -4/3\pi r^3 \Delta\mu / V_m + 4\pi r^2 \sigma \qquad (2)$$

where $\Delta\mu$ is related to the overpotential (η) via $\Delta\mu = zF\eta$, V_m is the molar volume, and σ is constant for a homogenous surface.[28] When differentiating $\Delta G_{nucleation}$ with respect to r, at a given overpotential the Gibbs free energy of nucleation has its maximum value at a radius of $r_{critical} = 2\sigma V_m / zF\eta$, which is known as the critical radius. This critical radius is the minimum nuclei size for stability and corresponds to the maximum $\Delta G_{nucleation}$.

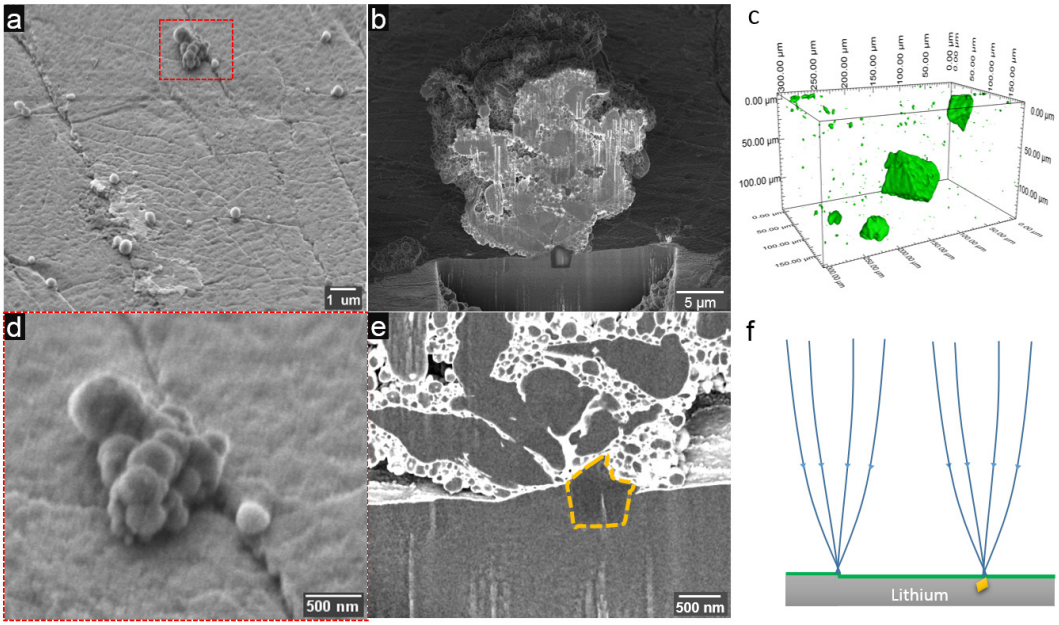

Figure 3. The nucleation sites of Li deposition. SEM images of (a) the Li nucleation sits on the Li substrate surface and (d) the corresponding magnification of the region marked by a red dashed rectangle in Fig. 3a. (b) A cross-sectional view of a bush-like deposit and (e) the magnified image of the root area of the deposit. These images were harvested from the Li electrode subjected to Li plating at 5.0 mA cm^{-2} for 0.2 h prior to SEM measurements. (c) Synchrotron X-ray tomography shows the impurities (crystals) inside Li substrate. (f) Schematic of the electric field at the surface irregularities (dislocations and impurity) of Li substrate. The green surface on the lithium refers to the SEI layer.

Unlike classical copper electrodeposition, the Li electrode, which is covered by an SEI layer has limited deposition sites over a given region as well as weak interactions between the substrate and deposit. Instead of a two-dimensional monomolecular layer growth, three-dimensional nuclei form on the Li surface, giving rise to the ball-like nuclei shown in Fig. 3a and 3d. These primary nuclei tend to stack up in clusters of nuclei during deposition, which can also be found in Fig. 2c. Interestingly, these nucleation sites are primarily found along or at rough regions on the Li. Roughness can

stem from intrinsic grain boundaries (usually from sub-μm to few μm) as well as dislocations and corrugation due to mechanical strain during the manufacturing process including lamination. Another factor that can substantially influence the nucleation site is subsurface impurities in the Li substrate. As shown in Fig. 3b and 3e, at the root of a bush-like dendrite, a faceted impurity particle was found, which could be attributed to the impurities involved during the manufacturing process. A previous study reported by K. Harry using synchrotron X-ray imaging also revealed similar impurities and suggested that areas with impurities underneath the Li surface were the favored deposition sites in Li-polymer cells.[29] In addition to increased chemical reactivity at the grain boundaries, local current densities at these micro-scaled surface irregularities are also higher than the flat areas during the electrodeposition process, which coincides with previous modeling results[30]. It has been regarded that the Li nucleation is associated with the surface conditions of the substrate but without conclusive proof.[31] Herein the high resolution and multiple-perspective resolvability of SEM/FIB enables us to show conclusively that micro-scaled surface irregularities (*i.e.* grain boundaries, dislocations, cracks and impurities) act as the preferred sites for the onset of electrodeposition. Additionally, in contrast to the view that Li is deposited beneath the SEI layer[32], the FIB/SEM images prove that Li deposition will occur above the SEI protective layer and proceed on the pre-generated Li nuclei.

To further reveal the internal structure of the deposition, the Li electrodes after plating at a capacity of 1.0 mAh cm^{-2} were milled by a source-focused gallium ion beam. Figure 4 shows the cross-sectional views of two representative morphologies, i.e. granular and bush-like, generated at current densities of 0.2 and 5.0 mA cm^{-2}, respectively. In Fig. 4a and 4c, the deposition at 0.2 mA cm^{-2} appears as solid ball-like particles with approximately 60-100 nm thick shells. The ball-like particles at the deposition surface layer possess thicker shells compared to the inner ones. These shells are attributed to the SEI layers that result from the side chemical reactions between deposited Li and electrolyte during electrochemical deposition. While the bush-like deposition of 5.0 mA cm features a different inner structure with ball-like particles covering trunk-like deposits (as highlighted in Fig. 4d). The white dots on the cutting surface are attributed to the Li components (Li and SEI layer) that fell and adhered to the surface during the vertical cutting, which is consistent with the white vertical lines on the cutting surface in Fig. 3b. Apart from solid balls, particles with a core-shell structure are also observable in Fig. 4d, especially at the surface of the bush-like dendrite. This could be attributed to a lower Li ions concentration induced by the weak electric field intensity at the root of the bush near the Li substrate. In addition, these core-shell balls can also be seen at the top of the bush-like dendrite but with lower bush height around 10 μm (Fig. S3) which is far from the bulk electrolyte and thus the Li ion concentration may be reduced. Hence, it could be speculated that during diffusion-controlled deposition, Li nucleation at low Li ion concentration areas could generate core-shell structures to minimize its surface energy and achieve a stable structure.

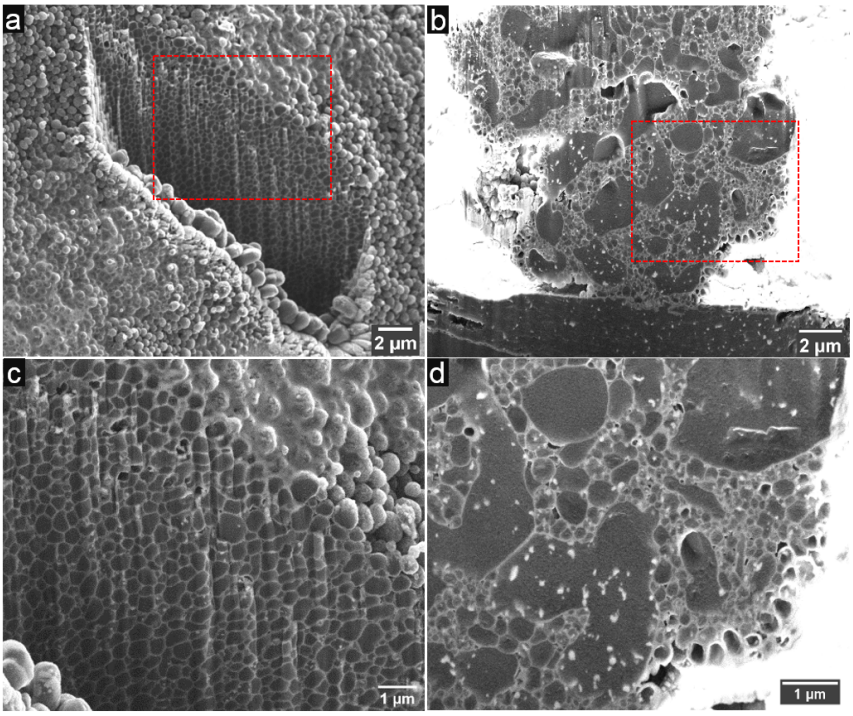

Figure 4. The internal morphology and structure of the granular and bush-like Li deposition. (a) A cross-sectional view and (c) the magnified view of the granular deposition at a current density of 0.2 mA cm^{-2}. (b) A cross-sectional view and (d) the magnified view of the bush-like deposition at a current density of 5.0 mA cm^{-2}.

Computational modeling of the electrode-electrolyte interface support the results obtained from SEM probing. A smoothed particle hydrodynamics (SPH) model of the interface is used to investigate how the deposition rate of Li affects the structure of the depositions. The model is based on a previous modeling of dendrite growth.[33-35] At low deposition rates (i.e. low current density), Li deposition is relatively uniform (Fig. 5a and 5b); however, as the deposition rate (current density) increases dendritic structures form (Fig, 5c and 5d). This coincides with the SEM images obtained at varying current densities. As the deposition rate increases, Li deposits transform into bush-like structures with various heights. Li ion concentrations near the top of the dendrite structures are higher than the root parts, leading to favorable conditions for vertical growth instead of lateral spread over the substrate. In addition to explaining the deposition morphologies, the distribution of Li ion concentration in Fig. 5 can also be employed to predict the subsequent preferred deposition sites, which usually occur at the electrochemically active interfacial regions that have higher Li ion flux.

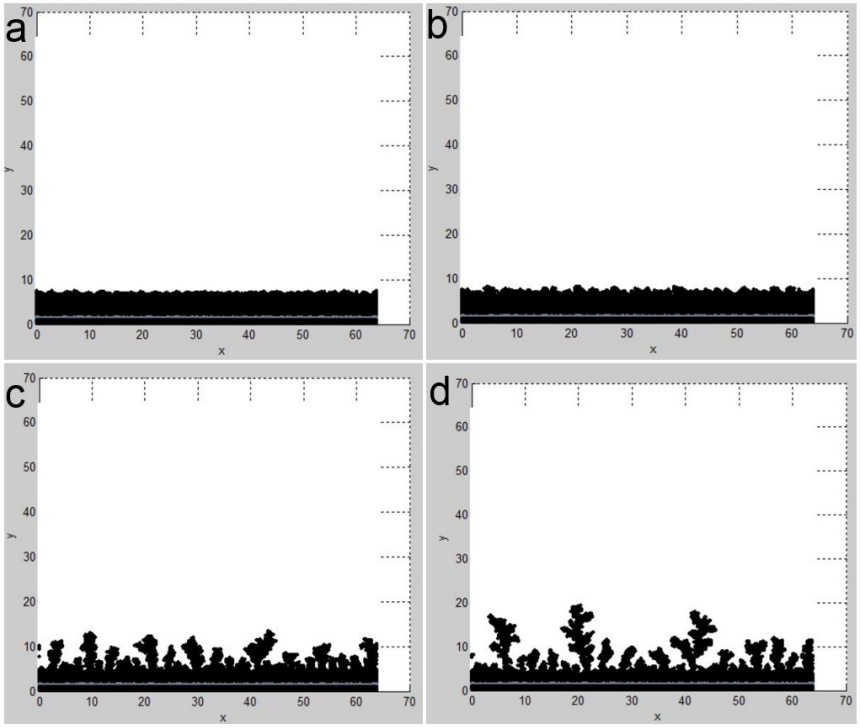

Figure 5. Simulations of Li electrodeposition at varying current densities. Morphologies and structural of the deposits obtained at **(**a) 0.2 mA cm^{-2}; (b) 1.0 mA cm^{-2}; (c) 5.0 mA cm^{-2}; (d) 10.0 mA cm^{-2}.

It is commonly regarded that inhomogeneous/dendritic deposition originates from 1) an inhomogeneous SEI which will induce "hot spots" for preferred deposition; 2) weak electrochemical stability and mechanical strength of the SEI layer leading to the exposure of fresh Li that is favorable for Li deposition[36]; 3) inhomogeneity of the Li^+ concentration on the anode surfaces. Instead of being attributed to the SEI properties and/or the ambiguous uneven Li ion flux which has not been well clarified, here we reveal that surface heterogeneity of the Li substrate could be one critical root cause for the initial inhomogeneous nucleation. As our experimental characterization shows and our computational simulations support, inhomogeneities promote dendrite nucleation and can lead to run-away dendrite growth, which leads to performance and safety issues in the battery. Therefore, it must be noted that mechanical pretreatment during practical cell assemble, such as rolling Li and scraping the Li surface with a razor blade, could introduce contaminations and increased surface inhomogeneities as uneven deposition sites, thus leading to undesired fast cell failure.

Except for metallic Li, other metals such as Li, copper, tungsten[19] and nickel[37], have also been used as deposition substrates. For these foreign substrates which usually have no typical SEI layer, surface inhomogeneities are also supposed to be the preferred initial nucleation regions. However, differences could appear between substrates with or without an SEI during the deposition process. Compared with using the Li substrate on which newly generated Li would be preferred, subsequent deposition on Cu is speculated to be more likely to appear adhering to the substrate due to good electron

conductivity of Cu as previously reported [38]. This will lead to a two-dimensional dispersive deposition morphology at the initial deposition stage instead of a 3D quasi-spherical segment shown in Fig. 2c, 2d. Further investigation regarding the deposition behavior on a Cu substrate and the differences from that on a Li substrate is crucial in the quest of achieving anode-free lithium batteries. The results and discussions aforementioned focus on the nucleation mechanism and evolution of Li deposition. Ongoing research aims to reveal the Li dissolution, the impacts of different cycling behavior as well as the chemical composition, which are crucial to get comprehensive and deep insights into the mechanism of Li stripping and dissolution.

Conclusions

In summary, quasi *in-situ* SEM techniques were used to investigate the free nucleation and growth of Li in liquid electrolyte at multiple length scales. Without a separator and external pressure, Li initial nucleation and the morphology evolution of deposition can be well reserved and clearly presented. Instead of being attributed to the SEI properties and/or the ambiguous uneven Li ion flux, the surface and cross-sectional images show conclusively that surface heterogeneity of the Li substrate is one critical root cause for the initial inhomogeneous nucleation. At current density below the diffusion limiting current, deposition morphology was found to evolve from ball-like to the co-existence of granular and columnar. At a higher current above the diffusion limiting current density, bush-like deposition appears with ball-like and fibre-like deposits covering the backbones of the bush. Computational modeling of the electrode-electrolyte interface further confirms the favorable nucleation sites and helps explain the nucleation and growth behavior, which could promote the fundamental understanding of Li nucleation and dendrite growth mechanism.

Experiment

1. Materials

Metallic lithium was purchased from MTI Corp. USA. The electrolyte of 1 M $LiPF_6$ with a mixture of ethylene carbonate (EC) and ethyl methyl carbonate (EMC) (1:1, v/v) and anhydrous dimethyl carbonate (DME) were received from Sigma-Aldrich. A Swagelok derived cell consisting of a polyamide-imide housing can be found in our previous report[39].

2. Battery assembly and characterization

The Li chips (0.45 mm thick) were received and elaborately punched into smaller disks with a diameter of 2.0 or 3.0 mm before use without further treatments. To build the tailor-made cell, a symmetrical Li/Li cell was built using 3.0 mm Li as the working electrode, 2.0 mm as the counter electrode and 70 ml electrolyte. Instead of using a separator, the two electrodes were separated by a 1.3 mm region filled by the electrolyte to avoid short-circuit, and more importantly for free dendrites nucleation, growth and evolution without external mechanical pressure. Then the assembled cells were galvanostatically charged at different current densities. Afterwards, the cells were disassembled in an argon-filled MBraun glovebox, where the working electrodes were removed from the cell. Before dried under vacuum, the electrode samples were rinsed by anhydrous DME to remove residual electrolyte. To avoid degradation, electrode samples were transported and protected by argon gas using a sealed container for the FIB/SEM measurement.

The morphological and structural characterization of the as-grown Li deposition on the electrode was investigated using a focused ion beam scanning electron microscopes (FIB-SEM, Zeiss Crossbeam 340). Galvanostatic charging of the cells was conducted using a Neware BTS4000 battery cycler.

Synchrotron X-ray tomography was conducted at the BAMline at the BESSY II electron storage ring of the Helmholtz-Zentrum Berlin, Germany.[40] The energy of the monochromatic X-ray beam was adjusted to 35 keV using a double multilayer monochromator with an energy resolution of about $\Delta E/E = 1.5\%$. These monochromatic synchrotron X-rays were directed onto the sample during a 180° sample rotation. The detector system consists of a 60-µm thick $CdWO_4$ scintillator, a set of microscope optics and a PCO4000 camera with a 4008 × 2672 pixel CCD sensor. A (3.5 × 2.34) mm^2 field of view was captured with a pixel size of 0.876 µm. A 2 by 2 binning was further used to decrease the scan time. The tomography dataset contains 1000 projections and 110 flatfields with an exposure time of 0.8 s for each projection/flatfield. The tomography dataset was reconstructed as previously reported[39]. 3D visualization shown in the context were obtained using VGStudio MAX 3.1.

3. Simulations

Smoothed particle hydrodynamics (SPH), a particle-based Lagrangian method is used to simulate reactive transport near the electrode-electrolyte interface.[41] SPH is a continuum-based method, which solves for the mass transport and surface reactions of Li ions near the interface. The model used in this study is based on previous work[33-35], which has included verification of the numerical model and validation with literature data.

Author Contributions

Kang Dong, Fu Sun and Ingo Manke designed the cell. Kang Dong assembled and cycled the cells. Kang Dong and Markus Osenberg conducted the FIB/SEM measurements. Kang Dong and Fu Sun conducted the synchrotron tomography measurement and composed the manuscript. Jinwan Tan and Emily Ryan conducted the simulation and aided in data interpretation. John Banhart and Ingo Manke directed the work. All authors contributed to the discussion of the results.

Notes

The authors declare no competing financial interest.

Acknowledgments

This work was sponsored by the Helmholtz Association and the China Scholarship Council (CSC). We would gratefully acknowledge Helmholtz-Zentrum Berlin for the FIB/SEM measurement time allocation. The authors would also like to thank John Schneider for cell fabrication.

References

[1] M. Armand, J.-M. Tarascon, Building better batteries. *Nature*, **2008**, 451, 652.
[2] P. G. Bruce, S. A. Freunberger, L. J. Hardwick, J. M. Tarascon, Li-O2 and Li-S batteries with high energy storage. *Nat Mater*, **2011**, 11, 19.
[3] X. B. Cheng, R. Zhang, C. Z. Zhao, Q. Zhang, Toward Safe Lithium Metal Anode in Rechargeable Batteries: A Review. *Chem Rev*, **2017**, 117, 10403.
[4] W. Xu, J. Wang, F. Ding, X. Chen, E. Nasybulin, Y. Zhang, J.-G. Zhang, Lithium metal anodes for rechargeable batteries. *Energy Environ. Sci.*, **2014**, 7, 513.
[5] D. Aurbach, E. Zinigrad, Y. Cohen, H. Teller, A short review of failure mechanisms of lithium metal and lithiated graphite anodes in liquid electrolyte solutions. *Solid State Ionics*, **2002**, 148, 405.
[6] M. Loveridge, G. Remy, N. Kourra, R. Genieser, A. Barai, M. Lain, Y. Guo, M. Amor-Segan, M. Williams, T. Amietszajew *et al.*, Looking Deeper into the Galaxy (Note 7). *Batteries*, **2018**, 4, 3.
[7] G. X. Li, Z. Liu, Q. Q. Huang, Y. Gao, M. Regula, D. W. Wang, L. Q. Chen, D. H. Wang, Stable metal battery anodes enabled by polyethylenimine sponge hosts by way of electrokinetic effects. *Nature Energy*, **2018**, 3, 1076.
[8] S. H. Wang, Y. X. Yin, T. T. Zuo, W. Dong, J. Y. Li, J. L. Shi, C. H. Zhang, N. W. Li, C. J. Li, Y. G. Guo, Stable Li Metal Anodes via Regulating Lithium Plating/Stripping in Vertically Aligned Microchannels. *Adv Mater*, **2017**, 29.
[9] N. Li, W. Wei, K. Xie, J. Tan, L. Zhang, X. Luo, K. Yuan, Q. Song, H. Li, C. Shen *et al.*, Suppressing Dendritic Lithium Formation Using Porous Media in Lithium Metal-Based Batteries. *Nano Lett*, **2018**, 18, 2067.
[10] A. Basile, A. I. Bhatt, A. P. O'Mullane, Stabilizing lithium metal using ionic liquids for long-lived batteries. *Nat Commun*, **2016**, 7, ncomms11794.
[11] C. Wang, Y. Zhao, Q. Sun, X. Li, Y. Liu, J. Liang, X. Li, X. Lin, R. Li, K. R. Adair *et al.*, Stabilizing interface between Li10SnP2S12 and Li metal by molecular layer deposition. *Nano Energy*, **2018**, 53, 168.
[12] J. A. Lewis, F. J. Q. Cortes, M. G. Boebinger, J. Tippens, T. S. Marchese, N. Kondekar, X. Liu, M. Chi, M. T. McDowell, Interphase Morphology between a Solid-State Electrolyte and Lithium Controls Cell Failure. *ACS Energy Letters*, **2019**, 4, 591.
[13] X.-Q. Zhang, X.-B. Cheng, X. Chen, C. Yan, Q. Zhang, Fluoroethylene Carbonate Additives to Render Uniform Li Deposits in Lithium Metal Batteries. *Advanced Functional Materials*, **2017**, 27, 1605989.
[14] F. Ding, W. Xu, G. L. Graff, J. Zhang, M. L. Sushko, X. Chen, Y. Shao, M. H. Engelhard, Z. Nie, J. Xiao *et al.*, Dendrite-free lithium deposition via self-healing electrostatic shield mechanism. *J Am Chem Soc*, **2013**, 135, 4450.
[15] F. Sun, L. Zielke, H. Markotter, A. Hilger, D. Zhou, R. Moroni, R. Zengerle, S. Thiele, J. Banhart, I. Manke, Morphological Evolution of Electrochemically Plated/Stripped Lithium Microstructures Investigated by Synchrotron X-ray Phase Contrast Tomography. *ACS Nano*, **2016**, 10, 7990.
[16] S. Lv, T. Verhallen, A. Vasileiadis, F. Ooms, Y. Xu, Z. Li, Z. Li, M. Wagemaker, Operando monitoring the lithium spatial distribution of lithium metal anodes. *Nat Commun*, **2018**, 9, 2152.
[17] K. N. Wood, E. Kazyak, A. F. Chadwick, K. H. Chen, J. G. Zhang, K. Thornton, N. P. Dasgupta, Dendrites and Pits: Untangling the Complex Behavior of Lithium Metal Anodes through Operando Video Microscopy. *ACS Cent Sci*, **2016**, 2, 790.
[18] T. Nishida, K. Nishikawa, M. Rosso, Y. Fukunaka, Optical observation of Li dendrite growth in ionic liquid. *Electrochimica Acta*, **2013**, 100, 333.

[19] J. Steiger, D. Kramer, R. Mönig, Microscopic observations of the formation, growth and shrinkage of lithium moss during electrodeposition and dissolution. *Electrochimica Acta*, **2014**, 136, 529.
[20] P. Bai, J. Li, F. R. Brushett, M. Z. Bazant, Transition of lithium growth mechanisms in liquid electrolytes. *Energy & Environmental Science*, **2016**, 9, 3221.
[21] A. J. Ilott, M. Mohammadi, H. J. Chang, C. P. Grey, A. Jerschow, Real-time 3D imaging of microstructure growth in battery cells using indirect MRI. *Proc Natl Acad Sci U S A*, **2016**, 113, 10779.
[22] S. Chandrashekar, N. M. Trease, H. J. Chang, L. S. Du, C. P. Grey, A. Jerschow, 7Li MRI of Li batteries reveals location of microstructural lithium. *Nat Mater*, **2012**, 11, 311.
[23] H. J. Chang, A. J. Ilott, N. M. Trease, M. Mohammadi, A. Jerschow, C. P. Grey, Correlating Microstructural Lithium Metal Growth with Electrolyte Salt Depletion in Lithium Batteries Using (7)Li MRI. *J Am Chem Soc*, **2015**, 137, 15209.
[24] Y. Li, Y. Li, A. Pei, K. Yan, Y. Sun, C.-L. Wu, L.-M. Joubert, R. Chin, A. L. Koh, Y. Yu, Atomic structure of sensitive battery materials and interfaces revealed by cryo–electron microscopy. *Science*, **2017**, 358, 506.
[25] J.-H. Cheng, A. A. Assegie, C.-J. Huang, M.-H. Lin, A. M. Tripathi, C.-C. Wang, M.-T. Tang, Y.-F. Song, W.-N. Su, B. J. Hwang, Visualization of Lithium Plating and Stripping via in Operando Transmission X-ray Microscopy. *The Journal of Physical Chemistry C*, **2017**, 121, 7761.
[26] F. Shi, A. Pei, A. Vailionis, J. Xie, B. Liu, J. Zhao, Y. Gong, Y. Cui, Strong texturing of lithium metal in batteries. *Proceedings of the National Academy of Sciences*, **2017**, 114, 12138.
[27] C. Capiglia, Y. Saito, H. Kageyama, P. Mustarelli, T. Iwamoto, T. Tabuchi, H. Tukamoto, 7Li and 19F diffusion coefficients and thermal properties of non-aqueous electrolyte solutions for rechargeable lithium batteries. *Journal of power sources*, **1999**, 81, 859.
[28] Y. D. Gamburg, G. Zangari, in *Theory and Practice of Metal Electrodeposition*. (Springer New York, New York, NY, 2011), 10.1007/978-1-4419-9669-5_5, pp. 97.
[29] K. J. Harry, D. T. Hallinan, D. Y. Parkinson, A. A. MacDowell, N. P. Balsara, Detection of subsurface structures underneath dendrites formed on cycled lithium metal electrodes. *Nat Mater*, **2014**, 13, 69.
[30] G. Yoon, S. Moon, G. Ceder, K. Kang, Deposition and Stripping Behavior of Lithium Metal in Electrochemical System: Continuum Mechanics Study. *Chemistry of Materials*, **2018**, 30, 6769.
[31] K. N. Wood, M. Noked, N. P. Dasgupta, Lithium Metal Anodes: Toward an Improved Understanding of Coupled Morphological, Electrochemical, and Mechanical Behavior. *ACS Energy Letters*, **2017**, 2, 664.
[32] J.-i. Yamaki, S.-i. Tobishima, K. Hayashi, S. Keiichi, Y. Nemoto, M. Arakawa, A consideration of the morphology of electrochemically deposited lithium in an organic electrolyte. *Journal of Power Sources*, **1998**, 74, 219.
[33] J. Tan, A. M. Tartakovsky, K. Ferris, E. M. Ryan, Investigating the Effects of Anisotropic Mass Transport on Dendrite Growth in High Energy Density Lithium Batteries. *Journal of The Electrochemical Society*, **2015**, 163, A318.
[34] J. Tan, E. M. Ryan, Computational study of electro-convection effects on dendrite growth in batteries. *Journal of Power Sources*, **2016**, 323, 67.
[35] J. Tan, E. M. Ryan, Structured electrolytes to suppress dendrite growth in high energy density batteries. *International Journal of Energy Research*, **2016**, 40, 1800.

[36] X. Guan, A. Wang, S. Liu, G. Li, F. Liang, Y. W. Yang, X. Liu, J. Luo, Controlling Nucleation in Lithium Metal Anodes. *Small*, **2018**, 14, 1801423.
[37] R. Mogi, M. Inaba, T. Abe, Z. Ogumi, In situ atomic force microscopy observation of lithium deposition at an elevated temperature. *Journal of Power Sources*, **2001**, 97-98, 265.
[38] A. Pei, G. Zheng, F. Shi, Y. Li, Y. Cui, Nanoscale Nucleation and Growth of Electrodeposited Lithium Metal. *Nano Lett*, **2017**, 17, 1132.
[39] K. Dong, M. Osenberg, F. Sun, H. Markötter, C. J. Jafta, A. Hilger, T. Arlt, J. Banhart, I. Manke, Non-destructive characterization of lithium deposition at the Li/separator and Li/carbon matrix interregion by synchrotron X-ray tomography. *Nano Energy*, **2019**, 62, 11.
[40] W. Gorner, M. P. Hentschel, B. R. Muller, H. Riesemeier, M. Krumrey, G. Ulm, W. Diete, U. Klein, R. Frahm, BAMline: the first hard X-ray beamline at BESSY II. *Nucl Instrum Meth A*, **2001**, 467, 703.
[41] J. J. Monaghan, Smoothed particle hydrodynamics. *Reports on progress in physics*, **2005**, 68, 1703.

Supporting information

Quasi *in situ* observation of nucleation and morphological transition of lithium deposition in liquid electrolytes

Kang Dong [a, b], Markus Osenberg [a], Jinwang Tan [c], Fu Sun [d], Emily Ryan [e], John Banhart [a, b], Ingo Manke [b]

[a] Institute of Materials Science and Technology, Technische Universität Berlin, Straße des 17. Juni, 10623 Berlin, Germany

[b] Institute of Applied Materials, Helmholtz-Zentrum Berlin für Materialien und Energie, Hahn-Meitner-Platz 1, 14109 Berlin, Germany

[c] College of Mechatronics and Control Engineering, Shenzhen University, Shenzhen 518060, PR China

[d] Qingdao Institute of BioEnergy and Bioprocess Technology, Chinese Academy of Sciences, 189 Songling Road 266101 Qingdao, PR China

[e] Department of Mechanical Engineering, Boston University, 110 Cummington Mall, Boston, Massachusetts 02215, United States

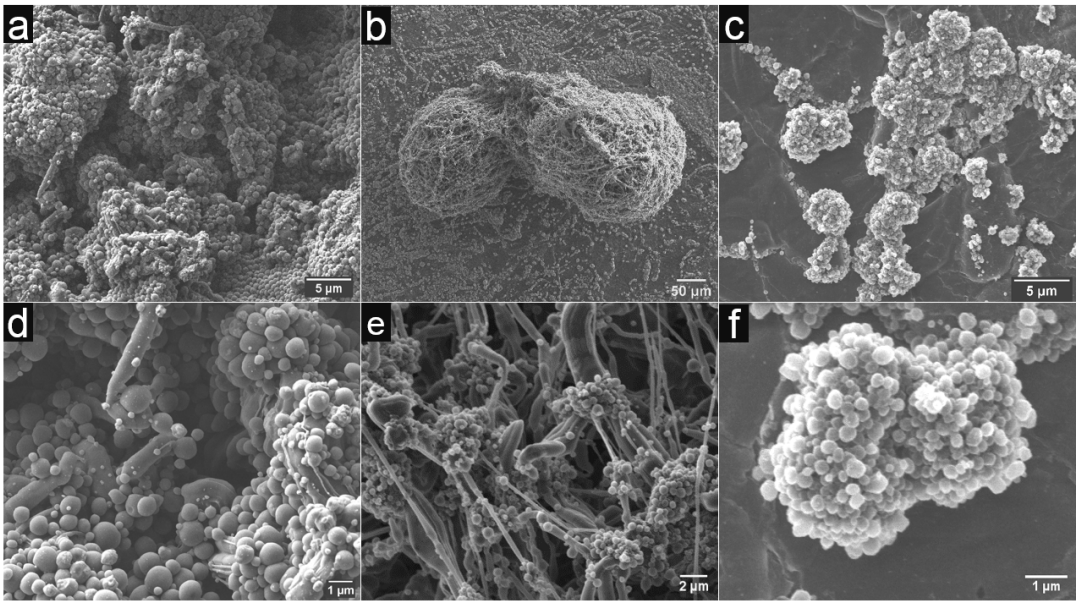

Figure S1. Li deposition morphologies after a deposition capacity of 1.0 mAh cm^{-2}. SEM images of deposition after (a) 2.5 h deposition conducted at 0.2 mA cm^{-2} followed by 0.1 h deposition at 5.0 mA cm^{-2}, and (b-c) 0.1 h deposition at 5.0 mA cm^{-2} followed by 2.5 h deposition conducted at 0.2 mA cm^{-2}. (d) and (e-f) are the magnified images of (a) and (b-c), respectively.

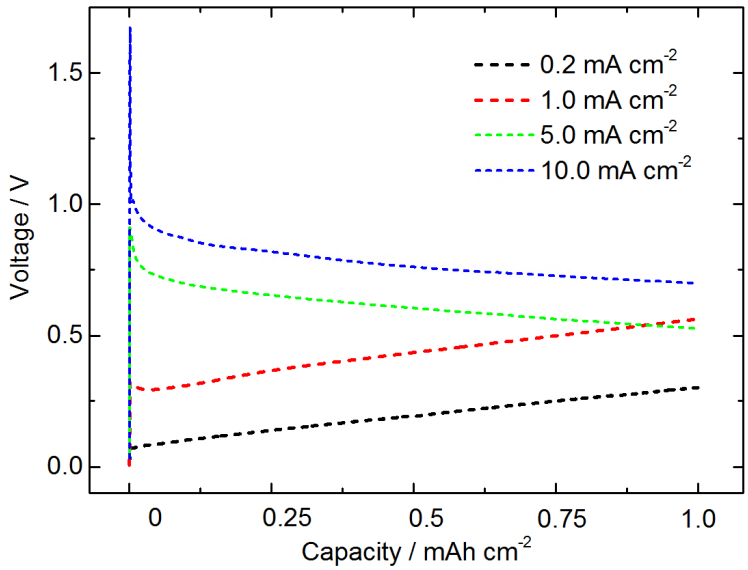

Figure S2. The typical voltage profiles of the cells charged at 0.2, 1.0, 5.0 and 10.0 mA cm^{-2} with a fixed deposition capacity of 1.0 mA h cm^{-2}. The obvious voltage peaks appear at the initial of deposition is the result of the electrochemical polarization. A higher current density typically leads to a higher deposition voltage plateau.

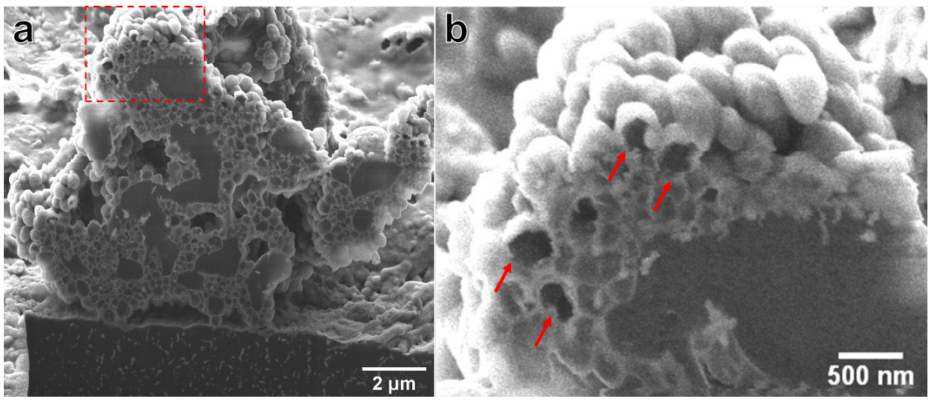

Figure S3. SEM images of a Li dendrite obtained at a polarization current density of 0.5 mA cm^{-2}. (a) An overview of a dendrite with a height around 10 μm; (b) the magnified image of the area marked by the dashed red line in (a). The arrows in (b) indicate the balls with a core-shell structure which have darker inner regions compared with the solid balls in (a).

2.4 Morphological evolution at InLi/LISION interface

F. Sun, K. Dong, M. Osenberg *et al*., Visualizing Morphological and Compositional Evolution of Interface of InLi-anode|thio-LISION Electrolyte in All-Solid-State Li-S Cell by in operando Synchrotron X-ray Tomography and Energy Dispersive Diffraction. *J. Mater. Chem. A*, **2018**, 6, 22489-22496. (DOI: 10.1039/C8TA08821G) [F.S and K.D. contributed equally to this work.]

Visualizing Morphological and Compositional Evolution of Interface of InLi-anode|thio-LISION Electrolyte in All-Solid-State Li-S Cell by *in operando* Synchrotron X-ray Tomography and Energy Dispersive Diffraction

Fu Sun,[1]*✉ Kang Dong,[1,2]* Markus Osenberg,[1,2] André Hilger,[1] Sebastian Risse,[3] Yan Lu,[3,4] Paul H. Kamm,[1] Manuela Klaus,[5] Henning Markötter,[1] Francisco García-Moreno,[1] Tobias Arlt[2] and Ingo Manke[1]

[1]Institute of Applied Materials
Helmholtz–Zentrum Berlin für Materialien und Energie
Hahn-Meitner-Platz 1, 14109 Berlin, Germany

[2]Institute of Material Science and Technologies
Technical University Berlin
Strasse des 17. Juni 135, 10623 Berlin, Germany

[3]Institute of Soft Matter and Functional Materials
Helmholtz–Zentrum Berlin für Materialien und Energie
Hahn-Meitner-Platz 1, 14109 Berlin, Germany

[4]Institute of Chemistry, University of Potsdam
Am Neuen Palais 10, House 9 14469 Potsdam, Germany

[5]Department of Microstructure and Residual Stress Analysis
Helmholtz–Zentrum Berlin für Materialien und Energie
Albert-Einstein-Straße 15, 12489 Berlin, Germany

Abstract

Dynamic and direct visualization of the interfacial evolution is helpful in gaining fundamental knowledge of all-solid-state-lithium battery working/degradation mechanisms and clarifying future research directions for constructing next-generation batteries. Herein, *in situ* and *in operando* synchrotron X-ray tomography and energy dispersive diffraction were simultaneously employed to record the morphological and compositional evolution of the interface of InLi-anode|sulfide-solid-electrolyte during battery cycling. Compelling morphological evidence of the interfacial degradation during all-solid-state-lithium battery operation has been directly visualized by

tomographic measurement. Accompanying energy dispersive diffraction result agrees well with the observed morphological deterioration and the recorded electrochemical performance. It is concluded from the current investigation that fundamental understanding of phenomena occurring at the solid-solid electrode|electrolyte interface during all-solid-state-lithium battery cycling is critical for future leaps in cell performance improvement and may determine its final commercial viability.

Developments in future battery technology are increasingly required to address the safety issues associated with the state-of-the-art lithium ion batteries (LIBs). Toyota Motor Corporation and Samsung R&D Institute Japan[1], for example, have devoted to promoting the application of all-solid-state lithium batteries (ASSLBs) in electric vehicles via replacing the conventional liquid electrolyte by the sulfide solid electrolyte (SE), which possesses high conductivity, good formability, favorable Young's modulus and moderate chemical stability[2]. However, in analogy to other inorganic oxide SEs[3], the interface between sulfide SE and battery electrode implies technical challenges for its practical application[4]. It has been discovered by ^{7}Li magnetic resonance imaging that Li distribution at the interface is inhomogeneous[5]. Moreover, Zhang *et al*. have directly observed significant interface bending caused by volume expansion by using X-ray tomography after battery cycling[6]. They later experimentally confirmed using electrochemical impedance spectroscopy that interfacial resistance increases drastically due to the interface degradation as a function of cycles[7]. Similar interface deterioration phenomena have been detected in inorganic oxide SEs by X-ray diffraction (XRD)[8], scanning electron microscopy[9], transmission electron microscopy[10], scanning transmission electron microscopy coupled with electron energy loss spectroscopy[11], time-of-flight secondary-ion mass spectrometry[12], X-ray photoelectron spectroscopy[13], Auger electron spectroscopy[14] and electron holography[15].

These in-depth studies have greatly enriched the understanding of the degradation mechanisms at the solid electrode|electrolyte interfaces which determine straightforwardly the overall electrochemical performance of ASSLBs. Nevertheless, *in operando* and nondestructive investigations[16] which could guarantee direct visual access to the dynamic evolution of interfaces under ASSLB operation, have not been reported due to the challenging characterization requirements, to the best of the authors' knowledge. Directly tracking the compositional and morphological evolution of the interfaces during electrochemical cycling would provide unprecedented benefits in gaining our understanding of the working/decaying/failure mechanisms of ASSLB and would contribute significantly to its industrial commercialization process.

Herein, *in operando* synchrotron X-ray tomography and energy dispersive diffraction were simultaneously employed to record the morphological and compositional evolution of the interface of anode|sulfide-SE for the first time. Specifically, the commercially available lithium tin phosphorous sulfide ($Li_{10}SnP_2S_{12}$, LSPS)[17] SE, a

LISION (LIthium Super-IONic conductor) belongs to LGPS ($Li_{10}GeP_2S_{12}$) family discovered by Kamaya *et al*. in 2011[18], was selected to assembly an all-solid-state lithium sulfur battery (ASSLSB). The indium-lithium (InLi) alloy (Li:In=2.34:1 in at% or 1.5:10.6 in wt%) and the Li_2S based composite (Li_2S:SE:C=3.5:4:2.5 in wt%) were used as anode and cathode, respectively. The mass of the used InLi anode, SE and composite cathode was 12.1, 5.6 and 0.4 mg, respectively. The diameter of the assembled electrode components was 3 mm and they were pressed under ~370 MPa. The cell was cycled successively at 1C, 0.5C, 0.25C and 0.1C at 70 ℃ during the *in operando* measurement. Detailed cell assembly and characterization procedures can be found in the *Methods* section. A photo of the designed cell and its schematic illustration, along with the illustration for the employed beamline setup are shown in Figure 1[19-24]. For the investigations targeted at the cathode side, readers can refer to previous reports[25-27].

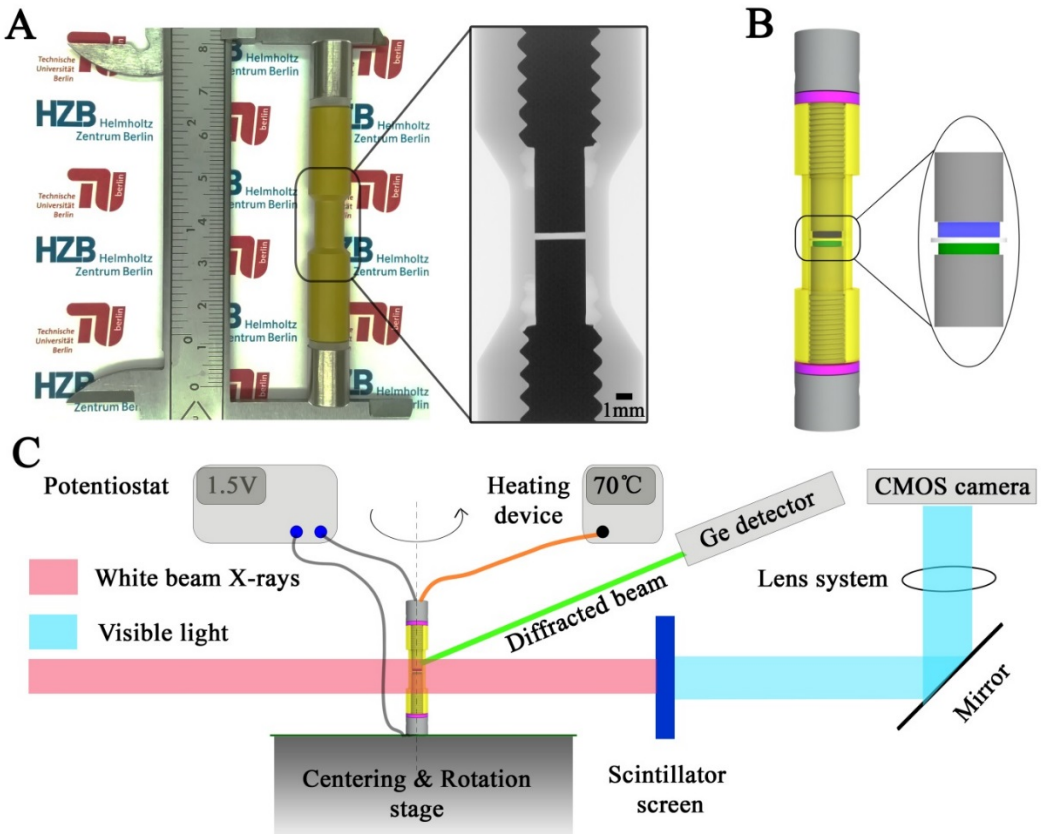

Figure 1. Photograph and schematic illustration of the customized electrochemical cell and the illustration of the employed beamline setup. A) Photograph of the fabricated cell, the enlarged picture in the black rectangle shows the interior of a blank cell, characterized by a laboratory X-ray setup. B) Corresponding schematic representation of the cell consisting of a polyamide-imide housing (yellow), two screws (light grey), two sealing rings (pink), solid $Li_{10}SnP_2S_{12}$ electrolyte (white) sandwiched between InLi anode and Li_2S based composite cathode (blue and green respectively). C) Schematic representation of the experimental setup of the tomography station at the EDDI beam line at BESSY II, Helmholtz-Zentrum Berlin, Germany. The cell was measured *in situ* and *in operando* during cycling by simultaneous synchrotron X-ray tomography and energy dispersive diffraction.

In this work, the cell undergoing four different cycles instead of long-term cycling was investigated due to the limited allocated beam time. Results from the first three cycles are shown in Figure 2 and the fourth cycle is shown in Figure 3. The electrochemical curves in Figure 2B and Figure 3B agree well with previous reports of ASSLSBs[28, 29]. The accompanying XRD and morphological recordings are shown in Figure 2A, Figure 3A and Figure 2C, Figure 3C, D respectively. It has to be pointed out that due to the high X-ray absorption of In/InLi, white beam at the employed EDDI beamline[30, 31] cannot fully penetrate the 3 mm diameter In/InLi. Only the relatively thinner part, *e.g.*, the protuberant or convex region, can be measured and analyzed (see results below). Note that the diffracted beam for XRD measurement has been focused on the interface of InLi-anode|LSPS-SE and the intensity scale bars in all XRD panels are different in order to maximize the principle diffraction line changes of InLi alloy during electrochemical cycling. Note also that, before the measurement, the cell underwent a conditioning charging at 10 µA for 5 hours and the curve is shown in Figure S1 in Supporting Information (SI). The whole *in operando* measurement is shown in a movie in SI.

From the first panel of Figure 2C, the InLi negative (Neg.) electrode and the LSPS electrolyte (Ele.) can be clearly observed due to the different X-ray absorption coefficient. The Li_2S composite positive (Pos.) electrode is located at the bottom and is shielded from the beam by the beam slits. In order to emphasize the morphological changes occurring during cycling, two features i.e. the length (vertical black line in Figure 2C) of the protrusion of the InLi Neg. and the distance (vertical yellow line in Figure 2C) between the selected SE particle and the bottom of the field of view (FoV) have been tracked. In Figure 2A, the principle diffraction line of InLi (422) is gray-color highlighted and a black vertical line indicates the principle diffraction line of In (202). During the first two cycles (1C and 0.5C), the XRD panels display mainly the InLi line (representing the starting composition (Li:In=2.34:1 in at%) and no significant morphological changes have been recorded (maybe due to the limited spatial resolution of 2.5 µm). However, during the third cycle noticeable morphological changes can be observed (last 5 panels in Figure 2C): The InLi protrusion has grown from 93 µm to 120 µm and the tracked distance between the SE particle and the bottom of the FoV has diminished from 123 µm to 113 µm. Moreover, from the accompanying XRD measurement (last panel in Figure 2A), it can be seen that the gradual decrease of the In peak is followed by the increase of the InLi peak during the charge process and vice versa during the discharge process.

Further significant changes can be observed from the measurement at the fourth cycle (0.1C), as shown in Figure 3. Note that Figure 3C shows the same region in Figure 2C and Figure 3D displays another region of the cell. The locations of these two regions are shown in Figure S2 in SI. After the fourth cycle (Figure 3B), the InLi protrusion has grown from 120 µm to 233 µm (first and last panel in Figure 3C), while the distance between the SE particle and the bottom of the FoV has further diminished to 108 µm

(compare the first and the last panel in Figure 3C). Figure 3D, another selected region, also displays tremendous morphological changes. Look closer at these morphological changes, one can find that primary changes occur during the charge process (red dots marking 1 to 6 in Figure 3B point to 6 panels in Figure 3C, D,), while during discharge (red dots marking 6 to 10 in Figure 3B), slight changes develop except the progressively built cavity/void between the InLi Neg. and SE (see white arrows in the last 4 panels in Figure 3C, D). Similar change behavior can be observed from the corresponding XRD measurements: Disappearance of the principle diffraction line of In is followed by appearance of the InLi line during the charge and limited variations can be discerned during the discharge. Comparing the measured principle diffraction line of InLi during the fourth cycle (1.397 Å) with that during the first three cycles (1.384 Å), slightly different *d* space value can be obtained.

Elucidating these observed results requires a reconsideration of the characteristic properties of the ASSLSB. It has to be pointed out that according to the XRD PDF card (00-003-0908), the *d* spacing value of InLi alloy at (hkl)=422 is 1.390 Å[32]. During the cell assembly, significant pressure has been employed to facilitate the interfacial contact of solid InLi-anode|LSPS SE (~370 MPa). Moreover, during the cell cycling, further pressure can be generated due to the tremendous volume change of In and Li_2S. Thus, it can be expected that these stress can result in noticeable lattice strain of InLi and resultantly, a smaller *d* value than 1.390 Å is obtained. On the other hand, the volume change induced interface degradation can be anticipated during cycling because no permanent pressure has been applied to this cell and the rigid solid electrode/electrolyte lacks the flexibility to transform/flow at free. As a result, after the delithiation of the InLi anode during the third cycle, the InLi lattice is probably under tensile stress (see the assumption below), generating a *d* value larger than 1.390 Å. Another reason for the explanation of the larger *d* value of 1.397 Å may be the formation of more lithium rich phases such as In_2Li_3 or $InLi_2$ during the de-alloying of InLi[33] and therefore an enrichment of indium (which has a larger atom radius than lithium) in the InLi phase (which has a wide compositional range). More sophisticated compositional investigations are needed for further clarification to distinguish different phases. Nevertheless, the volume caused build-up/release of the strain/stress in the electrode layer may further change the mechanical structure of the electrode|electrolyte interface and the connection between them can be weakened. This can be clearly observed in the last four panels of Figure 3C, D (see the white arrows). As a matter of fact, the pressure generation/release caused by (electro)chemical expansion/contraction of electrode materials during ASSLB cycling has been measured *in situ* via dilatometer by Zhang and coworkers[6, 34]. Unfortunately, to the best of the authors' knowledge, *in situ* XRD investigation of electrode/electrolyte materials in ASSBs has not been reported until now.

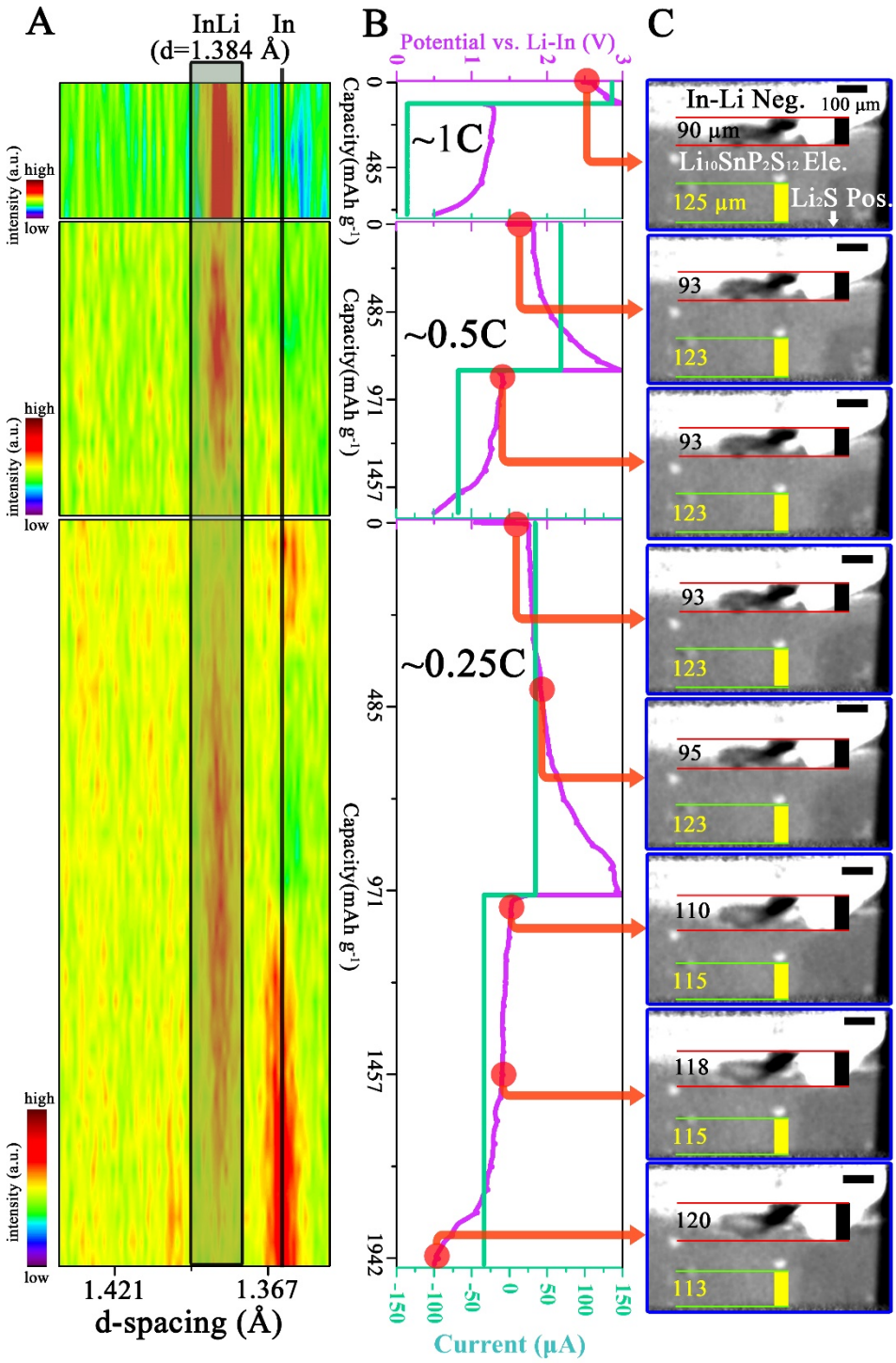

Figure 2. *In situ* and *in operando* measurement results of the cell from the first three cycles at 1C, 0.5C and 0.25C. A) The recorded XRD evolution as a function of cycle state. The principle diffraction line of In-Li alloy (hkl)=422 is gray-highlighted in a black rectangle and the black vertical line indicates the principle line of In (hkl)=202. B) The recorded voltage-current curves. C) Selected reconstructed slices showing the internal interfacial evolution as a function of battery state. The red points in B indicate the time where the slices in C are chosen. Note that the intensity scales in the three XRD panels are different and the location of the region shown in C is shown in Figure S2 in SI.

Clarifying the limited volume change of the InLi anode during discharge requests taking the In/InLi's high X-ray absorption and inflexibly property into consideration. Assuming cavities/voids develop due to the delithiation of InLi alloy near the current collector during discharge, they can be hardly detected by synchrotron X-ray tomography due to i) the X-ray cannot penetrate the surrounding In/InLi due to its high X-ray absorption and ii) the rigid In/InLi cannot shrink back automatically due to no applied external pressure. In contrary to the discharge process, the charge process induced morphological change can be easily detected because of the surficial In/InLi volume growth. Following focus will be concentrated on the quantification of the volume expansion after the 0.1C charge process electrochemically (from the electrochemical characterization) and morphologically (from the tomography characterization). The reconstructed tomography datasets at the beginning and ending of the 0.1C charge process have been binarized and the net volume expansion can be obtained through data subtraction. The 3D demonstration of the net volume expansion is shown in Figure S3 in SI and the value is calculated to be 4.58×10^7 μm^3. According to the reaction volume change of In/InLi anode proposed by Koerver *et al*.[34], which is $\Delta_v \approx 11.8 \times 10^{12}$ μm^3 mol^{-1}, the value of the expanded volume change calculated from the electrochemical characterization is $(I*t/F)*\Delta_v = 6.8 \times 10^7$ μm^3 (I is the charge current, t is charge time, F is the Faraday constant). The same order of magnitude of the volume expansion calculated morphologically and electrochemically during the charge process at 0.1C cycle indicates that almost all of the transferred Li has been alloyed with In instead of undergoing side reactions with the LSPS[17].

Currently observed interfacial cavity/void formation during battery cycling (last four panels in Figure 3C, D) induced by electrode volume changes and the rigid nature of solid electrode and electrolyte can be regarded as direct evidence for the mechanistic deterioration/degradation of the interface, as schematically shown in Figure 4. Due to the physical disconnection between the SE and the anode, it can be reasonably inferred that the partially disconnected anode will become electrochemically inactive, probably another reason for explaining the scarcely observed transformation of InLi peak in Figure 3A during the discharge process. Furthermore, the mechanistic deterioration of the interface will inevitably result in dramatic charge transfer resistance, giving direct rise to the experimentally observed internal resistance increase[7]. To conclude, the currently observed mechanistic deterioration/degradation of the interface would undoubtedly contribute to the overall electrochemical performance decay.

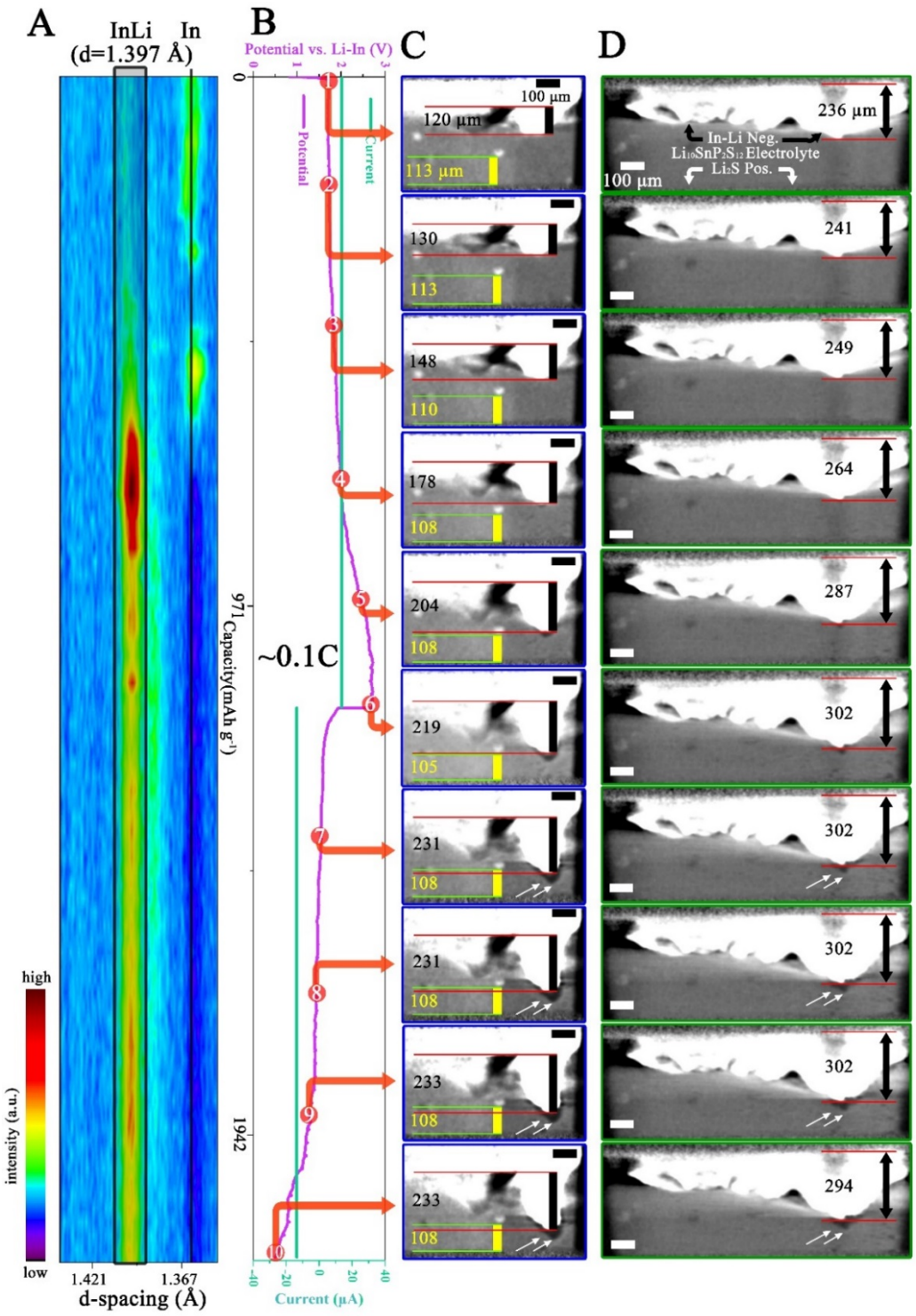

Figure 3. *In situ* and *in operando* measurement results of the cell from the fourth cycle at 0.1C. A) The recorded XRD evolution as a function of battery state. The principle diffraction line of In-Li alloy (hkl)=422 is gray-highlighted in a black rectangle and the black vertical line indicates the principle diffraction line of In (hkl)=202. B) The recorded voltage-current curves. C) and D) Selected reconstructed slices showing the internal interfacial evolution as a function of battery state. Note that C shows the same location as that in Figure 2C and D shows another region. The numbered red points in B indicate the time where the slices in C and D are chosen. Note that the intensity scale in this XRD panel is different from that in Figure 2A and the location of the region shown in D is displayed in Figure S2 in SI.

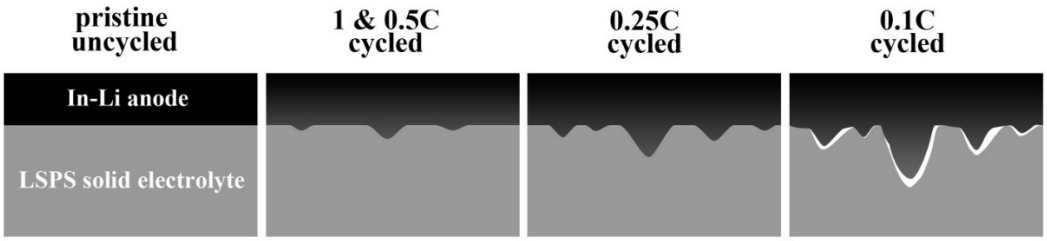

Figure 4. Schematic illustration of the observed morphological evolution of the interface of InLi anode|sulfide-solid-electrolyte during battery cycling. From left to right: the uncycled pristine state; the 1 and 0.5 C cycled state showing the volume expansion of the anode; the 0.25 C cycled state showing further developed changes; the 0.1 C cycled state showing significant interfacial degradation.

Combining the *in situ* and *in operando* synchrotron X-ray tomography and energy dispersive diffraction with the electrochemical characterization, direct visualization of the morphological and compositional evolution of the interface of InLi-anode|thio-LISION electrolyte in ASSLSB has been obtained. The compelling experimental evidence of the interfacial degradation has been clearly observed. Principal conclusions that can be drawn from the current investigation are discussed below.

First, the current investigation highlights the importance of preserving intimate contact during ASSLSB operation to maintain its electrochemical performance. Electrochemical reactions in ASSBs occur through the solid-solid interface between the electrode and SE materials, which is different from that in conventional LIBs with liquid electrolytes[35]. It has been generally acknowledged in the battery community that formation of intimate contact at the solid electrode|electrolyte interface is the key to improve the electrochemical performance of ASSBs because charge-transfer reactions occur only at the contacted interfaces[36]. Current findings of interfacial degradation during cycling (last four panels of Figure 3C, D) further suggest that maintenance of good interfacial contacts during ASSB operation is equally crucial to their establishment during ASSB assembly. Unfortunately, tremendous efforts have been concentrated on building an intimate interface contact during ASSB assembly by surface modification/buffer layer insertion, while insufficient studies have been devoted to investigate its sustainability upon battery cycling. It is suggested that more and more future work should be concentrated on improving the interfacial stability during ASSB operation.

Furthermore, investigating the (electro)chemical induced volume change and its effect on the mechanical integrity of the electrode|electrolyte interface is also of importance. For most electrode materials, varying degrees of volume change is inevitable during their de/lithiation[34]. Unlike the conventional LIBs using liquid electrolyte where the volume change can be cushioned/adsorbed by free liquid electrolyte, significant amount of stress/strain would be generated in their ASSBs counterpart due to its rigid entity. The favorable malleability and the ductility of sulfide SEs have been considered as advantageous merits because they guarantee easier and simpler ASSB assembly[37]. However, the present investigation challenges this hypothesis by pointing out that

sufficient electrode volume change from the anode side in high-capacity ASSBs may easily deform the soft sulfide SEs (see the deformation in Figure 3C, D) and jeopardize the battery's safety. Thus, a rethinking of the roles played by sulfide SEs is necessary and it can be concluded that the design of ASSBs requires consideration of other factors that are different from their liquid electrolyte LIB counterpart.

Last but not least, the current report emphasizes the importance of correlating interior battery components' evolution to the exterior electrochemical performance. Tremendous efforts have been concentrated on designing/engineering interfaces in ASSBs to improve their performance[38]. However, electrochemical evaluations can only give indirect and unspecific insights for the performance improvement. From the current report, it can be noted that the morphological and compositional evolution of electrode components that occur simultaneously during electrochemical cycling and also govern straightforwardly the overall performance cannot be represented from the voltage profiles (see the XRD panel, electrochemical panel and the morphological panels in Figure 3). This also applies to the (quasi)solid glass-polymer and/or ceramic-polymer electrolyte materials, which are considered as promising (quasi)solid electrolytes for next-generation ASSBs[39]. It is thus concluded from current report that sufficient attentions have to be paid to their structural/morphologic evolution when new strategies are proposed.

In a word, research on ASSBs is still in the very early stage even though steady progress on the improvement of Li ion conductivity in SEs has resulted in record high conductivity which rivals the conductivity of organic liquid electrolytes. It has been generally acknowledged that when the ohmic resistance of the ASSBs has been alleviated dramatically by the high ionic conductivity of SEs, the interfacial challenges originating from the solid-solid interface between solid electrodes and SE becomes significantly pronounced[40]. Fundamental understanding of phenomena occurring at the solid-solid electrode|electrolyte interface during cell cycling is thus critical for future leaps in cell performance improvement and may determine their final commercial viability.

Methods

Materials

Lithium and carbon black were purchased from MTI Cor. USA. The $Li_{10}SnP_2S_{12}$ (LSPS) solid electrolyte was purchased from NEI Corporation. The XRD pattern and the ionic conductivity of the used LSPS solid electrolyte are shown in Figure S4 in supporting information. The indium foil and Li_2S were purchased from Sigma Aldrich. The housing of the customized electrochemical beamline battery is made of polyamide-imide (Torlon) provided by Drake Plastics Europe. Polyimid tube of 3 mm diameter was purchased from DETAKTA GmbH, Germany.

Preparation of the all-solid-state Li-S battery

The composite positive electrode powder was obtained by mixing of the Li_2S, LSPS and carbon black in 3.5:4:2.5 in wt% with a mortar. The mixed composite (0.4 mg) was firstly placed in a polyimide tube (diameter of 3 mm), followed by the LSPS SE (5.9 mg), indium foil (10.6 mg) and lithium foil (1.5 mg). Afterwards, a pressure of ~370 MPa was applied to them to form a pellet. After releasing the pressure, the obtained pellet was sandwiched by two stainless-steel screws during cell assembly. The cell was properly sealed off before taking out of an inert argon atmosphere filled glovebox. Before measurements, the cell was placed in an oven at 60 ℃ for 12 hours to facilitate the formation of InLi alloy.

Beamline set-ups and In situ measurement

The white synchrotron beam generated by the 7T-Wiggler at the EDDI beamline, Bessy II, Berlin, used in current study has energies from 6 to 120 KeV. The detector system is comprised of a 200 μm thick LuAG:Ce scintillator, a Schneider Optics macro lens with a magnifying factor of ~4.4, a PCO DIMAX high speed camera (2016×2016 pixels) equipped with a CMOS chip that is kept out of the direct beam by using a mirror (white beam optic). The maximum field of view is 4×4 mm^2 (length × height).

The battery is mounted on the rotation table through a small screw on top of the electrode screw. The cell was remotely controlled by a potentiostat within the beamline hutch and it was kept electrochemical cycling at 1C, 0.5C, 0.25C and 0.1C through the complete characterization process. During electrochemical cycling, the cell was kept at 70 ℃. Every 15 minutes, one synchrotron X-ray tomography and energy dispersive diffraction measurement was conducted simultaneously during the cell 180 º rotation. Each complete measurement took around 90 seconds. The achieved pixel size was ~2.5 μm. The schematic illustration of the characterization methods at EDDI is briefly described in Figure 1.

Data reconstruction and analysis

The raw tomography data from EDDI was processed using in-house reconstruction software programmed in IDL 8.2. The data was first normalized, de-noised and in some cases, filtered. Then the filtered back projection was used for final reconstruction. 3D renderings shown in Figure S2 and S3 in Supporting Information were generated using VGStudio MAX 3.0.

During the XRD measurement, it was the energies (λ) measured while the angle θ was fixed. The acquired spectra were corrected by subtracting the spectrum of the un-cycled pristine cell to depict the occurring changes during cycling. During the XRD data analysis, the d-values can be calculated according to the Bragg's law. The XRD characterization result of the LSPS from a previous report[41] is shown in SI Figure S4A for comparison.

Associated Content

Supporting Information is available on the website or on Page 90.

Author Infomation

Corresponding Author

✉Email: fu.sun@helmholtz-berlin.de or sunfu1998@gmail.com

ORCID: 0000-0001-6787-6988

Author Contributions

*F.S and K.D. contributed equally to this work.

Notes

The authors declare no competing financial interest.

Acknowledgements

We thank engineer Norbert Beck and John Schneider for fabricating the beamline battery. This work is sponsored by China Scholarship Council, the German Research Foundation, DFG (Project No. MA 5039/4-1) and the Bundesministerium für Bildung und Forschung (BMBF, grant no. 03XP0115C, Liszuba).

References

[1] C. Sun, J. Liu, Y. Gong, D. P. Wilkinson, J. Zhang, Recent advances in all-solid-state rechargeable lithium batteries. *Nano Energy*, **2017**, 33, 363.
[2] A. Manthiram, X. Yu, S. Wang, Lithium battery chemistries enabled by solid-state electrolytes. *Nature Reviews Materials*, **2017**, 2, 16103.
[3] K. Kerman, A. Luntz, V. Viswanathan, Y.-M. Chiang, Z. Chen, Review—Practical Challenges Hindering the Development of Solid State Li Ion Batteries. *J Electrochem Soc*, **2017**, 164, A1731.
[4] J. Y. Seok, O. D. Yang, N. Y. Jin, P. K. Ho, Issues and Challenges for Bulk-Type All-Solid-State Rechargeable Lithium Batteries using Sulfide Solid Electrolytes. *Israel J Chem*, **2015**, 55, 472.
[5] P.-H. Chien, X. Feng, M. Tang, J. T. Rosenberg, S. O'Neill, J. Zheng, S. C. Grant, Y.-Y. Hu, Li Distribution Heterogeneity in Solid Electrolyte Li10GeP2S12 upon Electrochemical Cycling Probed by 7Li MRI. *The Journal of Physical Chemistry Letters*, **2018**, 9, 1990.
[6] W. Zhang, D. Schroder, T. Arlt, I. Manke, R. Koerver, R. Pinedo, D. A. Weber, J. Sann, W. G. Zeier, J. Janek, (Electro)chemical expansion during cycling: monitoring the pressure changes in operating solid-state lithium batteries. *Journal of Materials Chemistry A*, **2017**, 5, 9929.
[7] W. Zhang, D. A. Weber, H. Weigand, T. Arlt, I. Manke, D. Schröder, R. Koerver, T. Leichtweiss, P. Hartmann, W. G. Zeier *et al.*, Interfacial Processes and Influence of Composite

Cathode Microstructure Controlling the Performance of All-Solid-State Lithium Batteries. *ACS Applied Materials & Interfaces*, **2017**, 9, 17835.
[8] C. Hansel, S. Afyon, J. L. M. Rupp, Investigating the all-solid-state batteries based on lithium garnets and a high potential cathode - LiMn1.5Ni0.5O4. *Nanoscale*, **2016**, 8, 18412.
[9] F. Yonemoto, A. Nishimura, M. Motoyama, N. Tsuchimine, S. Kobayashi, Y. Iriyama, Temperature effects on cycling stability of Li plating/stripping on Ta-doped Li7La3Zr2O12. *J Power Sources*, **2017**, 343, 207.
[10] A. Brazier, L. Dupont, L. Dantras-Laffont, N. Kuwata, J. Kawamura, J. M. Tarascon, First Cross-Section Observation of an All Solid-State Lithium-Ion "Nanobattery" by Transmission Electron Microscopy. *Chem Mater*, **2008**, 20, 2352.
[11] Z. Wang, D. Santhanagopalan, W. Zhang, F. Wang, H. L. Xin, K. He, J. Li, N. Dudney, Y. S. Meng, In Situ STEM-EELS Observation of Nanoscale Interfacial Phenomena in All-Solid-State Batteries. *Nano Lett*, **2016**, 16, 3760.
[12] S. Wang, H. Xu, W. Li, A. Dolocan, A. Manthiram, Interfacial Chemistry in Solid-State Batteries: Formation of Interphase and Its Consequences. *J Am Chem Soc*, **2018**, 140, 250.
[13] R. Koerver, F. Walther, I. Aygun, J. Sann, C. Dietrich, W. G. Zeier, J. Janek, Redox-active cathode interphases in solid-state batteries. *Journal of Materials Chemistry A*, **2017**, 5, 22750.
[14] E. J. Cheng, A. Sharafi, J. Sakamoto, Intergranular Li metal propagation through polycrystalline Li6.25Al0.25La3Zr2O12 ceramic electrolyte. *Electrochim Acta*, **2017**, 223, 85.
[15] Y. Kazuo, I. Yasutoshi, A. Toru, H. Tsukasa, F. Hideki, F. C. A. J., N. Katsumasa, S. Yuji, O. Zempachi, Dynamic Visualization of the Electric Potential in an All-Solid-State Rechargeable Lithium Battery. *Angew Chem Int Ed*, **2010**, 49, 4414.
[16] F. Sun, H. Markötter, D. Zhou, S. S. S. Alrwashdeh, A. Hilger, N. Kardjilov, I. Manke, J. Banhart, In Situ Radiographic Investigation of (De)Lithiation Mechanisms in a Tin-Electrode Lithium-Ion Battery. *ChemSusChem*, **2016**, 9, 946.
[17] I. Tarhouchi, V. Viallet, P. Vinatier, M. Ménétrier, Electrochemical characterization of Li10SnP2S12: An electrolyte or a negative electrode for solid state Li-ion batteries? *Solid State Ionics*, **2016**, 296, 18.
[18] N. Kamaya, K. Homma, Y. Yamakawa, M. Hirayama, R. Kanno, M. Yonemura, T. Kamiyama, Y. Kato, S. Hama, K. Kawamoto *et al.*, A lithium superionic conductor. *Nature Materials*, **2011**, 10, 682.
[19] F. Sun, M. Osenberg, K. Dong, D. Zhou, A. Hilger, C. J. Jafta, S. Risse, Y. Lu, H. Markötter, I. Manke, Correlating Morphological Evolution of Li Electrodes with Degrading Electrochemical Performance of Li/LiCoO2 and Li/S Battery Systems: Investigated by Synchrotron X-ray Phase Contrast Tomography. *ACS Energy Letters*, **2018**, 3, 356.
[20] F. Sun, R. Moroni, K. Dong, H. Markötter, D. Zhou, A. Hilger, L. Zielke, R. Zengerle, S. Thiele, J. Banhart *et al.*, Study of the Mechanisms of Internal Short Circuit in a Li/Li Cell by Synchrotron X-ray Phase Contrast Tomography. *ACS Energy Letters*, **2017**, 2, 94.
[21] F. Sun, L. Zielke, H. Markötter, A. Hilger, D. Zhou, R. Moroni, R. Zengerle, S. Thiele, J. Banhart, I. Manke, Morphological Evolution of Electrochemically Plated/Stripped Lithium Microstructures Investigated by Synchrotron X-ray Phase Contrast Tomography. *ACS Nano*, **2016**, 10, 7990.
[22] F. Sun, H. Markötter, K. Dong, I. Manke, A. Hilger, N. Kardjilov, J. Banhart, Investigation of failure mechanisms in silicon based half cells during the first cycle by micro X-ray tomography and radiography. *Journal of Power Sources*, **2016**, 321, 174.
[23] F. Sun, H. Markötter, I. Manke, A. Hilger, N. Kardjilov, J. Banhart, Three-Dimensional Visualization of Gas Evolution and Channel Formation inside a Lithium-Ion Battery. *ACS Applied Materials & Interfaces*, **2016**, 8, 7156.
[24] L. Zielke, F. Sun, H. Markötter, A. Hilger, R. Moroni, R. Zengerle, S. Thiele, J. Banhart, I. Manke, Synchrotron X-ray Tomographic Study of a Silicon Electrode Before and After Discharge and the Effect of Cavities on Particle Fracturing. *ChemElectroChem*, **2016**, 3, 1170.
[25] M. Nagao, A. Hayashi, M. Tatsumisago, T. Ichinose, T. Ozaki, Y. Togawa, S. Mori, Li2S nanocomposites underlying high-capacity and cycling stability in all-solid-state lithium–sulfur batteries. *J Power Sources*, **2015**, 274, 471.

[26] T. Takeuchi, H. Kageyama, K. Nakanishi, M. Tabuchi, H. Sakaebe, T. Ohta, H. Senoh, T. Sakai, K. Tatsumi, All-Solid-State Lithium Secondary Battery with Li2S – C Composite Positive Electrode Prepared by Spark-Plasma-Sintering Process. *J Electrochem Soc*, **2010**, 157, A1196.
[27] K. Dong, S. Wang, J. Yu, A lithium/polysulfide semi-solid rechargeable flow battery with high output performance. *RSC Advances*, **2014**, 4, 47517.
[28] H. Takashi, H. Akitoshi, T. Masahiro, Li2S-Based Solid Solutions as Positive Electrodes with Full Utilization and Superlong Cycle Life in All-Solid-State Li/S Batteries. *Advanced Sustainable Systems*, **2017**, 1, 1700017.
[29] H. Nagata, Y. Chikusa, An all-solid-state lithium–sulfur battery using two solid electrolytes having different functions. *Journal of Power Sources*, **2016**, 329, 268.
[30] G.-M. F., J. C., K. P. H., K. M., W. G., B. J., G. Ch., White-beam X-ray radioscopy and tomography with simultaneous diffraction at the EDDI beamline. *J Synchrotron Radiat*, **2013**, 20, 809.
[31] F. Garcia-Moreno, P. H. Kamm, T. R. Neu, J. Banhart, Time-resolved in situ tomography for the analysis of evolving metal-foam granulates. *J Synchrotron Radiat*, **2018**, 25, Doi: 10.1107/S1600577518008949.
[32] T. S. Huang, J. O. Brittain, Defect structure and mechanical behavior of B□LiIn. *Materials Science and Engineering*, **1987**, 93, 83.
[33] W. A. Alexander, L. D. Calvert, R. H. Gamble, K. Schinzel, The lithium–indium system. *Canadian Journal of Chemistry*, **1976**, 54, 1052.
[34] R. Koerver, W. Zhang, L. de Biasi, S. Schweidler, A. O. Kondrakov, S. Kolling, T. Brezesinski, P. Hartmann, W. G. Zeier, J. Janek, Chemo-mechanical expansion of lithium electrode materials - on the route to mechanically optimized all-solid-state batteries. *Energy Environ Sci*, **2018**, 10.1039/C8EE00907D.
[35] S. Kinoshita, K. Okuda, N. Machida, M. Naito, T. Sigematsu, All-solid-state lithium battery with sulfur/carbon composites as positive electrode materials. *Solid State Ionics*, **2014**, 256, 97.
[36] C. Yu, S. Ganapathy, N. J. J. de Klerk, I. Roslon, E. R. H. van Eck, A. P. M. Kentgens, M. Wagemaker, Unravelling Li-Ion Transport from Picoseconds to Seconds: Bulk versus Interfaces in an Argyrodite Li6PS5Cl–Li2S All-Solid-State Li-Ion Battery. *J Am Chem Soc*, **2016**, 138, 11192.
[37] T. W. Kim, K. H. Park, Y. E. Choi, J. Y. Lee, Y. S. Jung, Aqueous-solution synthesis of Na3SbS4 solid electrolytes for all-solid-state Na-ion batteries. *Journal of Materials Chemistry A*, **2018**, 6, 840.
[38] M. Keller, A. Varzi, S. Passerini, Hybrid electrolytes for lithium metal batteries. *J Power Sources*, **2018**, 392, 206.
[39] S. Xin, Y. You, S. Wang, H.-C. Gao, Y.-X. Yin, Y.-G. Guo, Solid-State Lithium Metal Batteries Promoted by Nanotechnology: Progress and Prospects. *ACS Energy Letters*, **2017**, 2, 1385.
[40] K. Takada, T. Ohno, N. Ohta, T. Ohnishi, Y. Tanaka, Positive and Negative Aspects of Interfaces in Solid-State Batteries. *ACS Energy Letters*, **2018**, 3, 98.
[41] P. Bron, S. Johansson, K. Zick, J. Schmedt auf der Günne, S. Dehnen, B. Roling, Li10SnP2S12: An Affordable Lithium Superionic Conductor. *J Am Chem Soc*, **2013**, 135, 15694.

Supporting information

Visualizing Morphological and Compositional Evolution of Interface of InLi-anode|thio-LISION Electrolyte in All-Solid-State Li-S Cell by *in operando* Synchrotron X-ray Tomography and Energy Dispersive Diffraction

Fu Sun,[1]*✉ Kang Dong,[1,2]* Markus Osenberg,[1,2] André Hilger,[1] Sebastian Risse,[3] Yan Lu,[3,4] Paul H. Kamm,[1] Manuela Klaus,[5] Henning Markötter,[1] Francisco García-Moreno,[1] Tobias Arlt[2] and Ingo Manke[1]

[1]Institute of Applied Materials
Helmholtz–Zentrum Berlin für Materialien und Energie
Hahn-Meitner-Platz 1, 14109 Berlin, Germany

[2]Institute of Material Science and Technologies
Technical University Berlin
Strasse des 17. Juni 135, 10623 Berlin, Germany

[3]Institute of Soft Matter and Functional Materials
Helmholtz–Zentrum Berlin für Materialien und Energie
Hahn-Meitner-Platz 1, 14109 Berlin, Germany

[4]Institute of Chemistry, University of Potsdam
Am Neuen Palais 10, House 9 14469 Potsdam, Germany

[5]Department of Microstructure and Residual Stress Analysis
Helmholtz–Zentrum Berlin für Materialien und Energie
Albert-Einstein-Straße 15, 12489 Berlin, Germany

This file contains the figures Figure S1-S4.

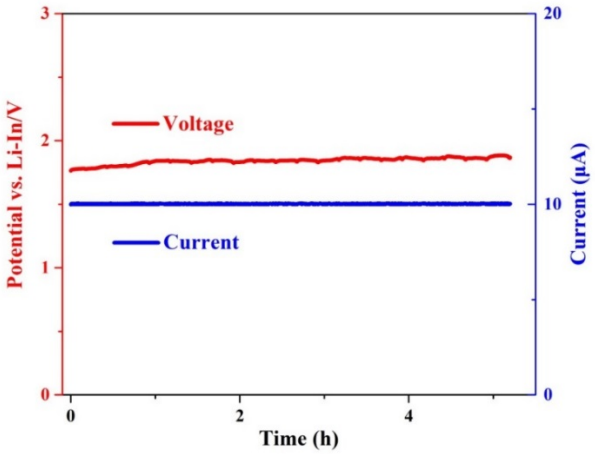

Figure S1. Electrochemical curve during the 10 μA conditional charging.

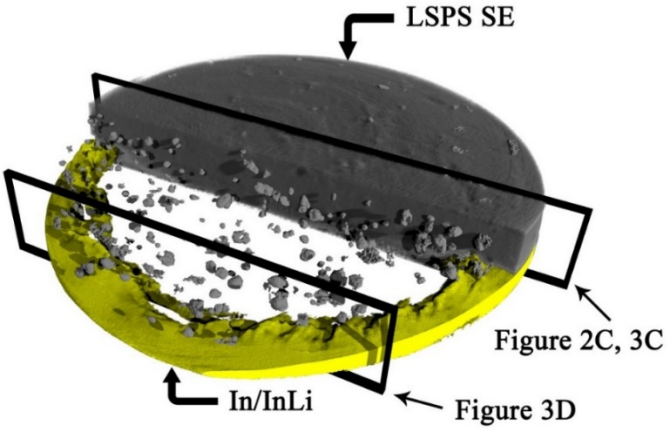

Figure S2. 3D rendering showing the location of the regions shown in Figure 2C/Figure 3C and Figure 3D.

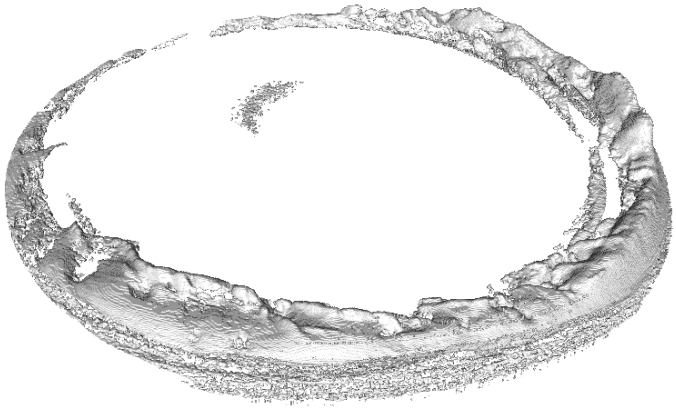

Figure S3. 3D rendering showing the net volume expansion after the 0.1C charge process, calculated from the tomography datasets measured at the beginning and the end of 0.1C charge process. Note that this process ignores the slightest volume expansion that has been blocked by the largest ones due to the X-ray absorption.

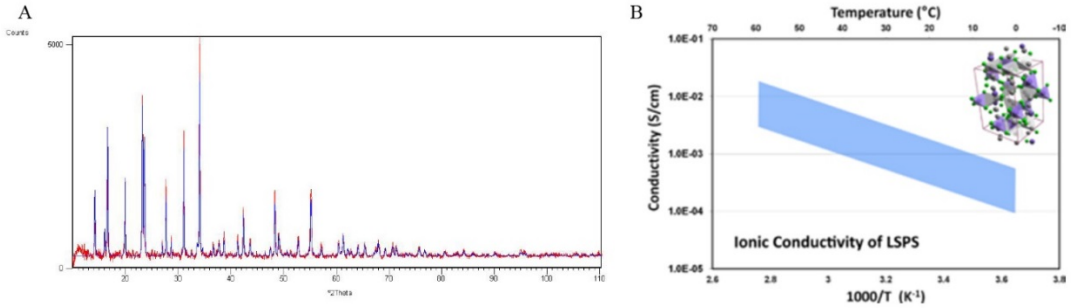

Figure S4. XRD pattern (A) and ionic conductivity (B) of the employed LSPS solid electrolyte. The ionic conductivity is obtained from the NEI Corporation.

3. Summary and conclusions

In this dissertation, X-ray and electron-based imaging techniques were employed to investigate Si and Li anodes under *in-situ* and/or *operando* conditions. The morphological and structural changes as well as the electrode/electrolyte interfacial evolution, which determine electrodes' overall performance but can be hardly unraveled by *ex-situ* characterization techniques, were visualized and quantified to disclose the degradation behaviors of these two promising anode materials.

In Section 2.1, using *operando* synchrotron X-ray radiography, the time-lapse microstructure evolution of a silicon electrode during battery operation was visually illustrated. Specifically, the volume expansion and shrinkage of individual Si particles during lithiation and delithiation were presented. The diameter/volume evolution was quantified during the first particle lithiation and delithiation. The expansion/shrinkage behavior is found to be related to the initial particle size but does not show a direct relationship with de/lithiation depth, which is also affected by the changing electron-conductive network and surrounding chemical environment (electrolyte migration, SEI propagation, *etc.*). In addition, an expansion prolongation phenomenon after reversal of the current polarity was observed, quantified, and explained based on the hypothesis of different expansion behaviors of particle cores and outer regions.

The deposition behavior of lithium at the Li/separator and Li/carbon matrix interregion was systematically studied by synchrotron X-ray tomography, as presented in Section 2.2. The deposition sites were found to be quantitatively more and widely located when the deposition was polarized under a higher current density. The morphology and distribution of Li deposition within the commercial Celgard® 2325 separator were firstly visualized and quantified in three dimensions. This promotes the understanding of cell short-circuit from a transient incident to a propagation process. In addition, the spatial distribution of Li deposition inside the deposition host (a porous carbon fibre matrix), which depends on the conductivity of the host, was visualized and quantified. The Li deposition behaviors found along the Li/separator interface, inside a trilayer separator and a porous carbon matrix provide deep insights and promote the development of surface modifications related to Li anodes, separator and the cell geometry design for accommodating Li deposition and preventing fast cell failure.

To further reveal the Li deposition mechanism, quasi *in-situ* SEM was employed to unravel the nucleation and growth of Li electrodeposition in a liquid electrolyte at multiple length scales, as shown in Section 2.3. Initial Li nucleation and the morphology evolution of deposition were well preserved without the presence of a separator and external pressure. The SEM images show that Li nucleation preferably germinates from the surface irregularities (cracks and impurities) of the Li substrate. At current density below the diffusion limiting current, deposition morphology was found

to evolve from ball-like to the co-existence of granular and columnar. At a higher current above the diffusion limiting current density, bush-like deposition appears with ball-like and fibre-like deposits covering the backbones of the bush. Cross-sectional views obtained by focused ion beam reveal the inner structures of the Li deposition and provide new insights into the evolution of Li deposition. In addition, computational modeling confirms the favorable nucleation sites and helps to explain the nucleation and growth behavior of Li deposition.

Aiming to suppress the severe side reactions found in Section 2.2 and 2.3 between Li and liquid electrolyte, $Li_{10}SnP_2S_{12}$ (LSPS) solid-state electrolyte was adopted in a Li-S cell in Section 2.4. The morphological and compositional evolution was dynamically visualized by *operando* synchrotron tomography and energy dispersive diffraction simultaneously. The progressively formed cavities/voids at the InLi/LSPS interface observed from the tomographic measurements give direct evidence to the interfacial mechanical degradation. Additionally, the energy dispersive diffraction results and the electrochemical performance agree well with the interfacial degradation of InLi/LSPS.

As a whole, it can be concluded that a flexible and stable carbon/binder matrix with nm-sized homogeneously dispersed silicon and pre-reserved space for silicon expansion is a promising strategy for silicon electrode design. Regarding Li anodes, a homogeneous and smooth-faced Li anode without obvious “hot spots” for preferred deposition is crucial to suppress the formation of inhomogeneous deposition. Furthermore, the development of novel liquid, polymer and solid-state electrolytes which enable a long-term stable Li/electrolyte interface, determines the commercialization process of batteries based on Li-metal anodes.

4. Outlook

In-situ and/or *operando* synchrotron X-ray imaging and electron imaging have revealed the morphological and structural change as well as the electrode/electrolyte interfacial evolution of Si and Li anode. Based on the obtained findings, some future work and directions can be suggested.

1. Optimization of the particle size of Si anodes. Silicon anodes with μm-sized particles will undergo severe volume expansion/shrinkage as well as particle fracture/pulverization. Si particles with nanoscale dimension could potentially undergo smaller volume change during de/lithiation. In addition, smaller particles could generally lead to a higher capacity. However, due to the large specific area of nm-sized particles, more electrolyte is supposed to be consumed due to SEI formation. Therefore, the particle size needs to be optimized to achieve a high energy density in the quest for practical use of Si anode.

2. The development of novel liquid, polymer and solid-state electrolytes. The unavoidable and continuous side reactions between metallic lithium and standard liquid electrolyte require excess electrolyte and thus largely decrease the energy density and service life of Li metal batteries. Novel liquid, polymer and solid-state electrolytes which can enable a stable Li/electrolyte interface are crucial and a pre-requisite for a massive commercial deployment of rechargeable Li metal batteries.

3. The combination of several complementary characterization methods. Synchrotron X-ray imaging has shown great and unique advantages in depicting the morphological, structural and interfacial evolution occurring within a closed cell system non-invasively and non-destructively under *in-situ* and/or *operando* conditions. Techniques that are able to collect detailed chemical and elemental information at a higher temporal and spatial resolution are good complements, and could further promote the understanding of battery degradation and failure as well as the development and optimization of novel battery materials.

5. Acknowledgment

First of all, I would like to thank my supervisor Prof. Dr. John Banhart and Dr. Ingo Manke for providing me the opportunity to work on this project at Technische Universität Berlin and Helmholtz-Zentrum Berlin. I would like to express my grateful acknowledgment to their support, their guidance and inspiration throughout my doctoral work.

I would like to acknowledge my colleagues Dr. Fu Sun, Dr. Henning Markötter, Dr. André Hilger, Markus Osenberg, Dr. Tobias Arlt and Dr. Nikolay Kardjilov for their assistance on both scientific and other occasions.

There are many people who also provided technical assistance and discussions who I would want to thank. This includes Dr. Charl Jafta, Dr. Sebastian Risse, Arne Ronneburg, Dr. Anna Manzoni, Dr. Fabian Wilde, Ralf Britzke and many others.

My thanks also go to Christiane Föster, Claudia Leistner, John Schneider for their support to my experiments; as well as Jörg Bajorat for technical assistance during my Ph.D. work.

I would like to mention Xingpu Zhang, Jian Ren, Li Zhang, Dr. Yajie Wang, Dr. Meng Liu, Dr. Fanxing Xi, Zi Yang, Dr. De Ning, Chao Yang who also study or work at Helmholtz-Zentrum Berlin, and those great guys I met including Shengkai Duan, Zun Huang, Shengjian Zhang, Jue Sun. The wonderful time we spent together is an important part of my study in Berlin.

With this opportunity, I would also like to acknowledge the China Scholarship Council for financial support to my Ph.D. study in Germany.

Last but not least, I am extremely grateful to my parents, brother and my beloved Yu Tan, who have always stood by me. Without your persistent support, encouragement and love, I cannot have reached so far.